THE EFFECT OF SHOT DEPENDENCY ON COMPOSITE MATERIALS SUBJECT TO BALLISTIC TESTING

THESIS

Clayton C. Hankins, Second Lieutenant, USAF

AFIT-ENY-MS-21-D-068

DEPARTMENT OF THE AIR FORCE
AIR UNIVERSITY

AIR FORCE INSTITUTE OF TECHNOLOGY

Wright-Patterson Air Force Base, Ohio

AFIT-ENY-MS-21-D-068

THE EFFECT OF SHOT DEPENDENCY ON COMPOSITE MATERIALS SUBJECT TO BALLISTIC TESTING

THESIS

Presented to the Faculty

Department of Aeronautics and Astronautics Engineering

Graduate School of Engineering and Management

Air Force Institute of Technology

Air University

Air Education and Training Command

in Partial Fulfillment of the Requirements for the

Degree of Master of Science in Aeronautical Engineering

Clayton C. Hankins, B.S.

Second Lieutenant, USAF

December 2021

AFIT-ENY-MS-21-D-068

THE EFFECT OF SHOT DEPENDENCY ON COMPOSITE MATERIALS SUBJECT TO BALLISTIC TESTING

THESIS

Clayton C. Hankins, B.S.
Second Lieutenant, USAF

Committee Membership:

Michael M. Walker, Lt Col, USAF, Ph.D.
Chair

John H. Hansen, Maj, USAF, Ph.D
Member

Carl R. Hartsfield, Ph.D
Member

Abstract

Ballistic analysis was performed on four common composite armor materials: 3k standard modulus plain weave carbon fiber, 8HS satin weave S-glass fiber, plain weave Kevlar® KM2 600 Denier fiber, and Spectra Shield® 4232 ultra-high molecular weight polyethylene to determine shot dependency based upon shot-to-shot impact distance, degree of penetration from the initial impacts, and the delamination effects from the initial impact. The primary measure of ballistic performance was the projectile velocity which represents a 50% probability of penetration, V_{50}. This velocity was determined using a three-phase optimal design test method with an average of twelve shots per test. Delamination was assessed via visual inspection and the tap test. All plates were 0.25 inches thick and impacted at 0° obliquity from a 0.5-inch-diameter hardened steel ball bearing fired from a nitrogen gas gun. This investigation was in response to previous research detailing the potential increase in the ballistic limit with delamination overlap. Additionally, an ensemble regression analysis of available ceramic armor data was performed to model ballistic performance. The results of the experimental study found no statistically significant increase in performance for the materials tested. The only shot dependency with statistical significance was a $1-2\%$ decrease of the ballistic limit for carbon fiber plates with a second impact one and two projectile diameters away. The regression ensemble proved capable of predicting the ballistic limit with an average error of 6.5%. The research recommends additional investigations into the ductility of composite materials to predict delamination, updates to MIL-STD-662F, and refinement of advanced modeling techniques in ballistic testing.

This thesis is dedicated to my wife for her unwavering support throughout this journey. Thank you for your commitment. To God alone be the glory.

Acknowledgements

Several hands assisted in creating this product. A special thanks goes out to Alex Moran and Roger Gerzeski for their assistance setting up the range and running the initial tests to begin this process. Their assistance provided the background knowledge of the tools available to successfully complete this investigation.

Thank you to Stan Lyons, Erik Johnson, and the team at TenCate Advaced Armor for your helpfulness contextualizing the scope of this project to current applications of composite armors. Thank you for your assistance developing the test articles for this study. I would also like to thank Lt Col Walker for his assistance organizing this research and creating the connections necessary for this product.

I am especially appreciative of Lts Jack Morgan and Alex Ramsperger. Both of them dedicated many hours assisting me in range operations. This project would not have been completed without their continuous willingness to make time in their schedules for this project. Thank you for keeping me sharp during testing and your attention to detail.

Finally, I would like to thank my wife, her family, and my family for their willingness to listen to me throughout the writing process. They have endured the worst of my frustrations and have been incredibly supportive. To my wife, thank you for always taking care of me and motivating me to grow throughout this process. Most importantly, thank you for always directing the glory to God. You have consistently reminded me to keep God first through it all.

Clayton C. Hankins

Table of Contents

Page

List of Figures

List of Tables

THE EFFECT OF SHOT DEPENDENCY ON COMPOSITE MATERIALS SUBJECT TO BALLISTIC TESTING

I. Introduction

1.1 Motivation

Test and evaluation are necessary within the modern civilian and defense acquisitions architecture to create an unbiased arena for all design candidates. Testing standards are published to ensure all designs are reviewed in a standard form. For hard armors, MIL-STD-662F provides these standards for department of defense applications. Unfortunately, the standards do not adequately address modern composite armors, subject to substantial delamination. Research both to classify delamination and determine the effects on the armor's ability to absorb and dissipate ballistic energy was limited in overall scope. Kinsler and Collins, as well as Keane, have highlighted the potential for statistically significant deviations from an undamaged test panel; however, continued testing to validate their findings and create a general trend for composite plates had not previously been completed[1, 2].

The previously mentioned research was performed against a limited sample of modern materials, and no effort was made to isolate potential design variables which may lead to delamination effects or variations in multi-hit properties. Generally speaking, numerical methods and analytical methods designed to model ballistic events are also material and projectile dependent. These methods address a single impact and are most focused on determining the ballistic limit velocity for the material. Delamination and effects that may alter the material's physical proper-

ties are not addressed, leading to little insight into inter-shot dependency in modern composite armors. While these tools are helpful for single-hit items, their utility in multi-hit analysis was limited. This established the need to conduct experimental analysis to lay the groundwork for future analysis.

Ballistic limit testing has historically been centered around the V_{50} definition of the ballistic limit. This velocity is when the projectile is expected to completely penetrate the armor 50% of the time. Thus, the historical standard was to compute the average velocity of an even number of complete penetrations and partial penetrations to estimate V_{50}. This method is simple and easy to implement, but it lacks efficiency and provides no inherent confidence interval to the resulting estimate. Recent advances in sensitivity testing have provided efficient test methodologies to find V_{50} as well as other quantiles of interest such as V_{10} or V_{90}. Many of these methods apply generalized linear regression models to the data, which provides the experimenter an effective tool for comparative analysis of V_{50} estimates. The Three-Phased-Optimal-Design (3-Pod) sensitivity testing algorithm applied these models to produce significant confidence at all potential quantiles of interest and was determined to be an effective tool for this study[3].

1.2 Problem Statement

Modern advancements in composite armors have led to the observation of new damage modes not previously addressed in testing standards. Kinsler and Collins, and Keane have investigated shot dependency in composite armors based on the observable delamination extent from an impact, but their work was introductory and applied to a single material based on customer constraints. This investigation seeks to isolate design variables within composite armors to characterize the extent of delamination and its effect on a material's V_{50}. The extent of material delamination

was assessed between shots allowing secondary shots to be placed close, medium, and far distances from the previous impact relative to the delamination. The previous penetration types were sorted to eliminate dependencies based upon the type of penetrations. Additionally, the projectile was a spherical ball bearing to eliminate projectile variations from impact to impact. The results were a characterization of material-specific delamination and an assessment of shot dependency for composite materials subject to ballistic impact.

1.3 Research Methodology

Four different families of composite armor: carbon fiber, glass fiber, aramid fiber, and ultra-high molecular weight polyethylene were tested. Each material was tested to determine a baseline V_{50} from which the complete and partial penetrations were separated into two groups. The delamination extent from these shots was then assessed before proceeding with the next series of experimental tests. The close series placed shots within the delaminated region of previous impacts a minimum of one projectile diameter from the previous impact. The medium test series placed shots outside of the delaminated region of the first impact, but close enough, the delaminated regions would overlap. The minimum distance from each test for this test series was two projectile diameters. The far distance represented clean shots with no delamination overlap. All tests were conducted using the 3-Pod methodology.

Once testing was completed, analysis was performed on the delamination extent for each material type based on the type of penetration it received. Statistical analysis was performed to determine whether there was a significant difference between partial and complete penetrations tested near the ballistic limit. Similarly, statistical analysis was also performed on the second shot series compared to the V_{50} estimate of the undamaged material. From this analysis, deviations from the clean V_{50} were assessed,

as well as potential material factors contributing to the performance of the materials.

1.4 Limitations

This investigation was limited to the maximum capabilities of the single-stage gas gun used in this investigation. This prevented the testing of armors with thicknesses greater than 0.25 inches. The standard thickness between armors resulted in unequal areal densities. Similarly, although it was desired to have a consistent fabric weave, three different fabric weaves were tested, introducing an additional variable in material performance. All testing conducted for these materials was limited to a 25 plate material sample, and no tests were performed to determine the physical properties of the final composite product. Specifications for the fiber plies and the matrix material were used to conclude properties affecting the ballistic limit.

1.5 Thesis Overview

The remaining chapters within this thesis are organized as follows. Chapter II presents the background necessary to develop the test methodology utilized in this experimentation. The background reviews several testing standards and experimental methods before introducing practical data analysis tools for ballistic testing. With this information established, material properties and ballistic failure modes were introduced to distinguish between metals and composites clearly. Finally, previous research is addressed to refine the test methods presented in Chapter III. The experimental design is presented here, discussing instrumentation, data collection, and data analysis. Chapter IV first presents the experimental results and their implications. The final element of the results is an ensemble regression model for ceramic armors. The final chapter is Chapter V which contains a synthesis of the significant finding and recommendations for future analysis.

II. Background and Literature Review

The information contained in the following chapter details the review of published information pertinent to V_{50} ballistics testing as well as a review of recent research efforts to characterize composite armors. Through the development of this chapter, the relevance of the subsequent research was demonstrated. Furthermore, preliminary research was directed towards preparing the results of this study in such a manner to enhance existing efforts to model ballistic events. The development of the literature review begins with an overview of ballistic testing standards. The second section contains a review of experimental procedures for ballistic limit testing. The scope of this section primarily focused on the Three-Phase Optimal Design Procedure, 3-Pod as developed by Wu and Tian, with a brief overview of historical and current suggested methods. The following sections reviewed regression modeling, compared ballistic testing techniques, and introduced general material properties. The subsequent section reviews analytical methods prominent in ballistic testing. The literature review concludes with an evaluation of the research, which directly prompted the experimental methodology for this investigation.

2.1 Ballistic Testing Standards

Within the confines of ballistic testing, there are several potential data points of interest. Of most significance for this study is the ballistic limit, V_{BL}. V_{BL} is defined by MIL-STD-622F, the United States Department of Defense (DoD) test method standard for ballistic testing. The DoD denotes three distinct utilizations of V_{BL}: the minimum velocity at which the projectile is expected to consistently penetrate the armor completely, the maximum velocity at which the projectile is expected to fail to penetrate the armor consistently completely, and a velocity within a zone of

mixed results, ZMR[4]. The ZMR is the velocity region where two different outcomes result under identical circumstances. For the MIL-STD and this thesis, V_{50} is the designated velocity to estimate within the ZMR. Other velocities such as V_{10} and V_{90} which represent the projectile penetrating the armor 10 percent and 90 percent of the time, respectively, could also be the focus of independent investigations should the resources be available to test for these velocities; however, the shots taken within this study were focused on finding V_{50}.

The precedent of V_{50} ballistic testing for DoD began as early as MIL-A-46100 when the need for armor plating in Southeast Asia was readily apparent[5]. With its acceptance in 1965, MIL-A-46100 became the base document for military armor testing, growing to be an initial database for steel armors tested against a variety of threats[5]. The information in this original specification expanded as ballistic armor testing matured, leading to additional military standards and performance specifications for various materials. For composite armors, MIL-PRF-4610E and MIL-STD-3038 both specifically cite the use of V_{50} for ballistic testing as defined in MIL-STD-662F[6, 7].

V_{50} has also been utilized in law enforcement applications. In the National Institute of Justice (NIJ), standard for body armor, V_{50} is mentioned as the prescribed ballistic limit[8]. The seventh edition of the previously referenced standard has been made available for public comments as a draft. It maintains the historical precedent of V_{50} but builds upon the advances in ballistic testing allowing for V_{Proof} standards as related to armor acceptance testing[9]. The "Proof" velocity builds upon the concept of logistic regression for modeling the ZMR without the necessity of testing each potential probability of penetration. The research detailing logistic regression is examined in Section 2.2.

Although several other ballistic testing standards exist, including international

test operations procedures, ITOP-2-2-713, and nation-specific standards, the final relevant standard to be reviewed was STANAG 2920. This document is the North Atlantic Treaty Organization (NATO) standardization agreement for the ballistic testing of armor and combat clothing. The most recent revision, edition three, published in 2015, was not available for review, but the previous edition and a summary of the changes from edition two to edition three were available. In both documents, the testing is designed to determine either V_{50} or V_{Proof}, similar to the NIJ standards[10, 11]. Of significance for this thesis is the transition from classical binomial assessments of ballistic testing to modern sensitivity testing. To be clear, ballistic testing standards are still reliant on an arithmetic mean to calculate the final V_{50}. Although verbiage in documents such as the draft for NIJ 0101.07 allows for alternate test methodologies, the provided test method is still a modified up-down method[9]. Despite the simplicity of the test method and its ability to define a point of interest within the ZMR, it is wholly underwhelming when attempting to undertake a statistically relevant analysis of the results. As researchers develop new simulation codes for ballistic events, more robust analytical methods provide more meaningful information to the researcher, developer, and final customer.

2.2 Experimental Procedures for Ballistic Limit Testing

Despite the continuity between international testing standards on the definition of V_{BL} as either V_{50} or V_{Proof} depending on the armor application, there are several variations in the experimental process worth discussion. This section introduces some of these variations and provides a rationale for using 3-Pod. This section is not intended to be an exhaustive review of the selected methodologies but rather an overview of the methodology's strengths and weaknesses. Three different aspects of experimental testing are covered within this section: testing algorithms, regression

models, and quantal response.

Ballistic testing algorithms are the methodologies by which the test velocity is selected in a given ballistic event. For armors undergoing proof testing, the test velocity could be as simple as reading the design specified protection level and testing against said threat. Testing of this nature leads to validation tests such as the "22 of 22" test highlighted in Eridon [12]. If the test article survives 22 specified shots against the designed threat level, it meets the minimum requirements of the test and is accepted. A test of this nature highlights the limitations of testing a single velocity range. No valuable data is collected on the test article except whether it passed or failed against the threat. The same article states that the current shortcomings in ballistic testing can be relieved utilizing a more sophisticated test procedure, which yields far more detailed results with the potential for enhanced confidence and analysis of the design. These modern methods for sensitivity testing provide robust capabilities for the experimenter by distancing themselves from historical methods such as the Up-Down method and the Langlie method through dynamic programming options and building upon each other to hone the testing process. The result is a series of testing methodologies designed to optimize data collection throughout the entire response curve, provide sufficient data for intensive statistical analysis, and provide the experimenter sufficient means to perform sound quantitative analysis on the test articles. Five different test methods are introduced to build the context for the testing methodology presented in Chapter III: the up-down method, Modified Langlie, Neyer Method, Robbins-Monro-Joseph, and 3-Pod.

2.2.1 Up-Down Method

As previously mentioned in Section 2.1, current ballistic testing standards still rely on an arithmetic mean to calculate V_{50}. To accomplish this, a series of test shots are

fired in sequential order, following a series of fixed step sizes. The method instructs the tester to increase velocity if the result is a partial penetrations, P_P and decrease velocity if it is a complete penetrations, C_P. This sequence creates an up and down pattern when velocity is plotted versus the test number after the test. The Up-Down method is complete when the prescribed number of C_P's, and P_P's, have been shot within the specified velocity range. For example, STANAG 2920 requires at least 6 shots but no more than 14 equally split between C_P's and P_P's and a maximum velocity spread of 60 meters per second[11]. While this methodology is straightforward to implement, it is only suitable for V_{50} testing. Testing for V_{10} or other similar proof velocities under a similarly simple methodology requires a test like the "22 of 22" test mentioned above. Another limitation of the Up-Down method is its lack of inherently available statistically relevant characteristics. It provides a mean estimate only but no methodology to conduct error analysis or hypothesis testing between two unique tests on the same material. Literature from 1950 presented in ARL-TR-7088 highlights the need for additional supporting methodologies to make the Up-Down method more statistically robust; however, as Collins states, "Unfortunately, as time passed, this knowledge was ignored." [13] the remainder of his article reconstructs the history of ballistic testing in more depth and was referenced further within this text. As for the Up-Down method, what it lacks in depth it makes up for in ease of application. No extensive computing power or sophisticated methodology is needed to complete the test, nor is there a need for detailed data processing to produce relevant results. For this reason, the method has maintained its prominence in ballistic testing despite other test methods which offer greater insight into the test article. Table 1 is adapted from MIL-STD-662F and NIJ 0101.06. The table provides an application of the methodology per testing standards. The method mitigates extreme events based on the algorithm's simplicity and its fixed step size. Again, this method is best suited

Table 1: Up-Down Method Algorithm

Shot Descriptor	Velocity Step	Previous Penetration
Initial Shot	Specification Declared Velocity	None
Until First Reversal	100 ft/s	Partial
	−100 ft/s	Complete
Until Second Reversal	75 ft/s	Partial
	−75 ft/s	Complete
After Second Reversal	50 ft/s	Partial
	−50 ft/s	Complete

for V_{50} testing only and has no mechanism to determine the range of the ZMR. If the test is applied to a material with unknown ballistic properties, it may struggle to converge due to the fixed step size. This makes the Up-Down method most applicable where the initial velocity guess is made with high velocity or testing to determine if a specification is met. No guaranteed maximum or minimum number of shots is needed for this method unless specified by experiment constraints.

2.2.2 Modified Langlie Method

H. J. Langlie derived the Langlie method in 1962 as a sensitivity test for electrical components when fifteen to twenty test articles were available[14]. Under these conditions, insufficient data could be reliably collected using either the Up-Down method or the Probit method, to be discussed in Section 2.3. Similar to other tests for ballistic evaluation, the Langlie method is sequential with a focus on determining the mean response, V_{50}. Unlike other tests, the Langlie method begins with an upper and lower limit then uses a variable step size to isolate V_{50}. This methodology collects data inside and outside the ZMR, which is utilized to form a logistic fit based on all test points. A modified form of the Langlie method is actively used within the DoD as described within Collins and Moss[15]. In short, the method begins with an esti-

mated maximum and minimum mean, μ_{max} and μ_{min}, respectively, which lies ± 65 ft/s from the estimated ZMR. The first shot is the average of these means while each subsequent shot is based upon the outcome of the previous shots in the general form, $x_{i+1} = (x_i + x_{Vari})/2$. x_{Vari} is dependent on the outcome of the previous shots and the shot number. Table 2 presents the Modified Langlie method. The modifications to the method improved the procedures for data points away from V_{50} resulting in a better logistic fit and ability to meet stopping criteria. An important characteristic

Table 2: Modified Langlie Method Algorithm, Adapted from Burke and Truett[16]

Shot Descriptor	**Previous Penetration**	**New Velocity**
Initial Shot	None	$x_1 = \frac{\mu_{min}+\mu_{max}}{2}$
Second Shot	P_P	$x_2 = \frac{x_1+\mu_{max}}{2}$
	C_P	$x_2 = \frac{x_1+\mu_{min}}{2}$
Third Shot	C_P, P_P	$x_3 = \frac{x_1+x_2}{2}$
	P_P, C_P	$x_3 = \frac{x_1+x_2}{2}$
	P_P, P_P	$x_3 = \frac{x_1+\mu_{max}}{2}$
	C_P, C_P	$x_3 = \frac{x_1+\mu_{min}}{2}$
No Reversal?	All P_P	$\mu_{min} = \mu_{min} - 65ft/s$ $\mu_{max} = \mu_{max} - 65ft/s$ $x_4 = \frac{x_3+\mu_{max}}{2}$
	All C_P	$\mu_{min} = \mu_{min} + 65ft/s$ $\mu_{max} = \mu_{max} + 65ft/s$ $x_4 = \frac{x_3+\mu_{min}}{2}$
For All Additional Shots		
Previous Shots: P_P, C_P or C_P, P_P		$x_{i+1} = \frac{x_i+x_{Prev}}{2}$
$\#\ P_P \neq \#\ C_P$	Backtrack ($x_{Prev} = x_{i-n}$) until equal $x_{i+1} = \frac{x_i+x_{Prev}}{2}$	
If $\#\ P_P \bar{\#}\ C_P$ is not possible:		
Previous Shot: P_P		$x_{i+1} = \frac{x_i+\mu_{max}}{2}$
Previous Shot: C_P		$x_{i+1} = \frac{x_i+\mu_{min}}{2}$
Test for at least 8 shots and all stopping criteria are met		

of the Langlie method, and other ballistic models applying logistic modeling to allow quantal analysis, is breaking separation. Breaking separation in ballistic testing is to have a P_P that is faster than a C_P, crossover between the two possible outcomes of the binary sensitivity test. This allows the researcher to estimate parameters such as V_{50} by creating a logistic curve fit of the probability of response through the ZMR. With this in mind, the following four events are the stopping criteria for the Modified Langlie method[15].

i. Obtain a ZMR (Break separation between P_P's and C_P's)

ii. Average of all C_P's is greater than the average of all the P_P's

iii. Spread of the closest three P_P's and three C_P's is $\leq$ 125 ft/s

iv. Confirm test points exist $\pm$ 65 ft/s from V_{50} estimated from the average of the shots in the third stopping criterion

All four stopping criteria must be met to terminate the test and take at least eight shots. The DoD standard for the Modified Langlie method establishes a maximum number of trials at 15 shots[15]. The established boundaries for the Langlie method distinguish it from other tests when only a limited number of test articles are available by allowing the researcher to create a definite test plan from the available test articles. To calculate V_{50} with this methodology, computing power is required to apply the maximum likelihood equations or other generalized models. The derivation of the maximum likelihood equations may be found within Langlie's initial report in reference [14]. The Langlie method is best suited for V_{50} calculations but capable of determining V_{10} due to its estimations over the entire ZMR. The Langlie method is efficient for calculating the standard deviation and mean; however, minimal refinement of the estimated parameters is achievable under non-ideal circumstances.

2.2.3 Neyer Method

Developed in 1989 and further improved in 1994, the Neyer method seeks to improve the efficiency of sensitivity tests and introduce a method of analysis to improve upon the limitations of the maximum likelihood equations[17]. The Neyer method is the first example of a sequential method designed with multiple phases. The three phases work in sequence to find the mean, compute the maximum likelihood estimates for mean, μ and standard deviation, σ, and apply estimates to refine both the mean and standard deviation. Unlike the methods formerly presented, the Neyer method is applied through a software package available for purchase through Dr. Neyer, along with personally taught seminars on sensitivity testing and the use of his method. The following analysis of his method focuses on the flow of the test algorithm rather than the coded logic to run the formal test.

Before presenting the Neyer method, it is essential to understand the key parameters driving the search for an optimally designed sensitivity test. The first of these parameters is the maximum likelihood estimators. Using the nomenclature from *Sensitivity and Analysis*, where L_i is the stimulus level, N_i is the number of successes, M_i is the number of failures, $\mathrm{P}(\mathrm{L}_i)$ is the probability of response at a given stimulus level, and T_i is the total number of shots, the likelihood function is provided in Eq. (1)[17]. This function serves as the objective function for optimizing the response to produce the proper mean, μ, and standard deviation, σ, assuming the distribution of the sensitivity analysis is normal. Considering this analysis is for ballistic testing, the stimulus is the velocity, and μ and σ represent the actual material V_{50} and standard deviation.

$$L(L_i, N_i, M_i|\mu, \sigma) = \prod_i \binom{T_i}{N_i} P(L_i)^{N_i}(1 - P(L_i))^{M_i} \tag{1}$$

Since the true material properties are unknown in ballistic testing, an optimal guess

maximizes the likelihood function. That is, the derivatives of the likelihood function are set equal to zero and solved to determine the maximum likelihood estimators(MLEs), μ_g and σ_g.

Additional analysis of the test data can be accomplished using the Fisher information matrix presented by Kendall and Stuart in 1967 and presented within Neyer's explanation of his test methodology[17, 18]. The equations specifically of interest in sensitivity testing are presented as Eq. (2) and Eq. (3).

$$I_{jk} = \sum_i T_i J_{j+k}(Z_i) \tag{2}$$

Where J_{j+K} is defined as:

$$J_j(z_i) = \frac{P'^2(z_i) z_i^j}{P(z_i)(1 - P(z_i))\sigma^2}. \tag{3}$$

These equations are derived from the second derivatives of the log of the likelihood function and provide the basis for Neyer's rapidly converging initial phase. When plotted against a normal stimulus level as in Fig. 1 it is clear that little additional test article information is gleaned from tests after three standard deviations. J_0, J_1, and J_2 are the variance of μ, the covariance of μ and σ, and the variance of σ; respectively, leading to the conclusion, the optimal test location is approximately $\mu \pm \sigma$ to improve both μ and σ simultaneously. Another aspect of the Neyer method is being a D-optimal design. The specifics of D-optimality are not essential for its application. Only the effects of its application are presented. In summary, D-optimal designs refine the entire response curve rather than focusing on a quantile of interest, for instance, V_{50}. By approaching maximization of the likelihood function from this aspect, it was determined that the determinant of the information matrix was maximized when test points were evaluated at $\mu \pm 1.138\sigma$[18]. Several additional sources

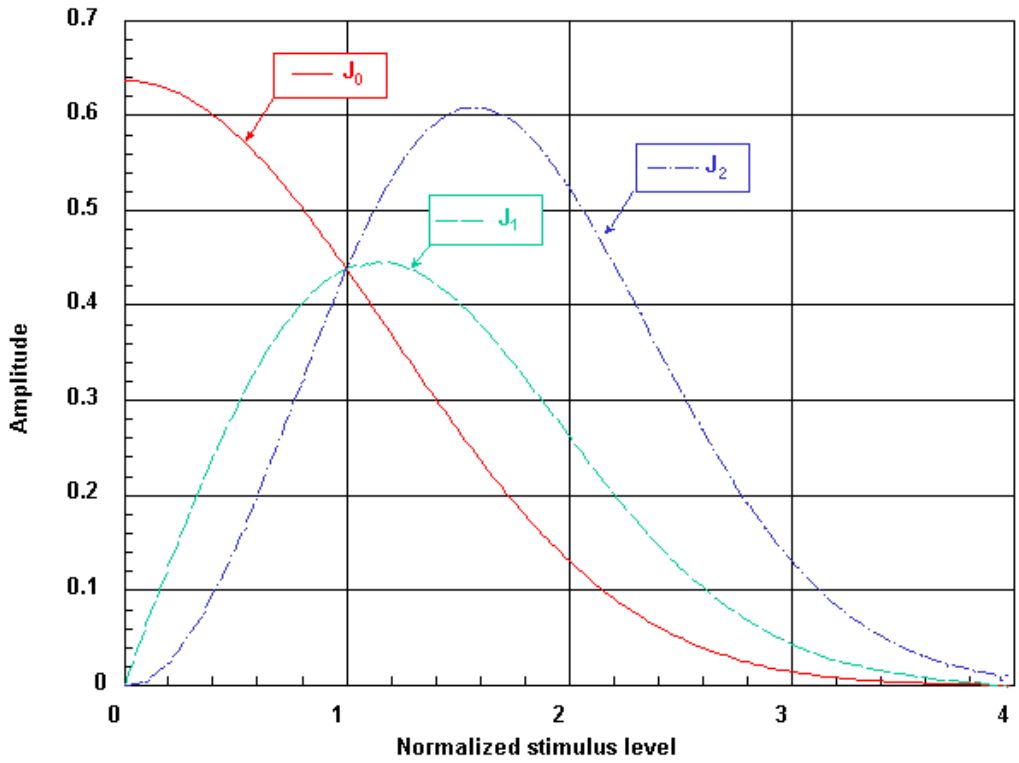

Figure 1: Sensitivity Test Matrix Functions[17]

are presented within Neyer's *A D-Optimality-Based Sensitivity Test*, Ref. [18], for a detailed explanation of how the D-optimal result maximizes the likelihood function and minimizes the area of the standard confidence ellipsoid about μ and σ.

To run a Neyer test, guesses of the upper and lower limits for the mean and the standard deviation are required. Then using this information, the testing sequence begins by rapidly seeking to converge to the true mean through a modified binary search[18]. This testing phase aims to bound the test sequence with a recorded response and non-response, for this investigation, a recorded C_P and P_P. A flow chart of the implementation of the Neyer Method in "gonongo" is provided in Fig. 2[19]. "Gonogo" was the "R" implementation of the testing algorithms used in this thesis. Its details are further discussed in Chapter III. Unlike the Langlie method, where the initial shots slowly increase the range of velocities tested should the same response

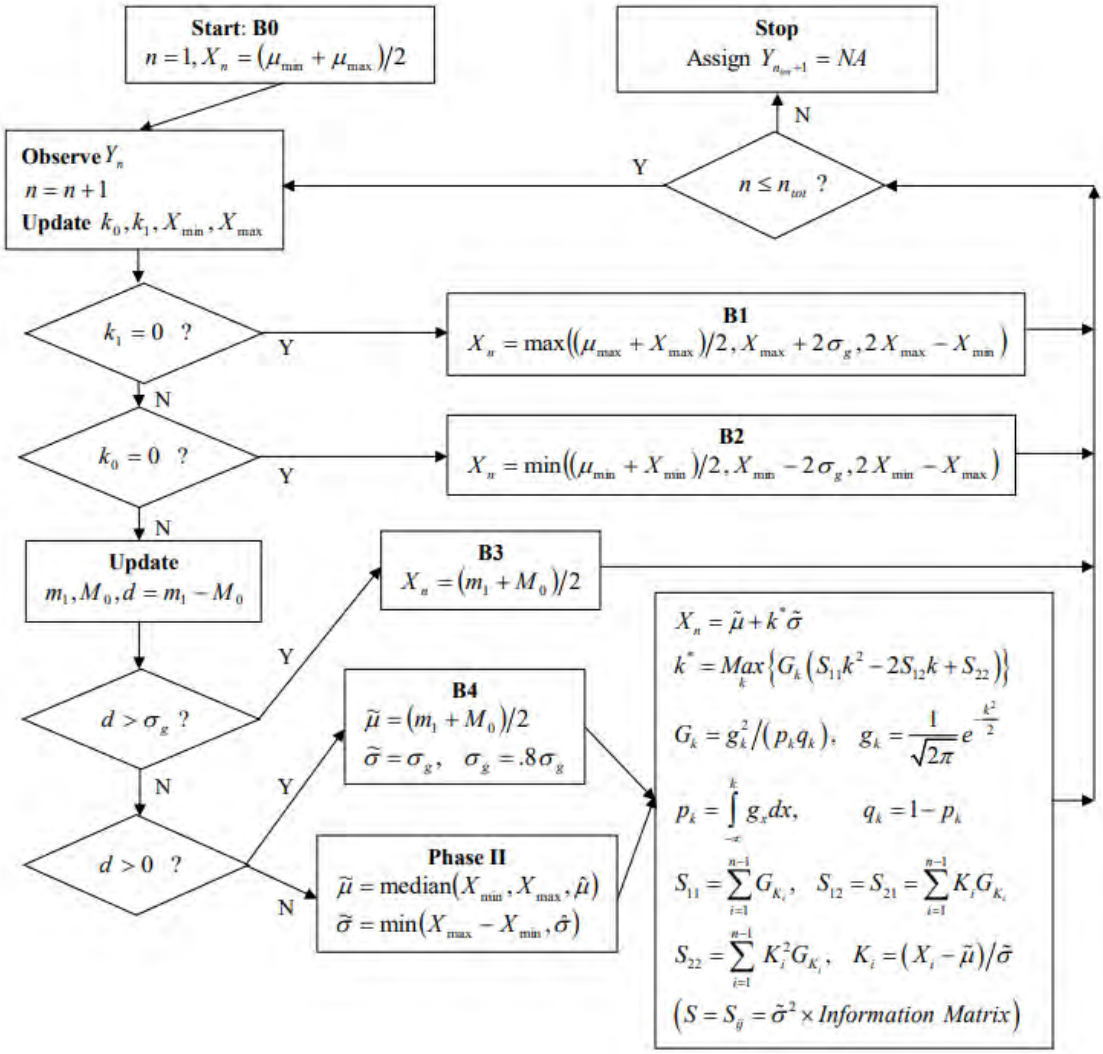

Figure 2: Flow Chart Algorithm Neyer Method [19]

occur more than twice in a row, the Neyer method doubles the range of velocities tested to expand the test range rapidly should the test article perform significantly different than expected. This allows the Neyer method to reduce the number of wasteful shots greater than three standard deviations from the mean, improving the overall efficiency of the test.

Once this testing phase is completed, at least one response is recorded, phase two begins. Observing the flow chart of Fig. 2 only the bottom three blocks from right

to left pertain to phases two and three of the Neyer method. The other blocks detail the determination of the stimulus level for phase one as this phase lends itself to a simplified algorithm. Phase two, on the other hand, utilizes the maximum likelihood functions to maximize the determinant of the information matrix[18]. Specifically, block B4 represents Neyer's phase two. The mean guess is calculated in this block by calculating the highest non-response and lowest response average. At the same time, the guessed standard deviation is iteratively reduced by $0.8\sigma_g$ until separation is broken and crossover is achieved. The new testing stimulus level for each shot is determined by selecting the value at which the determinant of the information matrix is maximized.

The third and final phase of the Neyer method, labeled as Phase II in the flowchart, no longer guesses the mean and the standard deviation based on the original estimates provided by the test conductor. At this point, enough information has been collected to determine unique MLEs from the maximum likelihood equations. Refinement of the MLEs is accomplished by maximizing the information as mentioned previously in this section. It is in this phase where the Neyer test becomes D-optimal by testing with stimulus levels at near $\mu \pm 1.138\sigma$ as referenced previously.

What sets the Neyer test apart from the previously discussed methods is its emphasis on using statistically relevant metrics to refine the testing process dynamically and efficiently. While the test ultimately is designed to determine the mean and standard deviation of binary response sensitivity experiments, the D-optimal approach and iterative utilization of the maximum likelihood equations refines the confidence of the entire response curve allowing analysis at probabilities other than fifty percent. The method is robust and efficient but requires computing abilities to continuously run and update the results from the MLEs during experimentation.

2.2.4 Robbins-Monro-Joseph Method

Before introducing the Robbins-Monro-Joseph method, RMJ, and its derivatives, this thesis does not derive an improved methodology or suggest limitations of current variations. Instead, the objective of this section is to introduce the evolution of the Robbins-Monro test methodology to the current version, which is helpful in today's modern sensitivity testing. Furthermore, the author acknowledges that the following methodology is presented in generalized terms applicable for a plethora of sensitivity tests, of which ballistic testing is one relevant source of binary response data.

Three iterations of the RMJ method are presented along with a brief discussion of the limitations that were addressed with each iteration. The first is the original Robbins-Monro method developed in 1951. This method is stochastic in nature making no assumptions of the distribution functions or the variables controlling the response[20]. The method utilizes a priori knowledge of the distribution, distinguishing itself from methods discussed formerly. As such, this method is not utilized to find an unknown parameter, such as V_{50}, but rather improves the estimate of the parameter. Keeping with the standard nomenclature of the source papers, let $M(x)$ be the unknown distribution function with response , Y [21, 22]. Robbins and Monro proved if the values of x were chosen sequentially by Eq. (4),

$$x_{n+1} = x_n - a_n(y_n - \alpha) \tag{4}$$

where y_n is the binary response and a_n meets the form of Eqs. (5) and (6), and c is some constant

$$a_n = \frac{c}{n} \tag{5}$$

$$\sum_{n=1}^{\infty} a_n = \infty, and \sum_{n=1}^{\infty} a_n^2 < \infty, \tag{6}$$

then the value of x will approach the desired probability of response defined as α. Later research conducted from the mid 1950s through the 1990s proved, although simple, defining a_n as in Eq. (5) led to sub-optimal performance requiring significant modification to perform well at extreme quantiles[21]. To improve this behavior Joseph demonstrated an improved method which resulted in the RMJ method. Rather than define each step as in Eq. (4), Eq. (7) was proposed[21].

$$x_{n+1} = x_n - a_n(y_n - b_n) \tag{7}$$

Since the true distribution, $M(x)$, is unknown, $E(\Theta)$ estimates the distribution based on known information about the test article with a variance, $var(\Theta) = \tau_1^2 < \infty$. With this notation, the next stimulus of interest in probability becomes $Z_N = x_n - \Theta$ such that optimization can be performed to minimize $E(z_{n+1}^2)$ subject to $E(z_{n+1}) = 0$. The optimization and its proofs may be referred to in depth in Joseph, but the results are as follows in Eqs. (8) to (11)[21].

$$a_n = \frac{1}{b_n(1-b_n)} \frac{\beta\tau_n^2}{(1+\beta^2\tau_n^2)^{1/2}} \phi\{\frac{\Phi^{-1}(\alpha)}{(1+\beta^2\tau_n^2)^{1/2}}\} \tag{8}$$

$$b_n = \Phi\{\frac{\Phi^{-1}(\alpha)}{(1+\beta^2\tau_n^2)^{1/2}}\} \tag{9}$$

$$\tau_{n+1}^2 = \tau_n^2 - b_n(1-b_n)a_n^2 \tag{10}$$

$$\beta = \frac{\dot{M}(0)}{\phi\{\Phi^{-1}(\alpha)\}} \tag{11}$$

This procedure yielded vast improvements from the standard Robbins-Monro method for several distributions, including the logistic distribution suggesting the RMJ method is suitable for application in ballistic testing.

The final iteration of the Robbins-Monro procedures of value for this thesis is

the skewed-RMJ method proposed in 2015 by Wang et al. This method builds upon Joseph's method to address weaknesses at quantiles less than 0.1 and greater than 0.9 by adding an asymmetric quadratic loss function, Eq. (12), with weight, $w = \lambda$,

$$L(z) = wz^2 \tag{12}$$

modified by the experimenter [22]. The remaining process to solve and prove the optimization is similar to Joseph's, with the major adjustment of the proposed skewness coefficient. Simulations comparing the skewed-RMJ method for normal, logistic, and extreme value distributions showed significant improvements over the standard RMJ method for extreme quantiles, but potentially worse results for moderate quantiles if the value of λ were extreme to the order of $50,000$. Unfortunately, there is no standard optimal solution for λ, but Wang et al. suggest a large range of potential values for λ, which could enhance the results. Furthermore, they provide an example of the skewness coefficient for a contextualized problem where the quantal of interest was the fiftieth percentile, much like V_{50} testing. In their example with $\lambda = 10$, they showed the skewed-RMJ method reduced the efficiency of the test but reduced the number of responses, $y = 1$ by thirty percent[22]. Discernment on the experimenter's part is thus necessitated to achieve the desired results. In regions where the ninety-ninth percentile is desired, skewing the RMJ method improves the overall results and accelerates the variation in step size to produce both responses and non-responses.

2.2.5 3-Pod

In the previous examples of sequential sensitivity tests, an effort was enacted to prosecute either simple or efficient experimental designs for the test article of concern. Of the designs presented, Wu describes Neyer's method as "the most novel and effective method in the last 20 years," providing his review of existing methods

before introducing 3-Pod[3]. The Neyer method provides a procedure to efficiently determine the median response as well as refine the complete response within the ZMR through D-optimal design; however, it does not contain an efficient means of isolating a quantal of interest such as V_{10} or V_{90}. 3-Pod provides such analysis by utilizing a three-phase approach to sensitivity testing, building upon concepts from both Neyer and RMJ.

The following presentation of the 3-Pod methodology serves as an introduction to the design architecture, but the presented flow charts for Phase 1 do not contain the modifications of 3-PodM or 3-Pod2.0 as described in the "gonogo" implementation of 3-Pod. The modifications to 3-Pod were not available to the author in mathematical form; however, they were listed in the documentation for gonogo[19]. Still, the flow charts provide the 3-Pod methodology in a most useful format to describe ballistic testing. To be clear, the 3-Pod methodology is a generic sensitivity test applicable for more than ballistic testing.

The first phase of 3-Pod consists of three sub-phases designed to narrow the range of stimulus to a reasonable estimate of the ZMR. This phase mirrors the initial phase of the Neyer method by initiating the search process with a guess of the material standard deviation and a range of stimulus thought to contain the median response as symmetrically as possible. Wu and Tian suggest the range of stimulus values to be at least plus or minus six standard deviations from the median as a rule of thumb to capture the entire ZMR. Using these values to initialize the algorithm, 3-Pod begins the first of three distinct stages. The stages are as follows:

1. Obtain response bounds, (1 C_P and 1 P_P)

2. Search for overlap to define the ZMR

3. Improve the estimate for the ZMR.

Fig. 3 shows the search method utilized to obtain boundaries for the method. Based on the search topology, 3-Pod assumes the provided guesses are symmetric but contains the ability to expand the search region rapidly, reassigning μ_{min} or μ_{max} as required. If the initial responses are not $(y_1, y_2) = (0, 1)$, stage 1 modifies the search parameters until both response are achieved as expected by the algorithm. The exact number of runs for this stage is unspecified. For a properly defined test with reasonable estimates, two shots should provide the information to proceed to stage 2.

Stage 2 approaches the ZMR with two approaches to quickly approach the median quantal then refine the results using steps based on the guessed standard deviation. Initially, stage 2 checks the difference between the maximum and minimum P_P and C_P against the guessed standard deviation. The first potential path represents the case when the difference between the responses is larger than the standard deviation as in Eq. (13). This represents a separation between response and non-response that cannot be efficiently broken via a modified binary search method.

$$MinV_{CP} - MaxV_{PP} \geq 1.5\sigma_g \tag{13}$$

To reconcile this, Wu and Tian approach this problem by applying a location-scale

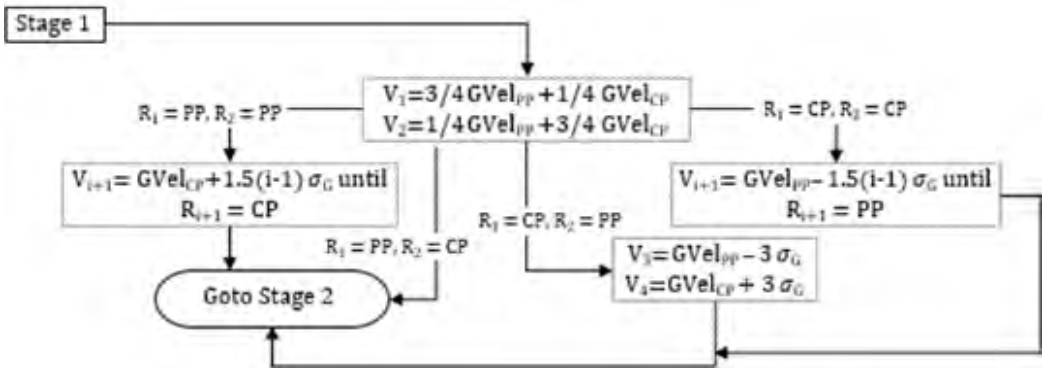

Figure 3: Flow Chart of Phase 1, Stage 1 of 3-Pod [16]

model provided in Eq. (14) where G is a known distribution function such as the normal distribution or logistic distribution. This estimation method then becomes the standard for estimating the maximum likelihood estimates for μ and σ. As presented in the Neyer method, a unique set of MLEs is not possible until separation is broken, defining the ZMR. Therefore, μ is adjusted while σ_g is considered acceptable.

$$F(x, \mu, \sigma) = G(x - \mu)/\sigma \tag{14}$$

Unlike the Neyer method, which continues optimizing the MLEs to generate a final estimate for μ and σ, 3-Pod applies shifts to a branched set of conditional paths when refining the search for the true median response. When the difference between responses is less than 1.5 σ_g as displayed in Eq. (15), the decision-making process for the next stimulus becomes highly dependent on the number of responses and non-responses with the next two stimuli being selected based on whether there are more C_P's or P_P's. The selection process is provided in Fig. 4 from Burke. For each 2 shot iteration that does not produce a region

$$MinV_{CP} - MaxV_{PP} < 1.5\sigma_g \tag{15}$$

of overlap, σ_g is reduced by two-thirds. This stage of the 3-Pod method is the most variable in size that the experimenter does not predetermine. The number of shots required for this stage ultimately depends upon the quality of the guess provided, and the ability of the experimenter to achieve the stimulus levels called for by 3-Pod. Neither of these factors can be directly attributed to 3-Pod's design architecture, but nonetheless affect how an experimenter must design there test when utilizing 3-Pod.

The final stage of 3-Pod's unique Phase I approach is simply and eloquently designed to improve the estimate for μ and σ. In essence, it confirms the previous results

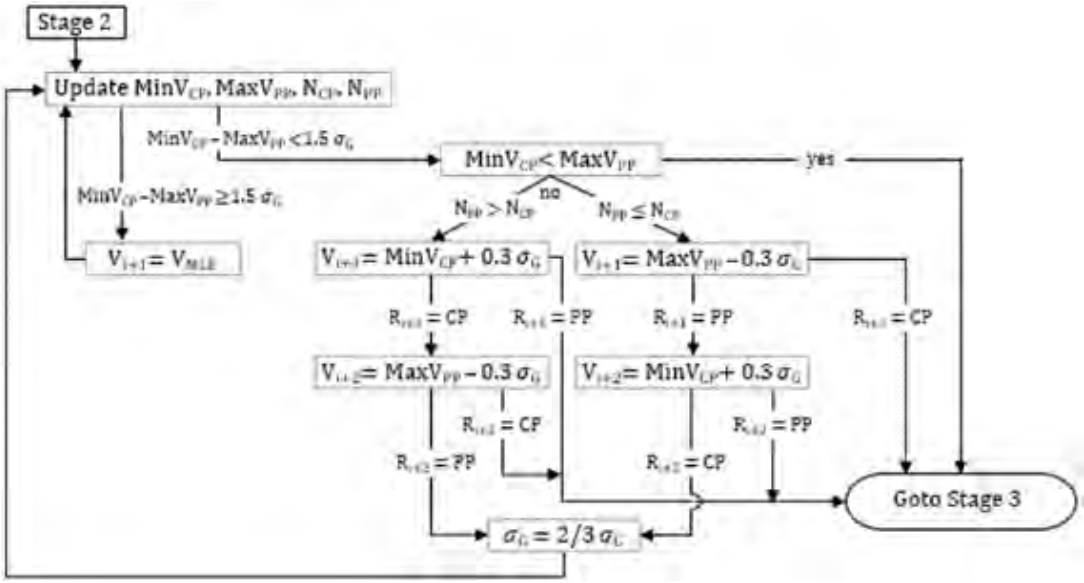

Figure 4: Flow Chart of Phase 1, Stage 2 of 3-Pod [16]

with the updated value of σ_g. The stage begins with a similar inequality as Eq. (13). If the inequality is true, 3-Pod tests a single stimulus, the average of the minimum C_P and the maximum P_P. If the separation is smaller than the final σ_g of stage 2, then two shots are fired at $(MinVC_P + MaxVP_P)/2 \pm 0.5\sigma_g$. A flow chart of stage three is presented in Fig. 5. Upon completion of the three stages of Phase I, 3-Pod has efficiently estimated both μ and σ without the need to compute the maximum likelihood equations or information matrix as in the Neyer method. at this point the

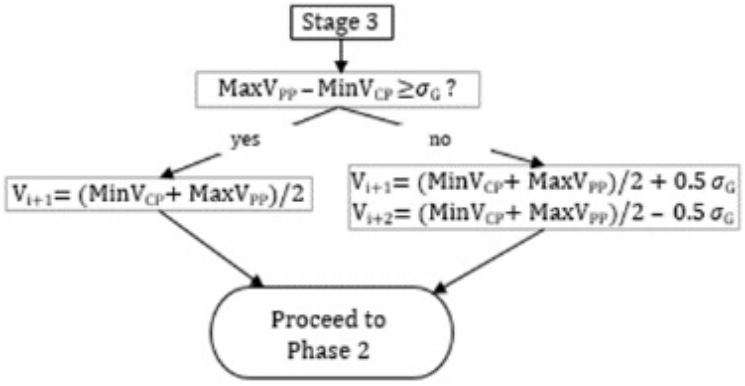

Figure 5: Flow Chart of Phase 1, Stage 3 of 3-Pod [16]

final two phases of 3-Pod are optional, designed to refine the entire response curve or a prescribed percentile of interest respectively.

The final two phases of 3-Pod build upon methodologies introduced in the Neyer and skewed RMJ methods. Phase II of 3-Pod conducts tests similarly to Phase II of the Neyer method. This test phase seeks to improve the entire response curve using the D-optimal design criteria using the Fisher information matrix to inform the optimal velocity for follow-on tests. The number of tests conducted at this phase is experimenter determined. Depending on the purpose of the test and the number of test articles available, this phase of 3-Pod may be omitted. Phase III of 3-Pod uses the skewed-RMJ method to test a specific parameter of interest such as V_{10} or V_{90}. As with Phase II, Phase III of 3-Pod is optional based upon the experimenter's needs. The utility of the skewed-RMJ method has already been introduced, but it had yet to be implemented within a testing scheme to refine a parameter of interest efficiently. Of the entire 3-Pod methodology, only the initial phase represents a truly novel approach to sensitivity testing, but the efficiency and robustness of the 3-Pod methodology make it unique when compared to available sensitivity testing methodologies. It is the only test to be designed with three distinct phases organized to maximize the data collected by the experimenter.

2.3 Regression Modeling in Ballistic Testing

In the previous sections, the need for a method to further analyze the statistical properties of V_{50} is presented. Collins makes the argument in ARL-TR-7088 methods without a ZMR, such as a generic Up-down method, are void of necessary conditions to permit valid statistical inference[13]. In the same way, the testing standards and methodologies currently in circulation provide little insight into a standard definition for the meaning of σ in the context of ballistic testing. NIJ Standard 0101.06 and the

draft of NIJ Standard 0101.07 both suggest the logistic regression for ballistic data analysis but fail to provide any standardized process for reporting uncertainty in the final ballistic testing results[8, 9]. Both the Neyer method and 3-Pod required a guess for the standard deviation, which is implied to reference the variance of the ballistic limit estimate, but only for the mean value, V_{50}. No further discussion of the utility of μ, σ, or the desired V_{Proof} is discussed within these methods leaving the experimenter to determine the appropriate course of action to quantify the uncertainty within their ballistic calculations[17, 18, 3]. For this thesis, regression analysis was focused on applying the maximum likelihood equations within the framework of generalized linear regression using an appropriate link function to model the results through the ZMR. The work informed the rationale behind this application of regression analysis of Collins defining critical aspects of quantal response and a NIST evaluation of regression models[23, 13, 24]

Generalized linear models, GLM, consist of three components: a linear component, a link function, and a variance function. These components allow for statistical analysis and best fit parameters to be applied in a similar manner as those in linear regression. For a binomial distribution as with ballistic testing there are three common link functions utilized to approximate the regression curve. The logit and probit link functions represent a logistic and normal distribution, respectively and are symmetric in nature. The third link function is the complementary log-log (c-log-log) function representing the extreme value distribution and providing an asymmetric approach to the approximation of the response curve from ballistic testing. The distribution functions are provided in the order presented in Eqs. (16) to (18). For each model

$$\frac{e^{\hat{\beta}_0+\hat{\beta}_1\nu}}{1+e^{\hat{\beta}_0+\hat{\beta}_1\nu}} \tag{16}$$

$$\Phi(\hat{\beta}_0+\hat{\beta}_1\nu) \tag{17}$$

$$1 - e^{-e^{(\hat{\beta}_0 + \hat{\beta}_1 \nu)}} \tag{18}$$

there are three estimation parameters of interest, $\hat{\beta}_0$, $\hat{\beta}_1$, and ν. ν is the stimulus for the binomial test which is inputted with the experimental results. The values for $\hat{\beta}$ are directly dependent on the number of fitment parameters applied to the regression model. In the case of ballistic testing there is only one stimulus, the velocity. as such the values of $\hat{\beta}_0$, $\hat{\beta}_1$ represent the constant linear fitment coefficient and the velocity linear fitment coefficient[24]. These values contain the parameters of interest for the experimenter, μ and σ. The derivation of these parameters from the coefficient values is presented in a simple manner by Collins for the logistic and probit link functions. These relationships are presented in Eqs. (19) and (20)[23].

$$\hat{\beta}_0 + \hat{\beta}_1 \nu = \frac{\nu - \mu}{\sigma} = -\frac{\mu}{\sigma} + \frac{1}{\sigma}\nu \tag{19}$$

$$\theta = \begin{bmatrix} \mu \\ \sigma \end{bmatrix} = \begin{bmatrix} -\hat{\beta}_0/\hat{\beta}_1 \\ 1/\hat{\beta}_1 \end{bmatrix} \tag{20}$$

These results are provided without the use of a standardized stimulus. In practice, a standardized stimulus is utilized to avoid instabilities in the solution computation.In a similar manner the estimated parameters can be used to determine μ for the c-log-log link as seen in Eq. (21)[24].

$$\mu = \frac{ln(-ln(1-\pi)) - \hat{\beta}_0}{\hat{\beta}_1} \tag{21}$$

The value for σ is not calculated for the c-log-log link but could be extrapolated as needed. Neither Collins nor the NIST reference σ in comparing the link functions suitable for ballistic data. One reason for this is the asymmetry of the c-log-log link not being directly comparable to that of the logit and probit functions[23, 24].

With this in mind, the logit and probit function both promise greater utility over the alternative, but the quality of the regression has not been addressed.

Before selecting the preferred regression model, it should be noted that the NIST authors suggest applying multiple regression models to ballistic limit testing. They suggest the logit and probit link functions are the preferred functions for a standard set of ballistic data[24]. This is due to the symmetric nature of these curves, which naturally are defined between zero and one akin to the responses for a binomial experiment. The probit model specifically models the standard normal distribution with a mean of zero and one standard deviation for standardized data. The logistic regression model is similar with a standard deviation of 1.8[24]. This shifts some of the probability from the median value of the regression to the outer probabilities compared to the probit regression model. For ballistic limit testing at V_{50} there is hardly any discernible difference between all three methods suggesting the endpoint treatment at the extrema is the only significant source error between the models[24]. To visualize this result, Fig. 6 from the NIST document provides estimates for the response curve using all three GLM link functions. Despite the similarities presented, there are criteria to distinguish the link functions further.

Goodness-of-fit statistics are standard statistical tools to validate the curve fit applied to a given data set. In the case of GLM estimations, there are five common criteria used to assess the regression. Akaike's Information Criterion, AIC, is calculated based on the number of parameters included in the model and the log-likelihood function. This statistic is conveniently provided as part of the GLM for multiple statistics software packages. The smaller the value of AIC, the better the model fit. The scale for AIC is not global and changes from data-set to data-set, making it helpful in comparing link functions for a single ballistic test only. The log-likelihood method is an additional goodness-of-fit metric, but it is claimed to be

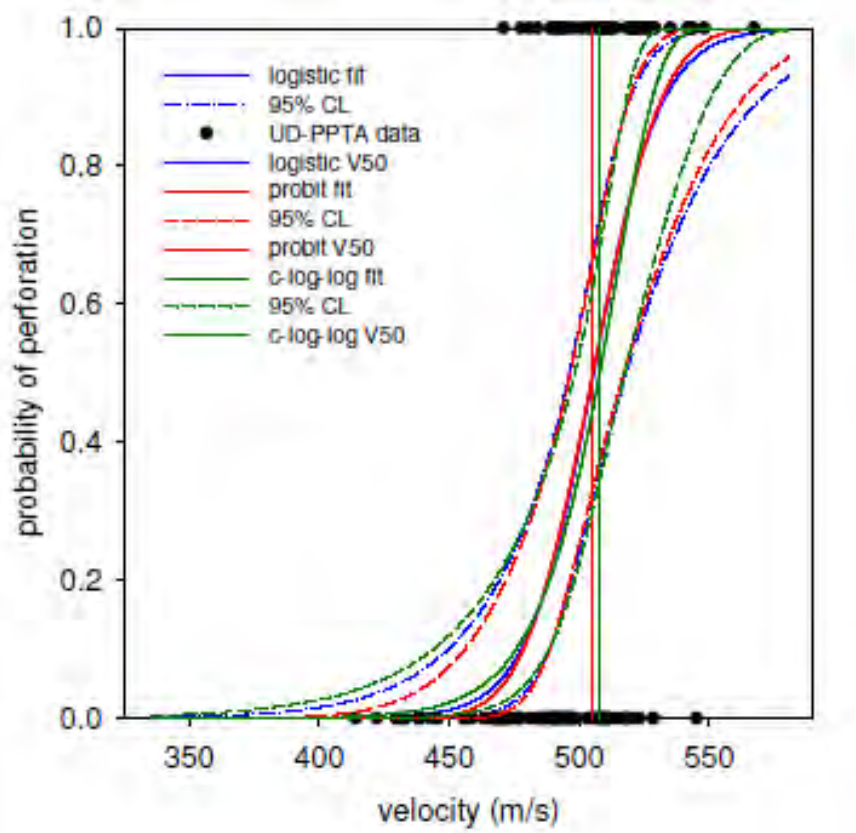

Figure 6: Estimated GLM Response Curves for Logit, Probit, and C-log-log Links[24]

inferior to AIC due to the potential for bias[24]. The deviance of a model measures the difference between the fitted values and the experimental observations, with zero deviance showing an exact fit. The final two methods for distinguishing potential fitment models are prediction error rate and cross-validation. The former utilizes all of the provided data to test data points for misclassification, that is, error between the expected and predicted values. This could lead to underestimating the error rate as all of the data built the model. Cross-validation corrects this potential bias by grouping the data into subsets then generates a model after training the model with one of the subsets removed each iteration. The omitted data set is then used to assess the error rate for the model[24]. These statistics may inform the experimenter of an

optimal model for the data, but a practical application is still required for appropriate use.

2.4 Comparison of Ballistic Testing Techniques

Several comparative studies exist to assess the validity of ballistic test methodologies. An early example of such tests was conducted across six DoD test centers to assess repeatability utilizing MIL-STD-662E. The authors suggest two different sources of discrepancy: extrinsic and intrinsic[25]. Extrinsic discrepancies are variations in test methodologies and practices from test center to test center, while intrinsic discrepancies naturally occur from a test article to a test article. Ultimately the investigation suggested standardization and frequent calibration of equipment to limit extrinsic discrepancies. It also suggested improvements to the selection of test velocities for materials to avoid significant discrepancies in materials with an observed shatter gap dependent on the deformation of the penetrator[25]. Although research, as presented, exists, it is still common for ballistic systems to be tested in non-standard manners before the required certification tests for the procuring party[26]. This does not necessarily suggest the non-standard tests are ineffective but instead suggests the need to review best practices and update standards as material science progresses. This thesis compared three aspects of ballistic testing: the test methodology, the regression model, and confidence in the presented results.

For a test methodology to be considered for ballistic testing, it must efficiently and accurately estimate the quantity of interest. Of the methodologies presented in Burke and Truett, 3-Pod was suggested for application in DoD testing[16]. Their assessment of 3-Pod identified it as the most robust model compared to Langlie and the Up-Down method, allowing researchers to assess multiple quantiles efficiently. Additionally, they found Phase I of 3-Pod to take between eight and twelve runs to

terminate with the 75th percentile of results requiring fourteen or fewer runs for a variety of initial conditions to include initial conditions skewed from the actual mean and standard deviation[16]. Several sequential methods are analyzed in a similar paper cited by Burke et al. This methodology applied two different stopping criteria to the data, the three and three stopping criteria and the break separation criteria. These criteria were applied to several testing methodologies, including several of the methods presented earlier to assess each model's ability to perform under less than ideal conditions[27]. Throughout the simulation, it was determined that 10.5 runs on average were required to determine the V_{50} with the break separation spotting criteria requiring 1.8 fewer runs than the three and three stopping criteria. When comparing the methods' ability to adjust for bias, both the Neyer method and 3-Pod performed the best overall. Where both the Neyer and 3-Pod were not as effective as the Up-Down method or Robbins-Monro methodologies was reducing the uncertainty of the mean. Johnson et al. contribute this to the number of runs required to complete these methodologies but remind the reader the the Up-Down and Robbins-Monro methodologies were only accurate for good guesses of μ and σ[27]. Considering this analysis, the precision of the Up-Down method and Robbins-Monro techniques is high; however, the accuracy depends on the initial conditions. This assessment is confirmed in an alternate review of ballistic testing methodologies, which further highlights the inability of a single test methodology to accurately and consistently estimate multiple quantiles in a concurrent test series[28].

Analysis of regression models has been discussed previously based on the introduction of regression models from the NIST and Collins in ARL-TR-6022. Little argument is raised against these methods, with several of the previously referenced articles using the Logit or Probit models to generate "truth" data in Monte Carlo simulations of ballistic testing algorithms. Additional articles detailing the effect of

various modifications of the test initial conditions for Up-Down methods also use Logit and Probit models[12, 28, 29, 30]. Of these, Eridon et al. and Tahenti et al. suggest the limitations of applying the assumptions of normality to ballistic testing. In both articles, the researchers signal interest in determining how other underlying distributions may affect the validity of the test results. Eridon et al. appear to suggest simply modifying the underlying distribution to a different best fit distribution and determining the effect on confidence levels[12]. A different avenue for the application of Monte Carlo simulations is stochastic modeling[28]. One such application of this is Bayesian stochastic modeling, but further analysis of this method is left to future research[31].

Confidence testing of ballistic testing has been a subject of recent interest following years of no set standard for approaching variations in V_{50}. Several applications of confidence intervals exist if a maximum likelihood estimate is calculated from μ and σ. The most basic of these confidence intervals are assessed from the asymptotic normal distributions of the maximum likelihood estimates using Wald's statistic[23]. Unfortunately, this test provides limited consistency, presenting additional confidence tests. Improved confidence interval algorithms generate appropriate statistical models from data with and without a ZMR and are generally derived from likelihood ratio estimates[13]. The application of the likelihood ratio estimate is described in detail in the previous reference. The "gonogo" program provides the user confidence testing by utilizing the Fisher Matrix, General Linear Model, and Likelihood Ratio, but little information is provided concerning their applicably[19]. Analysis of the Generalized Likelihood Ratio, (GLR), shows it can be rather simply implemented for a given dataset through Eqs. (22) to (25)[12]. L_{MAX} is the isolated maximum likelihood in the feasible region of interest, while MLE is the value of the maximum likelihood estimate. The first two equations provide the information needed to determine the

test statistic for the hypothesis test of interest.

$$V_{50} = V_{Spec} - \Phi^{-1}(P_{Pen})\sigma \tag{22}$$

$$Confidence = 1 - \frac{GLR}{2} = 1 - \frac{L_{MAX}}{MLE} \tag{23}$$

$$\Delta = -2ln(GLR) = -2ln(\frac{L_{MAX}}{MLE}) \tag{24}$$

$$\chi^2_{CDF}(\Delta, 2) = 1 - e^{-\frac{\Delta}{2}} = 1 - \alpha \tag{25}$$

The second set of equations, Eqs. (24) and (25) represent the test parameters for the hypothesis test statistics. Of note is the application of a two degree of freedom model for the χ^2 test statistic. This differs from what is suggested by both of the Collins references but is validated in the Monte Carlo simulations of Eridon et al[12].

2.5 General Material Properties

Classifications of material properties are essential for designing and treating potential ballistic armors. Four material descriptions could potentially describe the physical composition of composite material: homogeneous isotropic, homogeneous anisotropic, non-homogeneous isotropic, non-homogeneous anisotropic. Homogeneity in material science is concerned with the ability of a material to be separated into its components by physical means. This does not exclude composites, as materials, like ceramics, are composites but are homogeneous with a unique yet essentially isotropic response to ballistic stimuli. As far as isotropy is concerned, the material congruence is neither necessary nor sufficient to declare how material effects ought to be modeled[32]. This complicates the modeling of composites by necessitating experimental observations to determine the correct assumptions for a particular material. This is not to say other materials models, such as those for metals, do not require experimental results

but rather provide insight into the present and historic difficulties to determine appropriate numerical and analytical solutions to composite failure mechanisms. By definition, a model represents a particular object or system of thought. It is not the thing it represents and thus has differences that allow it to be scaled and modified for a purpose. The more realistic the model is, the more closely it resembles the physics and mechanics of its subject. The vast array of composite materials and their unique energy dissipation methods distinguish them from traditional materials forcing higher fidelity models and reanalysis of simplifying assumptions. Some of these factors are discussed further in later sections. However, the primary purpose of this section is to distinguish the failure mechanisms of metals that are primarily homogeneous and isotropic to the damage mechanisms of the composites of interest for this thesis which are non-homogeneous and anisotropic.

2.5.1 Failure Modes for Metals

Before introducing the failure modes for metals subject to ballistic impact, it is necessary to limit the scope of this analysis further. The testing for this thesis is not intended to model all types of impacts or projectiles. The velocity ranges for impact in this thesis are relatively low, where the structural dynamics of the target are more impactful to the final result than potential penetrator impact dynamics. Therefore, it can be reasonably assumed that elastic strain keeps the penetrator and the target material in contact throughout the impact event[33]. Dynamic penetrators such as shaped charges, explosively formed projectiles, or deformable projectiles were not assessed. The relationship between the maximum penetrator thickness and the target thickness is a critical limiting assumption. Four general classifications of targets are presented by Zukas when introducing impact dynamics: semi-infinite, thick, intermediate, and thin[34]. The classification from semi-infinite to thin is based on

the interaction between the material and the projectile, meaning that a thick target against one threat may be a thin target to another. The relationship between the target material local to the point of impact and distal regions constitutes the parameter for material thickness classification for the ballistic event. Semi-infinite materials do not influence the distal boundaries, while thin materials do not have any stress or deformation gradients throughout their thickness in a ballistic event. Intermediate thickness targets are of interest for this thesis meaning the rear surface of the target plate is expected to influence the deformation of the material, but there is expected to be a gradient in the witnessed stresses and deformations in the material. The thickness of the material was important for describing general material failure modes in post-impact analysis.

In ballistic analysis, metals are generally used to standardize new material results and provide a comparative base from which to begin analysis. It is granted that all metals do not perform in the same manner, but most can be generally compared to either steel or aluminum with some scaling of the properties to represent the material of interest. Analysis of the failure modes of metals compared to the failure modes of laminar composites provides relevant background when describing the difficulties of modeling composite ballistic dynamics and the need for relevant experimental data to assist in developing models.

Metals tend to fail in at least one of five common damage modes or a combination thereof. The first of these modes is plugging. Plugging results from impact by a generally hemispherically shaped projectile near the target's ballistic limit velocity[34]. Plugging is a shear failure that begins with projectile deceleration and a portion of the target mass being impacted accelerating. This process continues due to localized heating which propagates the shear along the surface area of the newly formed plug. At maturation, the plug and the penetrator move through the material at the same

velocity until the plug clears the rear thickness of the material or all remaining energy is dissipated from the moving mass[34, 33].

A similar damage mode for ductile materials is piercing. This failure mode is generally self-explanatory as the projectile shape allows it to pierce the material, like a wedge, displacing the target material and creating a local compression zone as the penetrator passes through the target. Unlike plugging, shear failure does not occur in the local impact zone resulting in a displacement of the target mass. This damage mode generally occurs at velocities below or significantly above the ballistic limit. Should the impact occur near the ballistic limit, an alternate damage mechanism, petaling, is more likely to occur. Petaling is characterized by high radial and circumferential stresses following the initial stress wave due to the shock upon impact. As the penetrator passes through the target material, plastic flows of material in the high-stress regions form until the material's tensile strength is reached. At this point, cracks form in the material creating sectors that are pushed out of the target and bent into petal-like shapes[34].

The above damage mechanisms are most prevalent in ductile metals and generally result in large fragments from the target as the target material begins to break apart due to the stresses from the impact. Two additional damage modes, scabbing and spalling, result from shock dynamics within the plate. These effects can be reviewed in far greater detail in the provided references, but only a basic description of the event is necessary for this review[33, 35, 36]. Spalling results from the rarefaction wave resulting from the initial shock wave reflecting from the rear of the target. The rapid transition from intense compression due to impact to tension from rarefaction leads to the material fracturing in tension, creating spall on the exit plane of the target[33]. Similarly, in scabbing, material defects resulting in an anisotropic region being significantly deformed may cause a section of the target material to break off

along a fault line generated from the incongruities in the material. This damage mechanism looks similar to the result of spalling but is primarily initiated due to compressive failures[34].

As a summary of the above damage mechanisms, Fig. 7 shows an example of some of the potential damage mechanisms in metals. These damage mechanisms generally represent the expected results for homogeneous and isotropic materials. Mathematical representations of many of these damage mechanisms exist, but the combined effects of these mechanisms make it difficult to generate a solvable expression for a combination of failure modes[33].

2.5.2 Failure Modes for Composites

While the failure modes for metals shed light on the overall mechanics of a ballistic impact event, significant assumptions and highly variable mechanics require significant attention for designers to produce a high fidelity model of their armor. Composite materials complicate this matter further, especially when constructed in

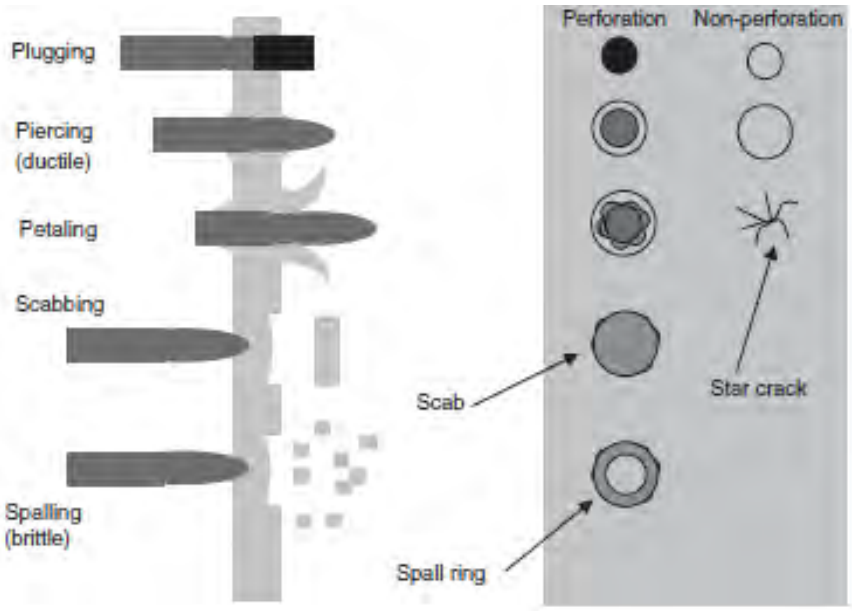

Figure 7: Traditional Material Failure Modes Under Ballistic Impact[33]

a plied configuration where the assumptions of homogeneous and isotropic materials are no longer valid. A degree of reprieve is granted if the composite is isotropic as scaled equations for metals can provide some estimate of composite performance[33]. As early as 1972, composite failure modes were analyzed and categorized as being dynamic and different from metals. Some of the composite failure modes referenced at that time were filament debonding, filament buckling, filament sliding, filament fracture, and shear buckling[32]. Several of these failure mechanisms are based upon the individual fibers which constitute a single composite lamina. Expanding these damage modes to a composite sheet of several plies and a fabric grid with thousands of fibers adds a level of difficulty to modeling, an already highly dynamic and computationally intensive event.

Composite materials are specially designed to dissipate energy. As with many physical events, detailed energy transfer analysis and its relation to material deformation are tedious and computationally expensive. In addition to the aforementioned damage mechanisms for composites matrix cracking, delamination, spall, and other damage modes presented in Fig. 7 all contribute to dissipating the energy from impact. Unique to laminar composite materials is the energy dissipated through delamination. The rate of delamination and its extent is dependent upon material stiffness, impact velocity, and whether the resulting impact yields a C_P or P_P, as well as other factors[33]. While delamination ultimately contributes to a reduction in overall material load-bearing capacity, it enhances the ballistic resistance of composite material during the ballistic event[33]. This is accomplished by transferring the energy into material fibers beyond the local region of impact. The elongation of material fibers is ultimately limited by material shear and tensile strengths but allows a greater amount of the composite material to be engaged, creating the distribution of force and dissipation of impact energy. The generic results adapted from Carlucci in Figs. 8 and 9

further explain the effect on delamination on composite armors. First, the amount of load supported by the material varies throughout the delamination process. This complicates the formulation of predictive equations for delamination growth and ballistic performance. Although delamination itself is not a critical design parameter, if a material delaminates significantly throughout a majority of its vulnerable area, how does this impact its ability to stop secondary threats or multiple hits? Similarly although it is known C_P's and P_P's create different delamination responses due to changes in the material energy dissipation response it remains a highly nuanced specialized process to model either the ballistic limit or delamination through finite element models[33]. As seen in Fig. 8, the progressive delamination response requires codes to average the expected response between lamina or model each lamina with several constraints to create a realistic model. This increases the computational requirements compared to homogeneous and isotropic materials and makes analytical methods extremely difficult to scale to a workable size.

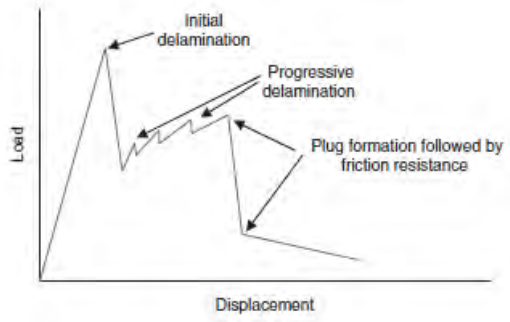

Figure 8: Load-Displacement Curve for a Generic Continuous Fiber Reinforced Composite[33]

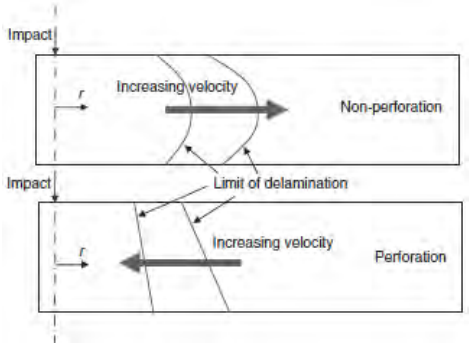

Figure 9: Composite Delamination with Respect to Velocity for both C_P's and P_P's[33]

2.6 Analytical Methods for Estimating Ballistic Events

The preceding sections of this literature review have focused on the history of ballistic testing and common standards relevant for experimental testing. Little has been discussed on estimating the ballistic performance before testing or generating an appropriate estimate for testing an unknown material. The following sections addressed these issues briefly by presenting analytical and experimental research. These detail the current state of ballistic testing for composites as well as highlight limitations and the present need for additional data to build confidence in various theoretical estimates of ballistic performance. Detailed derivations of the methods and techniques used to derive the methods presented can be found within their respective source documents. The emphasis for this section is on the model assumptions and, ultimately, their ability to predict ballistic events accurately.

For this thesis, analytical solution methods are ones in which algebraic expressions, differential equations, or a combination thereof are solved numerically or in a closed-form solution. These methods are different from those considered numerical modeling because they are not reliant on finite element analysis or numerical simulation. As a result, analytical methods are expected to be rough estimates of the ballistic events they model, providing the designer an estimate of their proposed armor's characteristics. These solution processes also provide valuable insight into the mechanics of the ballistic event, valuable for understanding the peculiarities of composite performance.

Analytical Models are most commonly developed from the principles of conservation of energy and wave propagation theory, but some additional models apply the conservation of momentum in their solution process[37, 38]. Approaches of this nature are reasonable to assess the outcomes of a ballistic event without the need to propagate stress-strain dynamics in an element-wise manner. Literature shows en-

ergy methods to be favored in the development of analytical models. These models provide the means to estimate significant damage modes and explain the relationship between damage modes and the overall energy dissipation. This maximizes the utility of an analytical method while providing the designer insight into the design space for the optimal armor solution. To model the transfer of energy from the projectile to the target, either wave theory or conservation of momentum are used to propagate the energy state of the event through completion. Conservation of momentum is generally applied for thin composites as the effects of the gradients through the material are assumed to be minimal[37, 38, 39].

Models for thick materials where a gradient is expected to develop, apply wave propagation theory to determine the current energy relations in their respective models. Two waves propagate through the target material upon ballistic impact, a longitudinal wave, and a transverse wave. The longitudinal wave develops first and is the faster of the two waves. It propagates along the primary yarns impacted by the projectile and initiates the tensile strain damage mechanisms following the compression from the impact[37, 40]. In a related manner, the transverse wave propagates following the longitudinal wave. No additional tensile strain is added in this wave, but the yarns are redirected from perpendicular to the projectile to parallel as the wave passes[40]. This acts to expand the influence of the impact from the primary yarns to secondary yarns in a characteristic "V-shaped" delamination[41]. The following figure from Langston provides a visualization of wave formation in an impact event. From this point forward, the treatment of wave propagation in each model is subject to the model's assumptions. Additional considerations for wave attenuation, decreases in wave velocity, and the treatment of stress-strain relationships impacted by wave dynamics are subject to the objectives of the analytical methods and the trade-off between computational efficiency and accuracy. For example, analytical methods

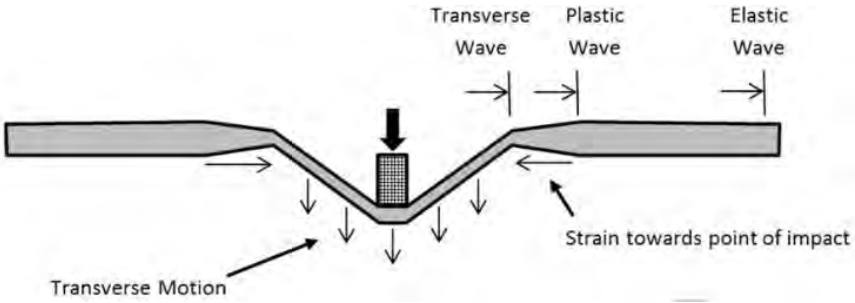

Figure 10: Wave Propagation under Ballistic Loading Adapted Langston[40]

designed to estimate targets with embedded nanoparticles are concerned with wave attenuation better to assess the performance of the nanoparticles[42]. This additional level of analysis requires additional computing power but increases the model's fidelity for a specific application. Similar models without attenuation result in relatively simple second-order differential equations which are solvable via numerical methods[43].

Ultimately, the selection of the proper model is bound by its ability to faithfully represent the event and provide insight into the damage mechanisms for the ballistic event. Uncertainties in the dynamics of the damage modes such as shear plugging, matrix cracking development, and composite fibers' elongation require high fidelity modeling on a microscopic scale. At the same time, analytical methods assess the ballistic event in a macroscopic manner. While wave theory determines how the stress-strain relationships propagate through most models, conservation techniques allow for reasonable estimates for the significant energy dissipation methods of the assumed initial conditions. For most dissipation modes, the extent of failure can be related to the number of composite plies defeated by the projectile. The extent of composite delamination does not assess damage modes such as delamination. Several articles detailing damage modes and their contribution to energy dissipation find results directly from delamination to be minor[37, 39, 41, 43, 44]. This finding does not

discount the value of delamination to composites. Damage mechanisms that do not dissipate significant amounts of energy yet must be designed against can be difficult or computationally expensive to model in analytical methods. This is part of the reason analytical models tend to assess estimates for the ballistic limit but not secondary effects. It also highlights the necessity of supplemental testing to understand a ballistic event beyond the estimates of analytical methods. Consequently, analytical methods are used to develop a general understanding of the ballistic event, with experimental results providing the final viability assessment for a given application.

The primary energy dissipation modes are variable based on the relative thickness of the armor and the projectile. This relationship is the subject of Alonso et al. and manifests itself in the geometry ratio, which is the ratio of laminate thickness to projectile radius[43, 39]. Determining the point at which a composite armor transitions from thin to thick affects the proper attribution of damage modes for composite failures. The critical geometry ratio at which composite armors transition from thick to thin models occurs at approximately one[43]. In general, the majority of energy in thin composites is dissipated through fiber failure, and fiber elastic deformation[38, 39, 43]. Thick composites tend to have similar primary energy dissipation modes with the addition of shear plugging, frictional effects, and compression in the immediate impact regions[37, 43]. These damage modes are the primary modes of energy dissipation for thick materials accounting for approximately 90% of energy dissipated in some models[43].

In a comparison of material effects on the primary energy modes, data was available for E-glass fiber, carbon fiber, aramid fibers(Kevlar®-29), and UHMWPE. A broad generalization of the results shows similar energy dissipation trends for all fibers. The primary energy modes change based on the initial conditions of the analysis, but the shape of the curves tend to be similar. This is especially true of

results modeling $P'_P s$ and $C'_P s$ near the ballistic limit. Energy from the deformation caused by transverse wave propagation, shear plugging, and bending represents the initial primary damage modes from the ballistic events for E-glass fibers. Over time, the energy dissipated from the secondary yarns supersedes that of the other modes for partial penetrations, but not complete penetrations[41]. For thin carbon fiber plates, the energy dissipation is dominated by cracking, momentum transfer, and fiber failure[38]. Of note between these two materials is cracking as the primary energy dissipation mode for carbon fiber materials. Cracking limits the ability of a material to deform in the plastic region, limiting the amount of energy dissipation through material deformation, accounting for the differences between the two materials. The material failures are thus related to the material shear strength and Young's modulus to drive significant failure modes. This is further evidenced by comparing aramid fibers to the previous results. Unlike the previous results, the dissipation by secondary yarns rapidly eclipses the energy dissipation from deformation due to the transverse wave. No other damage modes contribute in a significant manner to the overall energy dissipation[41]. This result is similar to that of UHMWPE, but delamination was also a significant source of energy dissipation[40]. The driving mechanism behind these differences again appears to be the materials' shear strength and Young's modulus. Further comparison of the analytical models and their results are limited by inconsistencies between the materials and projectiles simulated. To gain further insight into material performance, additional testing against standardized stimuli is recommended.

Standard projectile simulators are flat-nosed cylindrical shapes and spheres which do not deform or erode in any way throughout the ballistic event. These rigid projectile models are appropriate for several conditions, but when modeling jacketed bullets, they tend to underestimate the ballistic limit due to failure to account for

projectile deformation[45, 44]. Accounting for these effects modifies several assumptions used to simplify the solution model to be feasible for mathematical programs such as MATLAB. This does not make the problems unsolvable in analytical form but does further distance the solution method from algebraic or closed-form solutions to differential equations as in Naik and Lopéz-Puente[37, 38]. Modeling improvements detailing the reality of projectile deformation in projectile such as soft-core bullets are applicable in several threat environments. They also enhance understanding of the overall ballistic event, but this level of analysis is not necessary for the scope of this thesis. Should the projectile be modified for future testing such that deformation is likely, these results may be of interest.

2.7 Motivation for the Current Investigation

The motivation for the present investigation stems from the work of Kinsler and Collins on the multi-hit analysis of UHMWPE. Their investigation began with the observation of a qualitative increase in the velocity needed for a C_P of the second impact when delamination overlaps occurred[1]. This finding suggests there may be a significant variation from a composite test plate undamaged and one that has a follow-up shot within the delaminated region of a previous shot. Should this relationship be found significant, the implications resonate throughout the survivability community. Ballistic impacts are considered independent events when assessed in modeling software and survivability estimates. Impact events within a certain radius of a damaged region are expected to provide significantly worse protection than those in fair locations. Two examples of this are how MIL-STD-662F and STANAG 2920 define a fair hit. The former states a shot must be two projectile diameters from any previous impact or observed damage, while the latter states a distance of five projectile diameters is required for a fair hit[4, 10]. To visualize how this may be

problematic in composite testing, a comparison is made between homogeneous materials and composite materials in Fig. 11. The green dashed circles represent an idealized delamination region in a generic composite material. In certain armors, like UHMWPE, the delamination may not be detectable to the naked eye making it possible for a fair hit by either standard to result in a higher V_{50}.

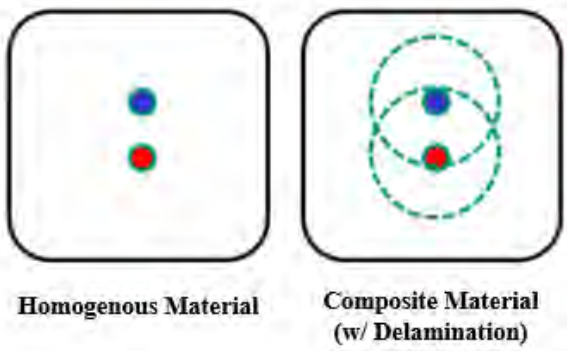

Figure 11: Comparison of Delamination Overlap

Tests from Kinsler and Collins were conducted on three UHMWPE panels from the same manufacturing lot. The baseline V_{50} was collected using the three and three stopping criteria from MIL-STD-622F. Each shot was placed outside of the delamination from previous shots for the baseline test. An acoustic tap test and visual analysis with the plate placed on a light table were used to determine delamination. It is noted that this study did not utilize alternative methods to determine delamination, such as measuring the thickness of the material or using ultrasound. After the initial test series, each subsequent shot required some delamination overlap. The three panels were tested independently after the baseline V_{50} was determined, each having an additional four V_{50} series shot on them. Plates one through three were shot a total of 34, 33, and 42 shots respectively[1].

Ultimately this testing series showed the potential for a shot to shot dependency in V_{50} testing. There were examples of tests being conducted which resulted in a statistically significant increase in the recorded V_{50} followed by a test with the statistically

significant decrease in V_{50}. These results are caveated by their lack of academic rigor in detailing the region of overlap and shot distances from each other. As a result, the paper-primarily highlights a potential concern for future investigation.

The research directly preceding the efforts of this thesis sought to correct the limitations of the study by Kinsler and Collins and sought to isolate potential variables in the testing sequence. After collecting initial estimates for V_{50}, the plates were separated into a group of C_P's and P_P's. The delamination region was determined using a tap test and visual inspection before a secondary set of V_{50}s were shot by placing the second shot within the delaminated region. Based on the second testing phase, the third phase was developed to set the distance from the previous impact constant. This was accomplished by placing shots either 0.25 inches from the previous impact or 0.75 inches from the previous impact. Again the tests were separated between C_P's and P_P's[2].

Keane's research found the potential for an 8.5% increase from the undamaged V_{50} if the secondary shot was in the delaminated region near a P_P. The results signaled there is a dependency between the previous shot result and a secondary shot in the near vicinity, but the analysis was conducted against only one type of composite and using an uncontrolled fragment simulator[2]. As such, additional research is necessary to isolate further the differences between C_P's and P_P's against a common projectile with consistent impact orientation. Similarly, testing against several composite materials would provide further insight into the impact of multi-hit dynamics in composite materials.

2.8 Summary of Literature Review

This chapter provided an overview of ballistic testing techniques, regression modeling, error analysis, and material failure modes. Several test standards were pre-

sented to define the scope of ballistic testing and illustrate limitations in current test methods. Following this assessment, several modern test methods for sensitivity experiments were reviewed and compared with respect to ballistic testing. Regression modeling was addressed to gain insight into proper data analysis and error analysis. This investigation led to further research into material failure modes and the primary modes of energy dissipation in composite materials. Finally, the motivation for this study was addressed to provide the framework for the experimental analysis. The collection of this material provides a firm understanding of the complexities of ballistic testing and the confidence to present a meaningful comparison of several multiple shot V_{50}'s.

III. Methodology

The following chapter details the test methodology used in this investigation. The purpose of these tests is to establish a standardized test procedure to compare several composite materials with V_{50} as the primary focus. The first section of this chapter introduces the test facility. Next, the test matrix is discussed along with the definition of a fair hit and qualitative terminology to describe the projected second impacts. Following this, the test articles are introduced along with an initial estimate for their V_{50}. The fourth and fifth sections detail this investigation's data collection and processing techniques. The final section considers uncertainty analysis for this investigation.

3.1 Test Facility

The testing for this investigation was conducted at Range A on Wright-Patterson Air Force Base courtesy of the 704th test group. The experimental setup comprised a firing control center, a single-stage nitrogen gas gun, and the test section. The fire control station featured in Fig. 12 was comprised of two laptop computers, the fire control group, power supply, and data acquisition system. The laptop computers were used to run real-time data processing through the Phantom Camera Control software. The Phantom v12.1 high-speed camera used in this investigation was connected to the computer via a TP-Link TL-SF-1008D switch. This provides a live link to the camera and controls the camera through the computer. From here, the initial review of the high-speed camera results and video processing through MATLAB analysis takes place between test shots. The details of these processes were further discussed in Section 3.5.1. To determine the velocity for each test, 3-Pod was run via gonogo on R. Once the desired velocity was determined, it was recorded in an Excel spread-

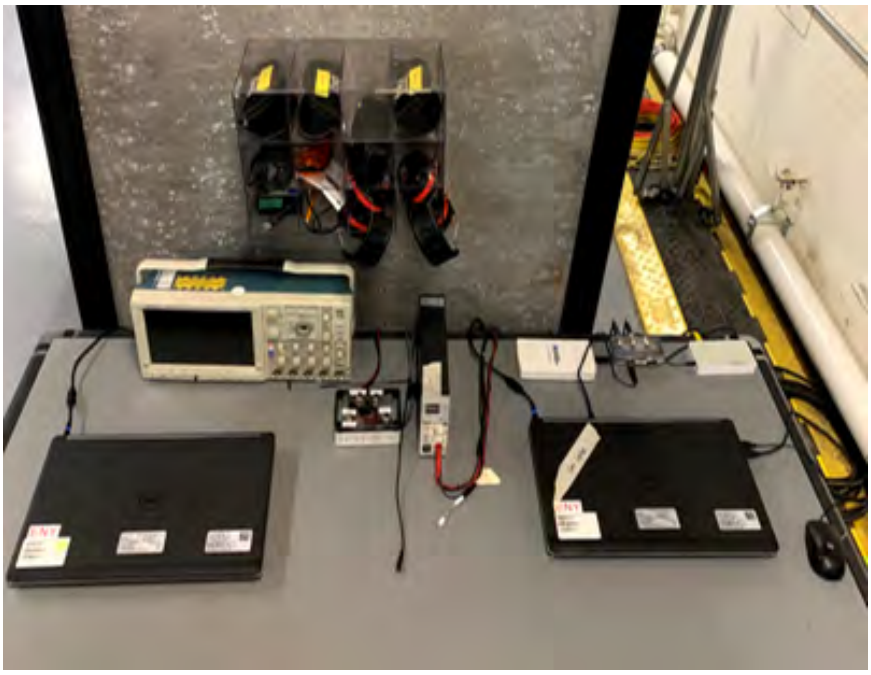

Figure 12: Fire Control Desk

sheet, and the required pressure was determined from a calibration curve fit. The calibration of the gas gun is discussed further in Section 3.6. Finally, the pressure is read from LabView code which converts the pressure transducer signals to gauge pressure through a National Instruments NI USB-6210 data acquisition system.

The fire control group was powered from an Extech 80W switching DC power supply set to 24V for the pressure solenoids and converted to 5v for the firing valve. This setup includes a safety switch that must be armed to fire the gun to provide an extra layer of risk management. Two additional switches command the pressure solenoids to pressurize and de-pressurize the holding tank. The fire control group can be operated without either computer, but the computer is required to determine the pressure within the holding tank. All elements of the fire control desk and the test conductors were located behind a 0.25 inch thick steel sheet secured in a frame constructed from 80/20 aluminum.

The gun consisted of a gas supply source, a pressure holding tank, a firing value,

and a barrel. The nitrogen supply tanks provided 341 cubic feet of nitrogen gas storage apiece pressurized to $2,500$ psi when full. The gas flow was controlled with a Valley National Gases, Inc dual regulator capable of holding $3,000$ psi tank pressure and regulating gas flow to below the $1,500$ psi rated fire control valve. Pressurization and depressurization of the 0.0353 cubic foot holding tank was controlled by a pair of Marotta MV74 solenoids connected to the fire control group. A Sensotec PPG/E981-05-01 pressure transducer provided pressure readings inside the holding tank to accurately predict the firing velocity of the gun. The configuration of the pressurization solenoids and the holding tank can be viewed in Fig. 13 as well as the barrel in Fig. 14. Firing was controlled through an ASCO Red Hat model 8223G003 solenoid valve which connected directly to a stainless steel barrel. The barrel had an

Figure 13: Pressure Holding Tank with Pressurization Solenoids and Firing Valve

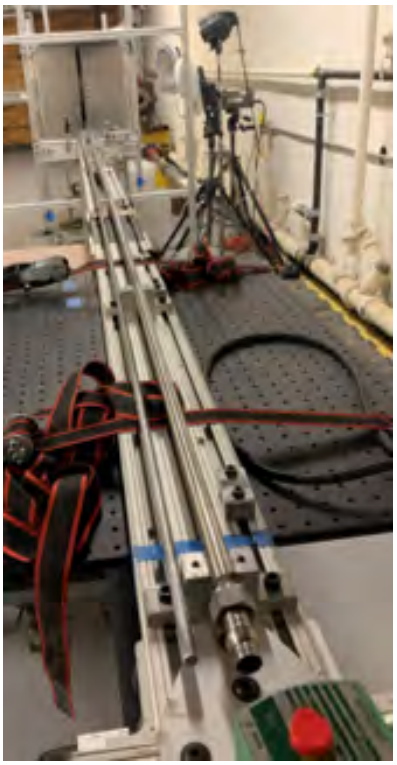

Figure 14: Stainless Steel Gas Gun Barrel 12 **feet Long with a** 0.525 **inch inner diameter**

outside diameter of 0.625 inches and an inner diameter of 0.525 inches and was 12 feet long with a flare fitting to seal the barrel and the firing control valve. The fitting and the value are seen in Fig. 15.

The projectile used for this investigation was a tight-tolerance hardened 440C stainless steel ball-bearing. The diameter of the ball bearing was 0.5 ± 0.0001 inches. A patch was used to seal the ball bearing in the barrel and provide consistent pressure in the chamber. The patch was a Thompson Center 0.45 and 0.50 lubricated round-ball patch. The patches were pre-lubricated with Thompson Center Natural Lube 1000 Plus Bore Butter for smooth loading and firing. Pre-lubricated patches were purchased to eliminate variability introduced by the experimenter. The patches had a uniform thickness of 0.015 inches providing a secure and consistent loading. Loading was conducted by centering the patch and the ball bearing over the muzzle. The ball bearing was then seated into the barrel via thumb pressure before being ramrodded to the end of the barrel before the firing control solenoid. The ramrod was marked to allow consistent loading to the same position in the barrel each shot.

The final element of the ballistic test range is the test section. The test section is a 3 ft x 3 ft x 6 ft container constructed from 80/20 aluminum extrusion. The container walls are 0.5 inch thick polycarbonate sheets except for the front and rear planes of the container. The front plane where the projectile enters the container consists of two steel plates designed to funnel an off-target shot into the test section rather than ricocheting back towards the experimenter. The test section is shown without the chronographs installed before and after the test stand in Fig. 16 with the projectile entering the test section from the right. The test stand is constructed from 0.25 inch steel plates. The stand clamps the test article between the steel backing and a front plate. The bolts are evenly spaced around the test article to provide consistent clamping force around all sides. A sample image of the test stand with a test article is

Figure 15: ASCO Valve Showing Barrel Fitting

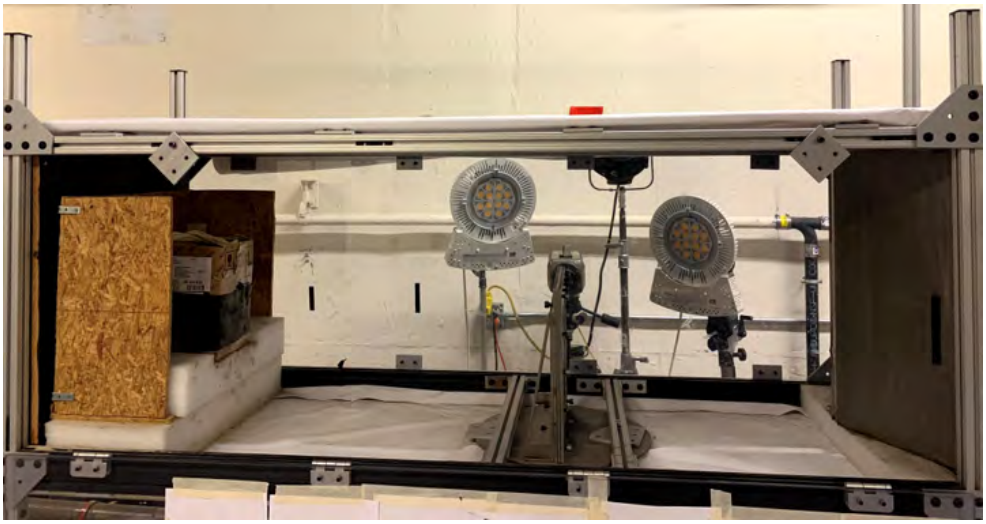

Figure 16: 3' x 3' x 6' Ballistic Test Section with Test Stand Installed

provided in Fig. 17. The test stand is mounted on 80/20 extrusion, which is squarely mounted to the frame of the test section. With the test section placed square to the muzzle of the gas, gun obliquity is controlled by orienting the test stand within the test section. The test stand was mounted square to the muzzle for this test series to provide a zero obliquity shot. Two Caldwell Ballistic Precision Premium Chronograph kits collected incoming projectile velocities and residual projectile velocity. If the test article did not arrest the projectile, a box of sand slowed the projectile before two

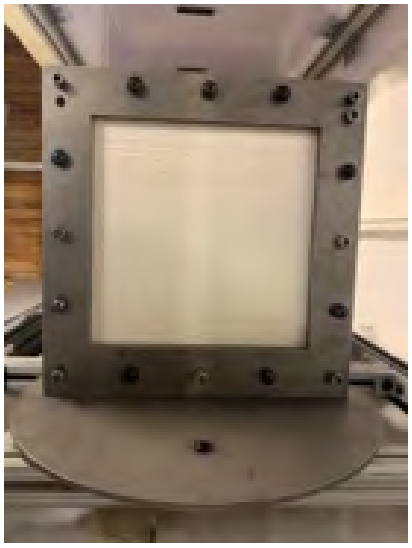

Figure 17: Ballistic Test Stand

0.375 plywood panels coated with truck bed liner. Should the projectile penetrate through the test stand, the rear panel is a 0.25 inch steel plate.

The high-speed camera was leveled perpendicular to the impact plane outside of the test section and centered on the projectile flight line. Three floodlights were focused on the test stand to accommodate the lighting needs for a 3 microsecond exposure time and $39,603$ frames per second. Paper was fastened to the inside of the opposite side of the test section to illuminate the test section further.

3.2 Qualitative Definitions

The following sections detail the qualitative definitions necessary to present the test matrix for the experiment. Lessons from Kinsler and Collins, and Keane were utilized to make the test repeatable and isolate as many design variables as possible. This design approach clearly distinguishes each impact's objective through the designations of close, medium, and far impacts. The definition of these terms is addressed further in this section. Additionally, the projectile used in this study was not constrained by customer requirements allowing a ball bearing to provide consistent

impact not possible when a cubic fragment simulator is used. This research also addresses the need to characterize the effect of delamination over various materials; all tested with the same approach.

3.2.1 Defining a Fair Hit

Several definitions of a fair hit were assessed to standardize the ballistic testing procedure for this investigation. MIL-STD-662F states that a fair impact must come from an unyawed fragment or test projectile impacting an unsupported target region with the specified obliquity for the test. Additionally, the impact must be at least two projectile diameters from a previous impact or disturbed area resulting from damages in a previous impact[4]. This standard is utilized for several materials and armor types without distinguishing between homogeneity or mentioning delamination. A DoD performance specification for an uncharacterized lightweight military armor suggests a fair hit must have an incidence angle $\pm 5^\circ$ of the desired angle with a shot-to-edge distance no greater than 3 inches and a shot-to-shot distance no closer than 2 inches from a previous impact[6]. This standard makes no comments addressing potential damage from an initial shot impacting the validity of the second shot. Other DoD test standards have a similar requirement for shots being two projectile diameters from previous impacts, but the most restrictive defines a fair multi-hit test spacing as a three-shot triangle with side lengths of $4 \pm 5\%$ inches[7, 46]. The applicability of MIL-STD-3038 is limited, though, considering it is a standard for acceptance testing of ballistic defeat materials, not an experimental test standard to evaluate V_{50}. NATO STANAG 2920 separates the concept of a fair hit into a normal impact and the shot location. For the impact to be normal to the target, the incidence angle must not be more than 3° of the intended incidence for bullets and flechettes or 5° for fragment simulators. The impact location must be a sufficient distance from areas of damage

such that damage caused between two tests does not overlap. Should there be visible damage, the impacts of the standard state must be at least 5 projectile diameters away to be included in ballistic limit calculations[10]. NIJ Standard 0101.06 introduces a minimum shot-to-shot distance of 2 inches, but similar to other standards, does not address regions of composite delamination overlap[8].

Based on the above standards, a fair definition is not standardized. It varies depending on the purpose of the test, whether it is a ballistic acceptance test or a test to determine the ballistic limit. Considering the purpose of this test was to characterize the impact of composite delamination on the V_{50} ballistic limit, the recommendations of MIL-STD-662F were followed when assessing the shot-to-shot distance between tests. To properly assess the relevancy of MIL-STD-662F, several V_{50} tests were conducted at distances within the minimum specification, at the minimum specification, and beyond the minimum specifications. These zones were further classified based on the degree of delamination overlap from shot to shot.

3.2.2 Regions of Interest, Multiple Hit Items

The composite armors for this investigation were plied armors. As a result, the material was expected to exhibit some degree of delamination under ballistic impact. Shots were placed either one projectile diameter shot to shot, two projectile diameters from the furthest extent of visible damage, or three inches center-to-center. This spacing was discussed further due to unexpected results from the aramid fiber test articles in Chapter IV. The qualitative descriptors super-close, close, medium, and far were used as shown in Fig. 18 to characterize the relative distance from shot to shot. The green circles represented initial shots, and the red circles were second shots. The delamination was idealized as a circle surrounding each shot. Homogeneous materials represented the standard case where the definition of a fair impact under

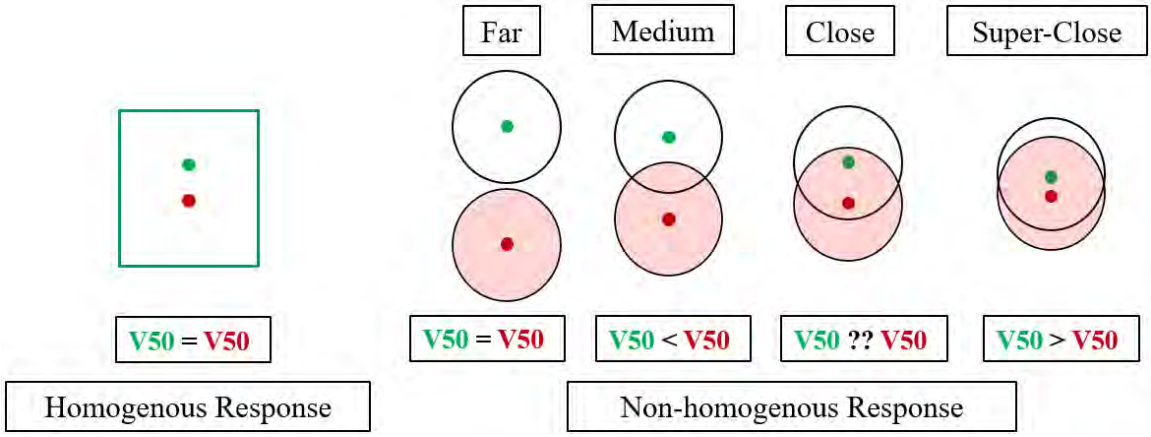

Figure 18: Homogeneous vs. Non-Homogeneous Delamination with Characterization of Delamination Overlap and Hypothetical Effect on V_{50}

MIL-STD-662F was appropriate. The materials, in this case, were assumed to show no delamination, and the minimum shot-to-shot distance was two projectile diameters from any previous damage. The composite armors tested were expected to exhibit characteristics of non-homogeneous materials. Additionally, under each case, the hypothetical effect of shot placement on V_{50} was listed. These hypotheses were made according to the results of Kinsler and Collins, and Keane. In all cases, except for C_P close second shots, there was expected to be no significant difference in V_{50} between C_P and P_P initial shots.

3.2.2.1 Super-Close Impacts

The closest two shots that might be placed were the super-close shot. These shots were expected to be within highly damaged portions of the material where the ballistic resistance of the material was severely degraded. Shots of this nature exhibit are both placed within the previous extent of material delamination as depicted. Due to the expectation that the armor would be severely weakened in this configuration; no shots were taken with this descriptor. Shots of this nature may be applicable in the testing of thick armors, and the hypothesis that the material would be severely

weakened would be most accurate for thin plates.

3.2.2.2 Close Impacts

Close impacts were those taken outside of the immediate damage from the previous impact but within the two projectile diameter specification of MIL-STD-662F. In this region, the damage from delamination was expected to overlap both the initial and secondary shots, but this was not a requirement if the material exhibited minor delamination for the visual and audiological assessment of the delamination extent. In this region, it was hypothesized that the V_{50} would be decreased from the clean V_{50} value if the initial shot was a C_P, but increased if the first shot was a P_P. This hypothesis is based upon the results of Keane, and the expectation overlapping delamination increases the value of V_{50} so long as the target plate is not critically damaged.

3.2.2.3 Medium Impacts

Medium impacts were those with a minimum shot-to-shot distance pursuant to MIL-STD-662F. In this region, some degree of delamination overlap was expected. The delamination was not expected to overlap the previous impact location as in the close impacts. In this region, the V_{50} is expected to increase compared to the clean V_{50} for both the C_P and P_P initial impacts. This hypothesis is again consistent with the findings of Keane.

3.2.2.4 Far Impacts

Far impacts for composite armors shall exhibit no delamination overlap. This standard is consistent with the minimum shot-to-shot distance described in STANAG 2920. These impacts were expected to be dependent events; therefore, no change from

the initial V_{50} was expected. The minimal distance for this spacing depended on the average delamination the composite armor is expected to exhibit. Far impacts were assumed to be the same as the clean configuration and treated to maximize the utility of the test articles.

3.3 Test Matrix

For each of the four composite materials, 25 plates were available for testing. Of these plates, 24 were selected for ballistic testing. Two plates were used to confirm the range of a high and low estimate for V_{50}. The minimum criteria for successful test completion were to shoot enough initial V_{50} tests to complete one of each of the following: C_P close, P_P close, C_P medium, and P_P medium. Each V_{50} series was expected to take twelve shots using the 3-Pod methodology. Should Phase I of 3-Pod be completed in less than twelve shots, the remaining shots were allocated to Phase III to increase confidence in the estimate for V_{50}. The schematic in Fig. 19 shows a visual break out of the test series. Each plate was initially shot once with the shot placed 3 inches from the bottom of the test stand and 3 inches from the side of the test stand. This location centered the shot within the lower right quadrant of the

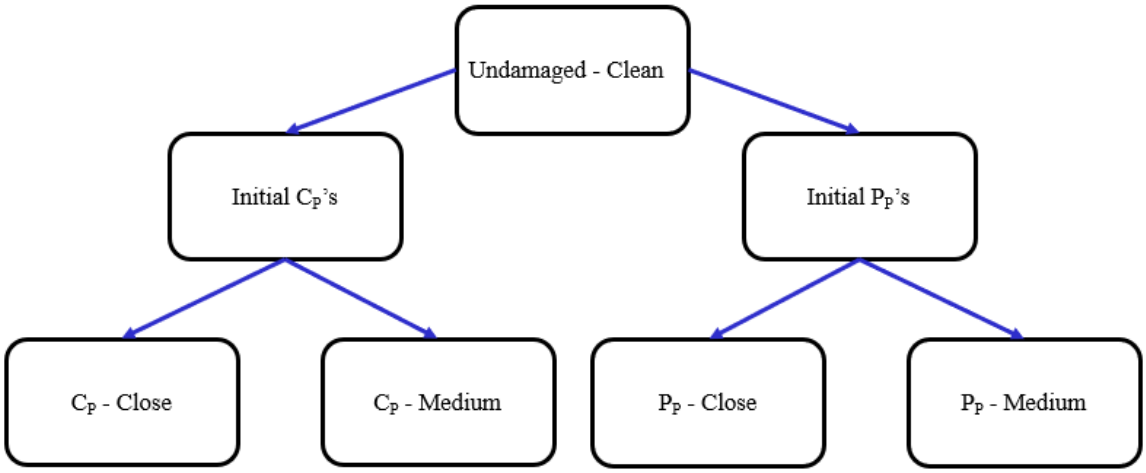

Figure 19: Ballistic Testing Test Matrix

plate. Following the initial V_{50} series, each plate was reshot in the opposite corner. This process was repeated until each plate had four clean shots and four clean V_{50} shot series were recorded. Each shot was indexed by plate number, shot number, and the response, C_P or P_P. Next, test series dependent, either a C_P or P_P was selected, and the test stand was positioned such that the secondary shot was placed in the secondary yarns of the initial impact the designated distance away from the initial impact. A maximum of eight shots was placed on each plate. A visual depiction of a completely shot test article is provided in Fig. 20. As configured, this sample plate was used to test both medium and close impacts. The green circles are the initial shots, and the red circles represent the second shots. In theory, each secondary shot could be a part of a different V_{50} series. The purpose of placing the secondary shots on the secondary yarns was to increase the probability that the second shot would not fall on fibers that had failed under the previous impact. Following the completion of the initial series of eight V_{50}'s, the results were reviewed, and tests were repeated on runs with unexpected results or large standard deviations.

The above methodology details the idealized test matrix for the investigation. This process was utilized for the carbon fiber and glass fiber plates. An alternate test methodology was applied for the aramid fiber and UHMWPE plates due to delamination extending beyond the 3 inch shot to shot distance. Only 2 shots were taken against the UHMWPE plates. These shots were taken at the maximum pressure for the gas gun setup and resulted in P_P's. As such, it was determined that the AFIT gas gun setup was insufficient to provide C_P's, and testing was abandoned for this material. Further discussion for this material is provided in Chapter IV. Following the initial test shots on the aramid fiber plates, it was determined that delamination on the back-face of the material prevented multiple clean shots on a single plate. To maximize the potential of the remaining 21 plates, two separate

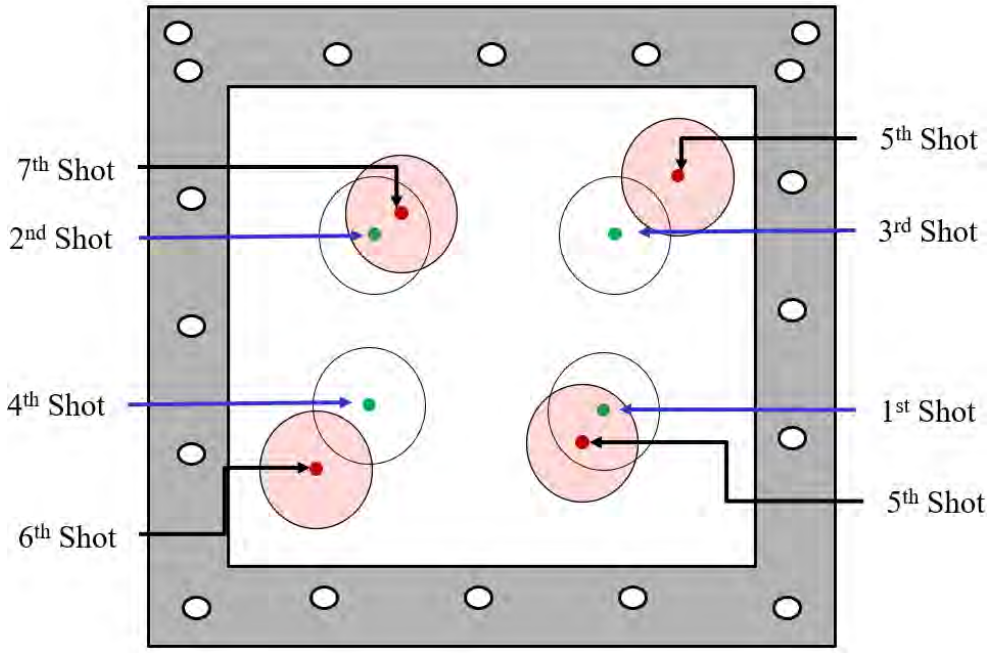

Figure 20: Example of a Shot Grid on a Completed Test Article

V_{50}'s were shot using the 3-Pod methodology. Each shot was placed slightly off-center to allow for a secondary shot without the edge of the test stand limiting the extent of the delamination. Once this testing was complete, the plates were separated into C_P's and P_P's and tested with a medium shot placed 2.5 inches shot-to-shot distance from the initial impact. This distance was selected such that the second shot was not placed within the delamination of the first shot. The delamination regions overlapped as defined for the close shots on the back-face. Under this configuration, V_{50} was hypothesized to be greater than the baseline V_{50}. After this testing was complete, a final V_{50} was shot with each shot spaced in the same manner as the clean shots on the carbon and glass fiber plates. This test series placed each shot in the delamination region of a former shot except for the initial impact on the plate. This V_{50} was hypothesized to be the largest V_{50} of the aramid fiber test series due to the compounding delamination effects.

3.4 Test Articles

The test articles for this investigation came from four different families of composite materials: carbon, glass, aramid, and UHMWPE. Each test article had a thickness of 0.25 inches. Where possible, all composites had the same weave and were laid up uniformly. This was possible for the carbon and aramid fiber plates. Each of these plates was composed of plain weave fibers. The glass fiber plates were made from 8 harness satin weave (8HS) fabric, and the UHMWPE plates were made from a unidirectional material in a 0°, 90°, 0°, 90° lay-up. The plates can be viewed in Fig. 21. General material properties are provided in Table 3. The impact of each material on the expected value for V_{50} will be discussed in each materials respective subsection. The matrix material for each material was also standardized were possible. Both the glass and aramid plates used AF163 as the matrix material. BT250 was the matrix material for the carbon fiber plates, and the UHMWPE sheets came with a urethane resin matrix pre-embedded in the material. This thesis is not developing new materials or assessing a novel processing technique; therefore, the following material descriptions are designed primarily to address the hypothesized range of V_{50} for 3-Pod and provide enough information to provide explanations for experimental observations.

Table 3: Test Article Properties

Fiber Material	**Matrix Material**	**Style Number**	**Weave**	**Areal Density,** lb/ft^2	**Thickness,** *inches*
3K Carbon	BT250	282	Plain	1.88	0.25
S2 Glass	AF163	6781	8HS	2.12	0.25
Kevlar® KM2	AF163	706	Plain	1.24	0.25
UHMWPE	Urethane	Spectra 4232	UD	1.27	0.25

Figure 21: Composite Test Articles, Left-to-Right: S2 Glass, SS 4232, 3k Carbon, and Kevlar® KM2 600 Denier

3.4.1 Material Properties

Although no material properties of the fibers used in this investigation were tested, an effort was made to collect relevant material properties to distinguish the composite materials from each other. Material properties were available for all fibers except UHMWPE. The UHMWPE plates used in this investigation were Honeywell Spectra Shield® 4232. Of the limited available information provided by Honeywell, it is stated that the product does not ship if V_{50} is below $1800 ft/s$[47]. No additional information on the thickness of the plate with a minimum V_{50} of $1800 ft/s$ was provided, but Honeywell's quality control process is available on request. Similarly, no information was available on the material's tensile, compressive, or flexural strengths. No data was available for the maximum strain to failure. Although no data was available for this particular UHMWPE, information adapted from Hexcel's *Technical Fabrics Handbook* was presented in Table 4. The estimated performance parameters were based on Spectra 900, Spectra 1000, and Spectra 2000. The performance of Spectra

Table 4: Physical Properties of the Test Articles[48]

Materials	**Density** lb/ft^3	**Tensile Strength,** Ksi	**Young's Modulus,** Msi	**Strain to Failure,** %
3K Carbon	0.064	530	33.5	1.5
S-Glass	0.090	665	12.5	5.5
Kevlar® KM2, 600 Denier	0.052	497	11.8	3.6
UHMWPE	0.035	348 - 465	11.4 - 16.4	2.9 - 3.6

Shield® 4232 was considered to perform within the range of results provided, but it is likely the material outperforms those presented. All other materials in Table 4 are representative of the materials tested in this thesis. The tensile strength and Young's modulus describe the material strength and the relationship between stress and strain in the material. The higher the tensile strength stronger the plate. Higher Young's modulus suggests less fiber deformation before failure. An optimal material minimizes density, maximizes tensile strength, and has a Young's modulus appropriate for the armor application. Materials with large Young's Modulus are expected to be more brittle than materials with lower Young's modulus. Carbon fiber is expected to be the most brittle of the materials tested, while UHMWPE is expected to be the least brittle. The hypothesized impact of these material properties was that delamination extent increases with decreasing Young's Modulus.

Properties for the matrix materials were available for all materials except UHMWPE. Similar to the fabric properties the tensile strength and Young's Modulus were available for comparison for both materials in unsupported neat resin forms meaning there was no influence from a structural material. Matrix materials that are both strong and flexible maximize the performance of the embedded fabrics. Comparing the materials in Table 5 the most significant difference in performance is the Young's modulus. In general the both matrix materials are expected to perform similarly in the final

Table 5: Physical Properties of the Matrix Materials[49, 50]

Matrix Material	Tensile Strength, Ksi	Young's Modulus, Msi
BT250	10.9	0.44
AF163	7.0	0.16

composite lay-ups. When comparing the carbon plates with BT250 to either the glass fiber plates or the aramid fiber plates, there was expected to be greater evidence of matrix cracking in the carbon plates due to the higher Young's Modulus in BT250. This was expected to reinforce the hypothesis delamination will be greatest in plates with the lowest Young's Modulus.

3.4.2 Ballistic Limit Estimates

Estimates for the ballistic performance of the test articles were derived from the findings of Section 2.6. Considering the majority of the dissipated energy came from fiber failure, fiber elongation, and shear plugging materials with the greatest tensile strength and lowest Young's modulus are expected to have the highest V_{50}. Secondary modes of energy dissipation were based open the ability of the primary and secondary yarns to elongate, suggesting ductile materials performs better than brittle impacts under ballistic loading. Based on this assessment material V_{50} expected to increase in the following order: 3K Carbon, Kevlar® KM2, S2 Glass, and Spectra Shield® 4232. This assessment relies only on the physical properties of the materials but does not address the significance of the fiber weave. Considering the plain weave is stronger than the more pliable 8HS weave due to greater energy dispersal throughout the fabric, the glass fiber plate was not expected to perform as well as a plain-woven aramid of similar physical properties. Therefore, the final order of hypothesized V_{50} has glass fiber performing worse than the aramid but better than the carbon fiber plates.

Estimations for the clean V_{50} were derived from the results of Bresciani et al and Scazzorosi[41, 44]. Neither of these articles tested the same materials presented in this study, but they did provide a reference for the aramid and glass fiber plates. Based on this estimate and test shots which provided a C_P and P_P, the initial conditions for 3-Pod were established. These parameters are presented in Table 6. Following the initial V_{50} series of the aramid plates the upper estimate for μ was adjusted to $850 ft/s$. Similarly, for all materials, σ_g was reduced to $5 ft/s$ following the first test series. No further adjustments were made of the initial conditions regardless of whether the V_{50} was shot against clean plates or previously impacted plates.

Table 6: Initial Conditions for 3-Pod

Material	μ_{lo}, ft/s	μ_{hi}, ft/s	σ_g, ft/s
3K Carbon	550	650	10
S-Glass	600	700	10
Kevlar ® KM2	750	950	10
UHMWPE	Limit Exceeded Range Capabilities		

3.5 Data Acquisition

This investigation's primary data acquisition was the velocity before impact, shot-to-shot distance, and delamination extent post-impact. Although not necessary to meet the experimental success criteria for the investigation, residual velocity was determined where possible. This section details how velocity measurements were taken and the delamination post-impact assessed.

3.5.1 Velocity Measurement

Velocity measurements were taken before and after impact using Caldwell Ballistic Precision Chronographs. These chronographs provided accuracy up to $\pm 0.25\%$ of

measured velocity[51]. Velocity measurements were recorded through Caldwell's app supporting the chronographs. This allowed the readings to be saved between shots and read from behind the blast shield at the fire control desk. An example of the setup within the test section is provided in Fig. 22. Unfortunately, the chronographs are known to be sensitive to variations in lighting. Due to the lighting required for the high-speed camera, there were several instances throughout the investigation where the chronographs failed to record velocity, or the recorded value was not reliable. This was due to the optical sensors used to trigger the chronograph. Similarly, the sensor errantly triggered or failed to record the projectile past both sensors. This made the readings from the chronographs functional primarily as reference velocities to compare with the results from the high-speed camera. This limited the ability to record meaningful residual velocities and was not remedied in this thesis.

The primary mode of velocity measurement came from analyzing the video from the phantom v12.1 high-speed camera. First, a calibration video was taken with a known scale so that the number of feet per pixel could be calculated. Fig. 23 shows the ruler up against the test article in the test stand. The direction of projectile motion was from left to right, and the ruler was centered on the shot-line. This allowed the camera to be focused on the projectile's flight path and maximize the recorded video's sharpness. Once the camera was calibrated, the ruler was removed as well as any other obstructions. The video was reviewed and saved for processing within MATLAB following a test shot. Two functions developed for previous research with the ballistic test calculated the velocity from cross-image correlation. Functionally, the code read the video file and subtracted the background image from all frames. The user then designates a frame of interest and a region of interest to analyze. The projectile velocity was measured $2-7$ inches from the test article for this investigation. Five different velocity measurements were taken, with seven frames between the two

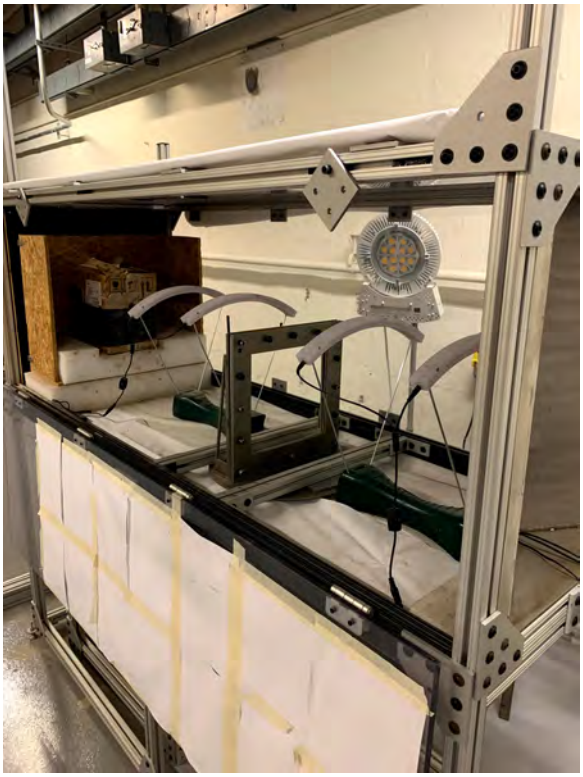

Figure 22: Chronograph Placement in Test Section

Figure 23: Camera Calibration Image Showing the Camera Field of Vision and the Ruler Scaled by Inches Used to Set the ft/pixel Calibration

frames used to determine the velocity. Fig. 24 shows a sample of the ball bearing during analysis. The green ball bearing is the initial difference from the background image, and the purple ball bearing is the change in position seven frames later. The initial velocity calculated was the pixel to pixel analysis. The error for this result was on the order of 1.25% of the measured velocity. Sub-pixel analysis of the correlation image was performed to improve the model's fidelity. This analysis was capable of detecting variations within 1/20th of a pixel. This reduced the error to 0.0625% of the measured velocity. The cross-image code and the sub-pixel analysis are available in

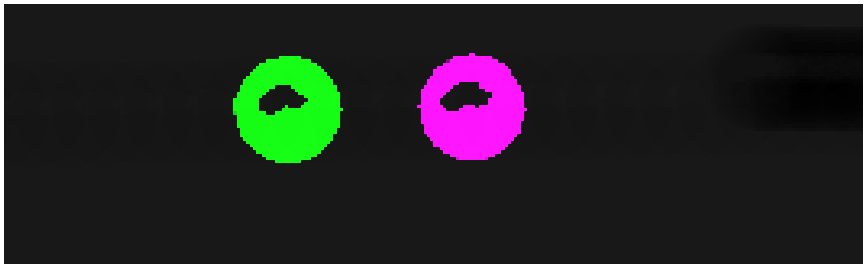

Figure 24: Cross-Image Correlation view of Ball Bearing

Appendices A and B. The camera resolution was 1,008 x 152, which allowed the video to be taken at 39,603 frames per second. The exposure time was 3 microseconds.

3.5.2 Delamination Measurement

Delamination was recorded based on audio and visual tests for materials where V_{50} was calculated. Examples of each impact case were provided for the delamination's radiographic assessment, but this was only accomplished on a select number of plates for each material. Delamination was measured as the total damage diameter for the carbon fiber and glass fiber materials. Measurements were taken with calipers across the maximum diameter on both the front and rear of the plate. Delamination was only measured for the initial impact due to the expected coupling of damage modes between the initial and second shots. Based on observations from the test plates, delamination for the aramid fibers was measured radially from the center of impact. This approach allowed measurements to be taken without extending beyond the maximum capacity of the calipers. When visible delamination was less than audible delamination, the visible delamination was not recorded. The visual assessment of delamination was performed by "naked eye" with no backlighting.

The audio tests for delamination were conducted through a manual tap test. To perform this test, the material was supported on the sides by 80/20 aluminum extrusion, which was secured to the examination table. A box-end wrench was used to tap the test article around the edges of the material to determine a baseline re-

sponse. Once this response was determined, the experimenter tapped the wrench until there was a discernible difference in tone. The material was marked at the location where the tone changed. This process was repeated until the delamination region was determined on both the front and rear of the panel. In general, tap tests in delaminated regions were best described as a musical "flat" note compared to the undamaged regions. If uncertain whether or not a change in tone was due to suspected delamination, the test article was reoriented on the support blocks and retested.

AFRL performed the radiographic assessment. Two methods were employed to characterize the delamination best: computed radiography and pulsed infrared thermography. 17 plates were tested by both methods with varying degrees of success. One limitation of this technique is that there must be a change in density for the results to be seen meaning separation between the material plies is needed to observe damage.

3.6 Nitrogen Gas Gun Calibration

Before conducting experimental tests, a calibration curve was developed for the nitrogen gas gun. The loading process for these tests was the same as those for the ballistic tests. Throughout testing, additional data points were added to the curve fit until at least one V_{50} for each material was complete. The results of these tests and the curve fit are provided in Fig. 25. The curve fit was generally accurate within $\pm 5\%$ for the regions of interest. The maximum recorded velocity from the gun as configured was $1,300 ft/s$. Performance plateaued beyond $500 psi$ at $1,000 ft/s$. Overall, this performance was satisfactory for the experimental testing.

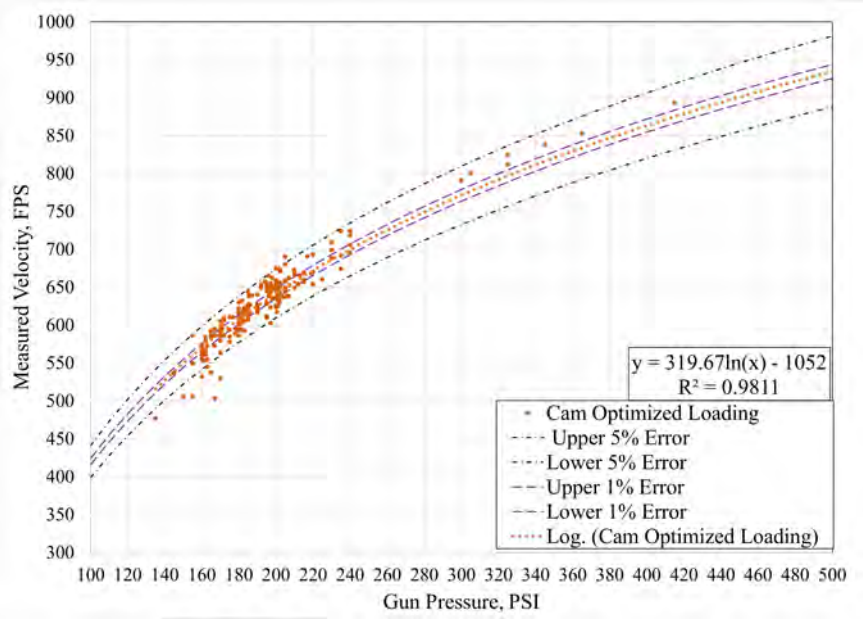

Figure 25: AFIT Gas Gun Velocity Curve, 0.50 **Inch Hardened Steel Ball Bearings,** 12 **Feet Long Barrel**

3.7 Uncertainty Analysis

Uncertainty analysis was primarily focused on the reduction of error in the estimate of V_{50}. As stated previously, the potential error in velocity was $\pm 0.065\%$ of the measured velocity. For each shot, three different post-processed edits of the video were used to build confidence in the results. The edits to the video utilized the Phantom Camera Control software tools to distinguish the projectile from the background image.

To reduce uncertainty in the estimate for V_{50}, several estimates for V_{50} were compared to the results from 3-Pod. For the value of V_{50}, an up-down method V_{50} was calculated. Care was taken when calculating this value to ensure the average of the C_P's was larger than the average of the P_P's. While this method does not inherently provide a confidence interval about the mean, it provides a point of comparison recognized by MIL-STD-662F. As seen in Section 2.3, the logit, probit, and c-log-log generalized linear regression links provide similar results for calculating both μ and

σ. Of these link functions, logit and probit regression models were compared to the results from 3-Pod. These link functions were chosen to highlight the difference between the link functions with a symmetric regression about the point of interest, V_{50}. To assess the goodness of fit, the statistical software program JMP was utilized to calculate the AIC for both models to determine which better fits the data. These values are expected to differ from 3-Pod, but the difference is expected to be insignificant. Confidence intervals about V_{50} were developed from both Wald's Tests and the GLR. The equations detailing application of the GLR are Eqs. (22) to (25). Eq. (26) presents the Wald's Test formula for calculating the confidence interval.

$$\hat{p} \pm z\sqrt{\frac{\hat{p}(1-\hat{p})}{n}} \tag{26}$$

The value of $\hat{p}$ is the parameter of interest, μ and n is the sample size. The z statistic is calculated based on the desired confidence level. For this testing, a 95% confidence was utilized. Both methods are expected to perform well due to the parameter of interest being centered in the assumed normal distribution.

The data was first fit to a normal distribution to compare each of the means to each other within a material's test matrix. The null hypothesis was that the data were distributed normally. If the null hypothesis was not rejected, the 95% certainty analysis continued with ANOVA testing. ANOVA compares the means as a whole to determine if any of the means are significantly different from each other. Although there is expected to be variation in the means based on shot dependency, the null hypothesis was that no statistically significant variation existed, and the means were statistically equivalent. Tukey's test was performed to determine whether the means were significantly different from each other individually. Eq. (27) shows the test statistic for Tukey's test, and Eq. (28) provides a confidence interval about the test

response[52].

$$T_\alpha = \frac{q_\alpha(a,f)}{\sqrt{2}}\sqrt{MSE(\frac{1}{n_i}+\frac{1}{n_j})} \tag{27}$$

$$y_i - y_j - T_\alpha \leq \mu_i - \mu_j \leq y_i - y_j + T_\alpha, i \neq j \tag{28}$$

The value of $q_\alpha(a,f)$ is found through table references or calculated through software such as JMP. The logit and probit analysis data was processed through JMP, and the 3-Pod data was processed directly since the mean, and standard deviation of the 3-Pod results are not equivalent to the mean and standard deviation of the shot history.

3.8 Ensemble Regression Model Estimate of Ballistic Limit

The following model was devised to provide a reasonable estimate of V_{50} from a limited number of design variables. The efforts to generate a model consisted of a test case example of applying a robust ensemble regression model through MATLAB. An extensive data set of experimental test results were required to accomplish this, with the plates all being tested against the same threat. This led to the work of Kumar et al. on ceramic armors[53]. This paper presented 60 different samples with several design variables, all measured without testing. A schematic of the armor plate design and the $12.7mm$ cylindrical projectile was adopted from Kumar et al. to visualize the armor design better. The primary design variables for this investigation were the areal density, ceramic plate thickness, backing material thickness, total plate thickness, and the ratio of ceramic armor to the total thickness of the plate. The design space for these variables is presented in Table 7. Of these design variables, the areal density, ceramic plate thickness ratio, ceramic plate thickness, and backing plate thickness all contributed to a significant response in the V_{BL}[53]. Considering the complexities of composite ballistic events preventing the simple formulation of a closed-form an-

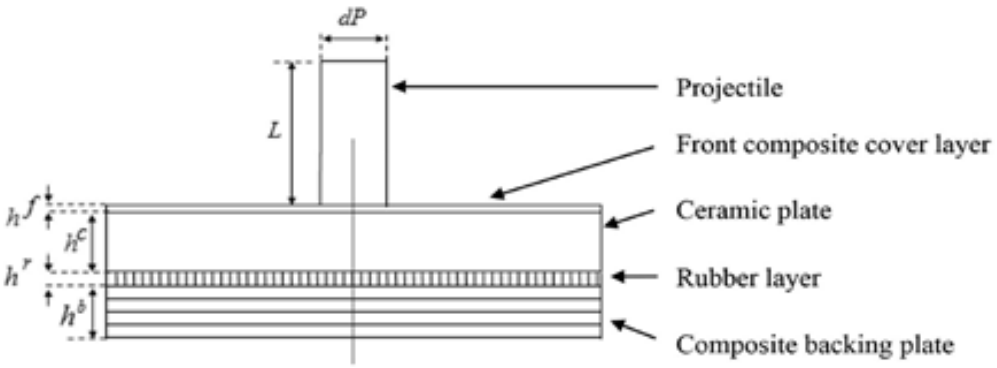

Figure 26: Ceramic Plate Design for Ensemble Regression Model[53]

Table 7: Design Variable for the Ensemble Regression Model

Design Variable	Lower Limit	Upper Limit
Areal Density	$90.3kg/m^3$	$125kg/m^3$
Ceramic Thickness, h^c	$17mm$	$28mm$
Backing Thickness, h^b	$0.71mm$	$25.23mm$
Total Thickness, h	$26.92mm$	$48.23mm$
$\frac{h^c}{h}$	0.3955	0.8734

alytical solution for estimating armor performance, an ensemble regression model is proposed to develop a model with machine learning. To select the data points for the models, at least one test sample from each of the nine test cases of Kumar et al. was selected by evenly splitting the 60 test points into 5 separate groups. This resulted in a training group of 12 data points and a final test group of 48 data points. The data can be visualized in Fig. 27 which plate each test case by total thickness compared with the plate's V_{BL}. By randomly sampling the data, several potential relationships between the design variables were likely to exist that could account for the variations in performance. This methodology only assessed the data as presented without any modifications, such as squaring a design variable or crossing two design variables to create additional relationships.

This initial model employed two different regression ensembles: "LSBoost" and

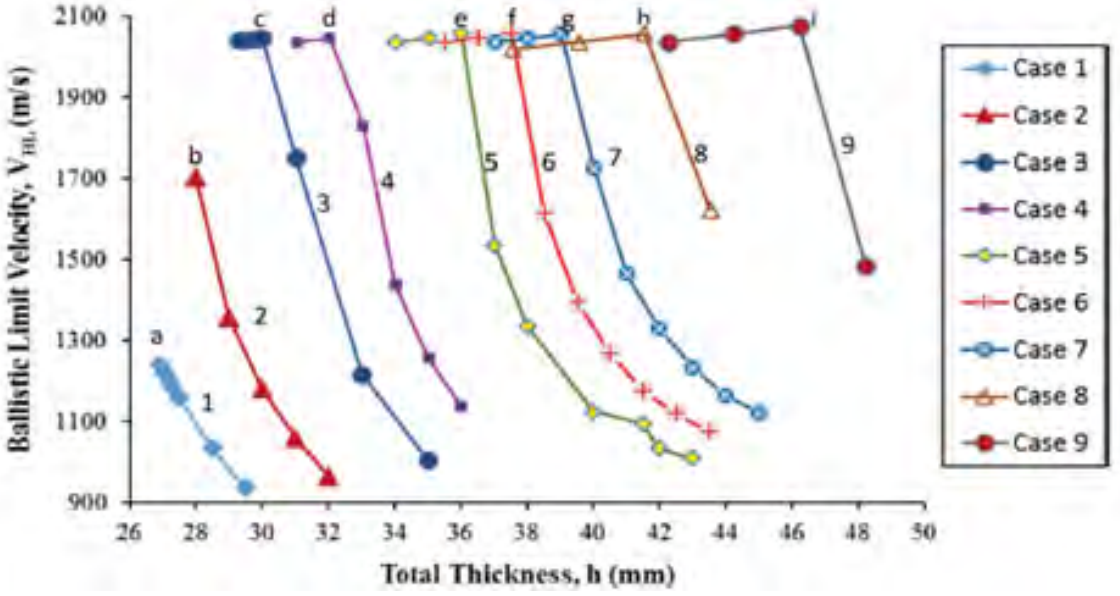

Figure 27: Graphical Representation of the Data from Kumar et al. [53]

"Bagged" algorithms. The "LSBoost" algorithm is a least-squares gradient method. The details behind the algorithm are available within several sources, but sample application and improvements in the model can be viewed in the referenced documents[54, 55]. The former presents an application of decision tree-based regression ensembles while the latter derivations of the "LSBoost" algorithm and potential algorithm improvements. In its simplest form, the "LSBoost" algorithm can be viewed as a steepest descent optimization algorithm for a problem without a cost function or clear linkage between the design variables. As such, it represents a robust algorithm to efficiently learn the response of a system without computationally expensive simulations not readily available to the average designer. "Bagged" algorithms are bootstrap aggregating algorithms that provide data smoothing links between learned decision trees in a regression ensemble[56]. This algorithm is expected to learn the relationships between the random design variables and organize a decision tree based on its ability to link the available data. These methods are highly sensitive to the presented training data, but a wide range of design variables could significantly improve

the model's fidelity.

The models were trained with a single set of data designed to simulate a limited ability to test many feasible solutions experimentally. The trained model was then used to predict the response of all the potential designs. The model and truth data error was determined, and the individual weighting factors for each design variable were recorded. This experiment is thus designed to determine the viability of two common machine learning algorithms to estimate V_{BL} with the computing power of an average laptop computer.

3.9 Summary of Methodology

Through the presentation of this methodology, the necessary procedures to conduct the experiment and analysis the results were presented. Following the introduction of the test facility and the single-stage gas gun definitions for the qualitative analysis of this experiment were presented. This section defined a fair hit with respect to MIL-STD-662F, and other standards were discussed to provide a reasonable design space for multi-shot analysis. Next, the test articles and the test matrix were presented in reference to the previously defined hit definitions. Here the relevant hypotheses for material performance were introduced. Now that the experiment was presented, data acquisition and calibration were addressed to provide the reader with a greater understanding of the investigation constraints. The methodology concluded with the presentation of ensemble regression models used to model a ballistic limit testing data set.

IV. Results and Analysis

The results and analysis were organized such that the experimental results are presented in the first section. This section is divided into three sections detailing clean, medium, and far experimental results. Following this analysis, the delamination results and impacts of each analysis method are presented. The third section presents the findings of the ensemble regression analysis on ceramic armors. Finally, the results and analysis conclude with an overall summary of the results, including applications from the research observations.

4.1 Experimental Testing

Experimental testing is presented in three distinct phases: undamaged ballistic tests, medium separation ballistic tests, and close ballistic tests. Each set of results were organized by material to investigate each material independently. The purpose of this section was to present the data for each configuration and each material such that analysis of these results could be presented in subsequent sections. The general presentation method was material identification, overall test results, and significant findings within the shot group. Findings from shot group to shot group were assessed in Section 4.2.

4.1.1 Undamaged Ballistic Limit Tests

Testing consisted of 3-Pod ballistic tests followed by comparing multiple means to assess the repeatability of the experiment. The undamaged ballistic tests served as the baseline V_{50} values for this analysis. Once a set of statistically identical means were determined, the average V_{50} and the weighted sum squared error for standard deviation were calculated about the mean. This analysis was used to determine a

baseline regression curve for each tested material.

4.1.1.1 Ultra-High-Molecular-Weight-Polyethylene Test Results

Tests for UHMWPE led to the conclusion the nitrogen gas gun was not capable of penetrating the test article. Two test shots were fired at $1,133.3ft/s$ and $1,296.7ft/s$ with both resulting in P_P's. The first shot was taken aimed off-center $3in$ x $3in$ from the edges of the test stand while the second was placed $5in$ x $5in$ from the edge of the plate. Fig. 28 is a time-lapse showing the second impact at $1,296.7ft/s$. This impact resulted in severe plate delamination to the edge of the plate, and the time-lapse shows the progression of the delamination from impact to $5.050ms$ post-impact. The reference line on each image was 1.2 inches from the rear surface of the UHMWPE plate to the maximum extent of back-face deformation. The image shows that the deformation began as a cohesive progression as the plate slowed the projectile. Once the projectile was arrested in the plate, a degree of resilience was exhibited by the composite armor leading the deformation to retreat to a final position less than the maximum deformation. This resulted from several factors, but the most apparent was the high flexural strain to failure percentage. The flexural strain allowed the material to maximize its high Young's Modulus and efficiently transfer energy from the primary yarns throughout the plate.

Further assessment of the damage modes from the UHMWPE plates was con-

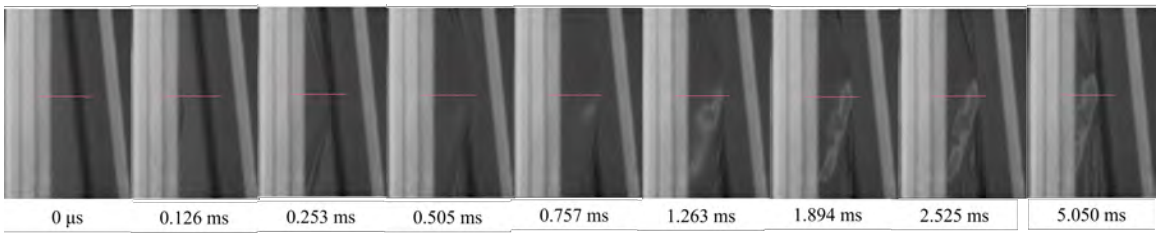

Figure 28: Time-Lapse of 0.25 inch Thick UHMEPE Impacted by a 0.5 inch Hardened Steel Ball Bearing at $1,296.7ft/s$ Showing a Maximum Deformation of 1.2 inches

ducted by assessing the front and rear damage of the plates. Fig. 29 shows both the front and rear of the plates in the test stand immediately following the test shots. Shot 1 was the test shot at $1,133.5 ft/s$ while shot two was $1,296.7 ft/s$. The front plies were depressed and visibly deformed along the primary yarns in both plates. In both the vertical and longitudinal directions, a crack formed in the interior plies. No crack was observed in the rear plies or the front ply, but there was a wrinkle in the material identifying the fault lines in the material. Near the impact, several loose fibers were observed separated from the matrix material. Many of these fibers were broken by the projectile as the plies failed. The length of the second plate along the bottom of the plate was significantly shorter than the top of the plate. This is presented in Fig. 30. The bottom of the panel was 0.5 inches narrower than the top of the plate, with the bottom of the plate retreated inwards towards the point of impact. The damage caused by this failure was inter-laminar shear. This damage mode was not viewed in the first plate, and the damage extent was notably less than that of the second plate.

Analysis of the inter-laminar plies was limited to visual observations, but it was clear that several of the plies had become dissociated from the overall fiber matrix. This delamination effect was confirmed by touching the rear plies and feeling soft spots within the plate. This response was reasonable considering the plastic and elastic deformation viewed in Fig. 28. As the plate dissipated, the impact energy and shock waves traveled through the plate the fibers elongated until failure. Fibers that did not fail were separated from the other plies of the composite material, creating voids where the areal density is considerably less than the undamaged plate. The ultimate effect of this delamination was not assessed in this investigation due to the limited capabilities of the gas gun. Future analysis of this effect on the ultimate strength of the plate could be investigated.

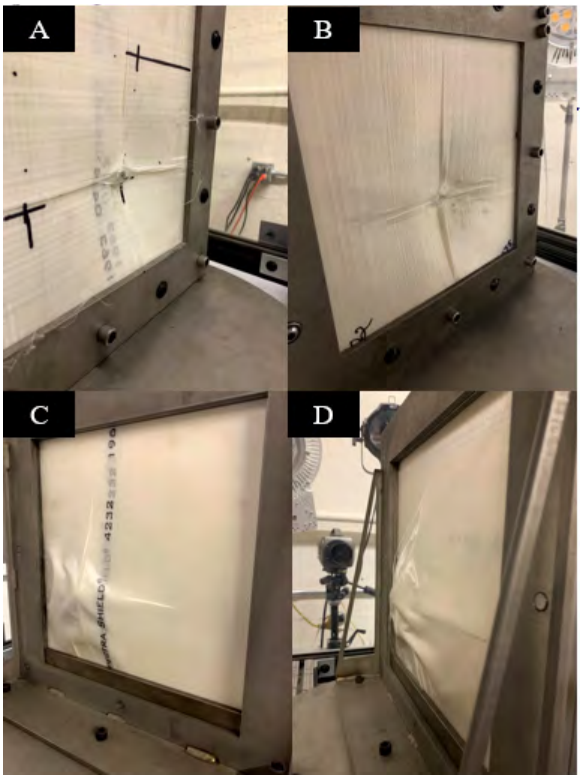

Figure 29: Front and Rear Views of the UHMWPE Plates After Impact: A: Shot 1 Front, B: Shot 2 Front, C: Shot 1 Rear, D: Shot 2 Rear

The rear surfaces of the impacted plates as viewed in sub-figures C and D in Fig. 29 show the extend of back-face delamination. The first shot in sub-figure C has visibly less delamination than the second shot. This is attributed to the two shots' $163.2 ft/s$ velocity difference. In the second plate especially, damage included inter-laminar shear, which extended to the furthest leftmost side of the plate and the rear of the plate. Fig. 31 shows the rear damage on the back plate. The image on the left in Fig. 31 shows the entire back-face of the plate, while the image to the right shows a close-up view of the inter-laminar shear. Several failure modes were observed from the delamination. Following the initial movement of the plate in the direction of projectile motion, vacuum-like force in the opposite direction created the conditions for a significant shear effect as motion from the transverse pressure wave reversed, and the primary stress oscillated between tension and compression. The

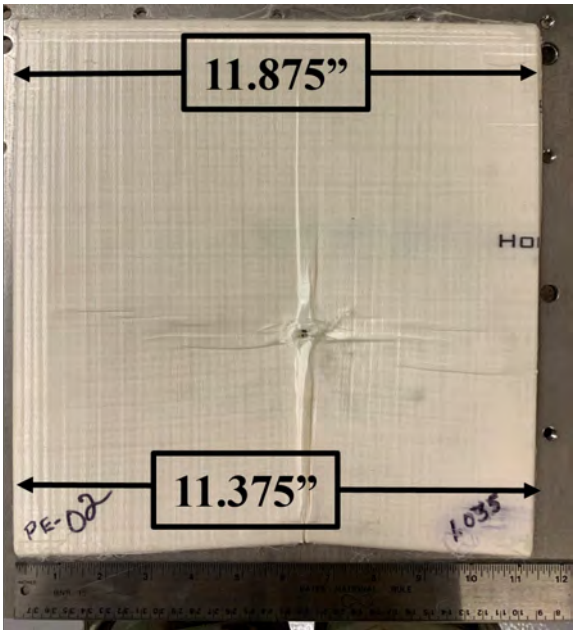

Figure 30: Post-Shot Plate Width of Plate 2 UHMWPE

damage was loosely centered about the projectile, with a greater extent of the damage impacting the vertical primary yarns. The yarns directly over the ball bearings were dislodged from the matrix, but none of the fibers had been broken. The most significant inter-laminar shear was on the bottom of the plate. This confirmed that the original transverse motion broke apart the matrix material, allowing the plies to act independently and extend further than if the matrix material had made the resulting panel more brittle. Ultimately, this response allowed for closer to optimal critical stress for the fibers leading to efficient energy dispersion.

Figure 31: Inter-laminar Shear on Plate 2 of UHMWPE

4.1.1.2 Aramid Fiber Results

Two successful V_{50}'s were calculated from the 21 test plates available for the initial shot for the aramid fiber plates. These tests required 13 and 8 respectively, with both tests yielding statistically equivalent results. Once the equivalence of the tests was determined, both results were averaged to create the baseline V_{50} for the aramid fiber plates. These results can be viewed in Table 8. Overall, the testing led to 10 P_P's and 11 C_P's for the second phase of testing. These shots were potted against velocity to visualize the spread of the data in Fig. 32. The results show the P_P's and C_P's largely covered a similar span $\pm 20 ft/s$ with two shots in more extreme regions of the tested

Table 8: 3-Pod Results for Ballistic Analysis of Undamaged 0.25 inch Thick Kevlar® KM2, 600 Denier, Projectile: 0.5 inch Hardened Steel Ball-Bearing

Test Series	μ, V_{50}, ft/s	σ, ft/s	P_P	C_P	Total Shots
Clean 1	801.981	5.592	7	6	13
Clean 2	800.0	10.93	3	5	8
Total	800.991	7.985	10	11	21

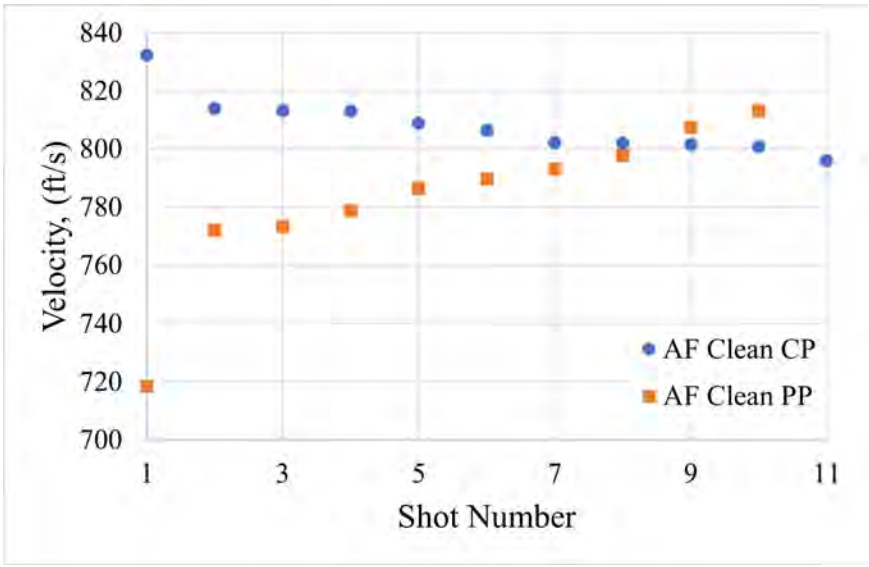

Figure 32: Kevlar® KM2, 600 Denier Clean Shot History

velocities. These results showed several data points were surrounding the estimated V_{50} with a defined ZMR. This allowed for a unique assessment of the data's logit and probit linked regression curves. Two different sets of curves were plotted along with the 95% confidence interval about their estimate for V_{50}. These curves represent the results from the 3-Pod assessment and a generalized view of the data as a whole using a fitted regression model from JMP. The data from JMP was fitted with a GLR confidence interval, while the 3-Pod data simply used a Wald's test. Fig. 33 shows the results of this analysis. First impressions of the data revealed nearly identical curve fits between the logit and probit linked regressions. This was not observed in the 3-Pod results, where the standard deviation led to a relaxed logit fit with greater probability density distributed about the extreme probability values. This is also observed in the skewed error bars for both GLR confidence intervals. Provided the greater velocity spread between P_P's, less confidence in the mean was achieved for the left-hand analysis of the mean compared to the right. The Wald Test makes no distinction between the left and right tails of the data, assuming the response to be normal. This proved reasonable compared to the right-hand confidence bounds

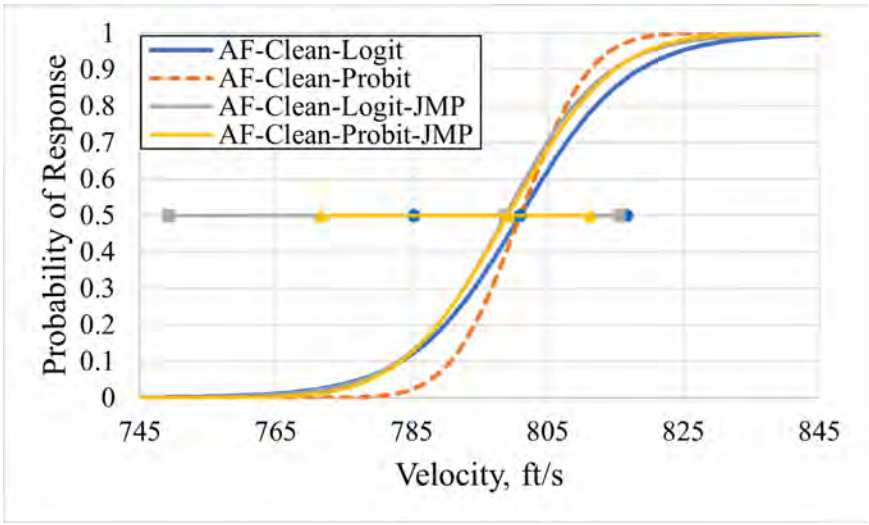

Figure 33: GLM Regression Models for Clean Aramid Fiber Ballistic Limit Tests with 95 % Confidence Intervals

but lacking for the left-hand confidence bounds. The confidence bounds for V_{50}, the estimate of V_{50}, and the standard deviation for each fit are found in Table 9. Based on these results, the confidence interval based upon the GLR method in JMP was more likely to provide certainty of a 95% confidence interval about the mean. This was due to the one-sided analysis of the GLR providing a mechanism to account for limited data about the mean. A final estimate for V_{50} was determined via an up-down method. Results were considered valid when the arithmetic average of an equal number of P_P's and C_P's resulted in the P_P's having a lower average velocity than the C_P's. This was accomplished after five pairs of shots were assessed, leading to a V_{50} estimate of $800.4 ft/s$. The same methodology with eight pairs of data yielded

Table 9: Comparison of Confidence Intervals for V_{50} for Clean Aramid Fiber Tests

Method/Link	**Lower** 95%	V_{50}	**Upper** 95%	**Std Deviation**
3-Pod/Logit	785.3	801.0	816.6	8.0
3-Pod/Probit	785.3	801.0	816.6	8.0
JMP/Logit	749.2	798.8	815.6	7.2
JMP/Probit	771.6	799.2	811.3	12.3

a V_{50} of $798.5 ft/s$. Although there was no uncertainty analysis provided with up-down testing, the results show the up-down methods to be in line with the regression analysis for V_{50}.

4.1.1.3 Carbon Fiber Results

Clean test of the carbon fiber plates yielded eight different V_{50}'s using the 3-Pod methodology. Shots were conducted four to a plate with multiple plates shot in each series to prevent a plate from biasing the data. Of the 85 shots, 42 were P_P's and 43 were C_P's. ANOVA analysis yielded a greater than 95% probability of a significant F-statistic, with the test statistic being 0.1298. Based upon this analysis, Tukey's test was performed to determine significant relationships between the proposed V_{50}'s. This analysis determined that the first and third test series were significantly different with a 95% confidence. The P-Statistic for this relationship was 0.0421, and the critical P-statistic was 0.05. Table 10 presents the means from JMP and the calculated values from 3-Pod. Based upon the wide variability in the results for both V_{50} and σ for the total data-set, it was determined an appropriate course to average the results from 3-Pod to generate on overall clean V_{50} for the carbon fiber plates. This approach was taken due to the only significant difference between the proposed means being the first and third series. Furthermore, the 3-Pod results featured more minor variations than the JMP analysis, further reducing the statistical confidence that there was a difference between the first and third test series. The shot history for the combined test series further validated this approach as none of the shots created significant outliers or random shots far outside the variability for the total ZMR as seen in Fig. 34. This allowed for the creation of two nearly identical regression models from JMP. These models laid between the results from the averaged 3-Pod regression with a region of uncertainty totaling $15.2 ft/s$, providing a high degree of certainty for the

Table 10: Calculated Values of V_{50} for 3k Carbon Fiber from JMP and 3-Pod

Test Series	JMP Results		3-Pod Results	
	V_{50}, ft/s	σ, ft/s	V_{50}, ft/s	σ, ft/s
Clean 1	631.4	11.9	619.3	7.08
Clean 2	603.5	20.0	598.3	15.45
Clean 3	588.9	5.77	589.0	9.79
Clean 4	610.7	4.15	611.8	7.84
Clean 5	603.6	2.94	603.6	4.8
Clean 6	594.2	1.99	594.1	3.34
Clean 7	597.4	7.87	596.0	13.25
Clean 8	601.9	2.63	601.9	4.35

V_{50} of the carbon fiber plates.

Fig. 35 shows this relationship through the regression models. In this case, the GLR confidence interval was very well defined due to the number and quality of the conglomerated shot data. The overall confidence in the findings was quite high. Finally, an up-down method was applied to the data. The first valid response occurred on the 25th pair of C_P's ad P_P's. The V_{50} for this method was $603.6 ft/s$. The large number of pairs required to achieve a valid up-down method result was due to the 3-Pod methodology seeking to cross-over. This creates a minimum of eight shots where there are P_P's at higher velocities than C_P's. The primary takeaway from this result was the significance of maintaining a well-rounded test series. Consider the initial review of this data showed a statistically significant difference between test series clean 1 and clean 3. Despite the differences between these test series, the overall data was well rounded, with several shots between one to two standard deviations from the mean. Several shots are followed with slight separation, increasing the required number of shots needed to achieve a valid response. Had the only method of analysis been averaging as in the three and three stopping criteria, important data may have

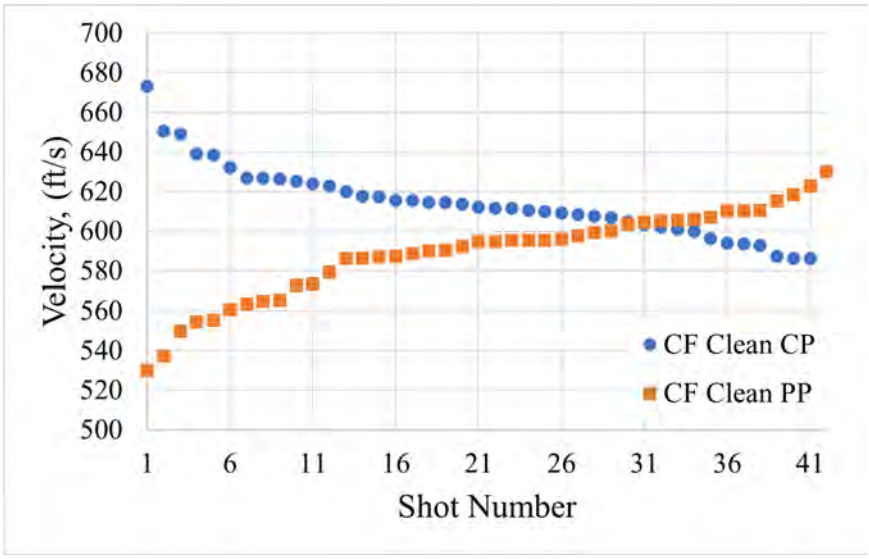

Figure 34: Shot History of all 8 Shot Series Against 0.25 inch Thick 3k Standard Modulus Carbon Fiber, Projectile: 0.5 inch Hardened Steel Ball Bearing

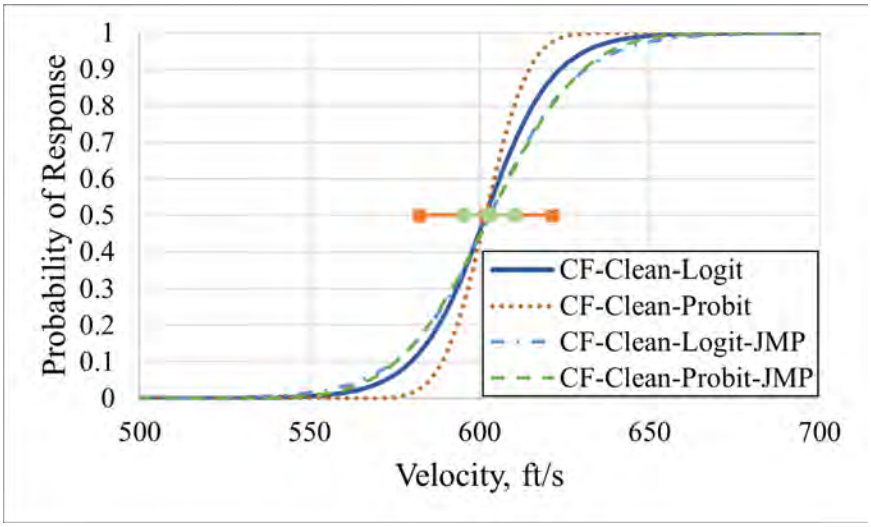

Figure 35: Regression Models for the Conglomerated Clean Carbon Fiber Test Series with a 95% Confidence Interval

been excluded from the overall results. This analysis was also aided by the means being a high and low estimate such that their combined influence matched that of the true mean. Had the means been equal to statistically equivalent to each other but not the rest of the test series, further analysis would have been necessary to determine the source of error between the two unique sets of estimates.

4.1.1.4 Glass Fiber Results

The test for the glass fiber plates was similar to those of the carbon fiber plates previously discussed. In total, six estimates of V_{50} were completed, with 87 total shots fired. Of these, 47 were P_P's and 40 were C_P's. The uneven number of shots was due to several instances where the gas gun could not consistently produce velocities within two to three feet per second. Although this did not assist in creating a ZMR for some test series, the results were minimal average deviation in each shot series, unlike the carbon fiber plates. In much a similar way as the carbon fiber results, glass fiber clean series 1 and clean series 3 were statistically different, but no other relationships presented a statistically significant difference between means. The overall shot history is provided in Fig. 36. Here the impact of having a limited number of C_P's is seen by the limited number of cross-over shots to define the ZMR thoroughly. Fortunately, the remainder of the test shots were very well centered about the estimated value for V_{50}. This reduced the uncertainty in the estimate for V_{50} and provided a well-defined baseline to compare subsequent tests.

The regression models showed the average of the 3-Pod results to be a reasonable estimate for V_{50}, but not as well defined as the intervals from the GLR confidence intervals. Many data points aided the definition of the likelihood regions necessary for a high-fidelity regression model. As with the other regression models presented, the probit link function proved the best fit for the data. This can be viewed in Fig. 37. Despite the increased confidence in V_{50}, the models from JMP exhibited more significant standard deviations than those from the 3-Pod conglomerate. This response separates the standard deviation from the confidence about V_{50}. As established, the standard deviation was more of an identifier of the width of the ZMR. For sample sizes much smaller than the clean V_{50} analysis, care was taken to focus directly on the vicinity surrounding the mean due to the majority of the shots being placed to

reduce error about the mean.

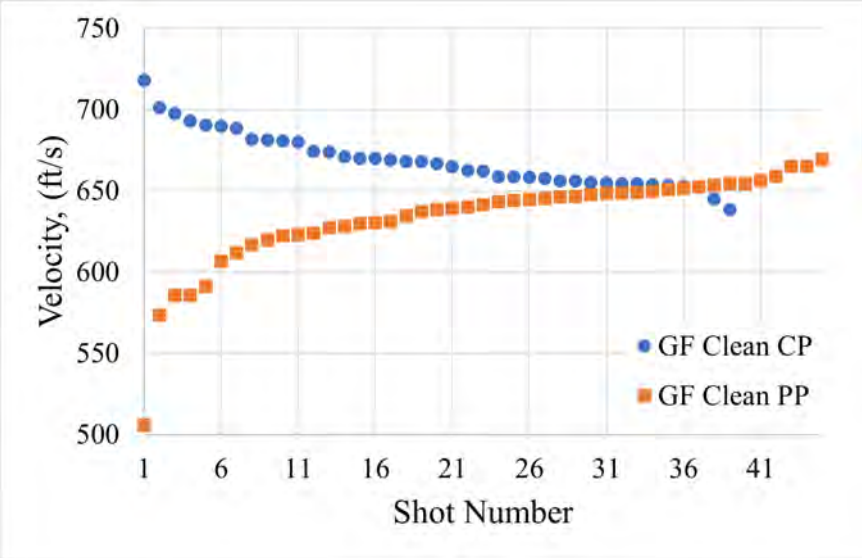

Figure 36: Shot History of all 8 Shot Series Against 0.25 inch Thick 8HS S-Glass Fiber, Projectile: 0.5 inch Hardened Steel Ball Bearing

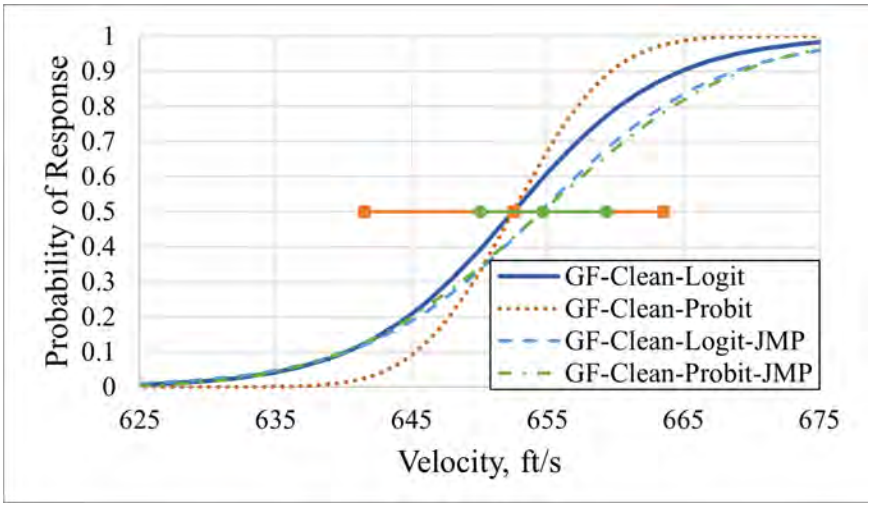

Figure 37: Regression Models for glass Fiber with 95% Confidence Intervals.

4.1.2 Medium Separation Ballistic Limit Tests

Medium ballistic tests were performed with a second shot placed at least two projectile diameters from the damage to fulfill MIL-STD-662F requirements. Addi-

tionally, shots were placed such that the regions of delamination would overlap at a minimum on the rear of the ballistic panel. For aramid plates, shots were placed 2.5 inches from center-to-center of the previous impact. For both the carbon and glass fiber plates, shots were placed to have two projectile diameters between the furthest extent of damage from the initial shot. Tests were separated between initial P_P's and C_P's to isolate the effects of the previous impact.

4.1.2.1 Aramid Fiber Results

After the recording of the initial V_{50} results, the extent of the front-face and back-face delamination was determined via a tap test and visual analysis. A purely Visual assessment of delamination neglected inter-laminar delamination and only measured the delamination in the outermost plies. With this level of analysis, it was possible to place four shots on a single plate in the same grid pattern as the carbon and glass fiber plates. This test series was the aramid fiber 4 shot series presented in this section. The preliminary tests consisted of a two-shot pair and were presented first.

Before testing the aramid medium shot series, the delamination of the 21 test plates was assessed based on the previous penetration. Once sorted, the front two sets of front and rear delaminations were separated the means were compared via ANOVA analysis. There was a 95% confidence the two means were not equivalent for the front delamination. The rear delamination did not have a statistically significant difference between the two means. Table 11 displayed the maximum, minimum, mean, and standard deviation of the maximum front delamination radii. These delamination results match theory for ballistic limit testing considering P_P's must dissipate more energy than C_P's. Based on these results, 2.5 inch center-to-center distance shot-to-shot placement is expected to be placed outside the front plane delamination but within the rear plane delamination. As sample P_P and C_P is shown in Fig. 38. The

Table 11: Kevlar® KM2, 600 Denier Delamination Statistics

Penetration	Side	Minimum Radius, in	Maximum Radius, in	Mean, in	Standard Deviation
Partial	**Front**	1.39	2.522	2.028	0.357
	Rear	3.802	4.854	4.471	0.402
Complete	**Front**	1.126	2.09	1.665	0.310
	Rear	2.87	5.267	3.960	0.834

marks across the plates represent the maximum delamination diameter, while the inner marks show the visible delamination. No additional damage outside of the immediate vicinity of the impact location was observed, suggesting the matrix and the fabric layers were near their undamaged strength.

First, to confirm the shots were placed, 2.5 inches center-to-center post-shot analysis was performed measuring from impact center to impact center. The results of this analysis were compared with an ANOVA test to confirm there was no statistical difference between the shot distance from P_P's and C_P's. Several statistical parameters are provided in Table 12.

With these test elements considered, analysis was performed to determine whether a significant difference existed between the second shot series and the clean series. The tests began with ANOVA analysis yielding no significant difference with a 95% confidence level. This result shows no significant difference between either of the three tests. Regression analysis was still performed, but the only curves displayed were the probit link, function models. This approach was taken to more clearly

Table 12: Kevlar® KM2, 600 Denier Shot-to-Shot Statistics

Penetration	Minimum Distance, in	Maximum Distance, in	Mean, in	Standard Deviation
P_P	2.153	2.633	2.481	0.137
C_P	2.290	2.535	2.431	0.072

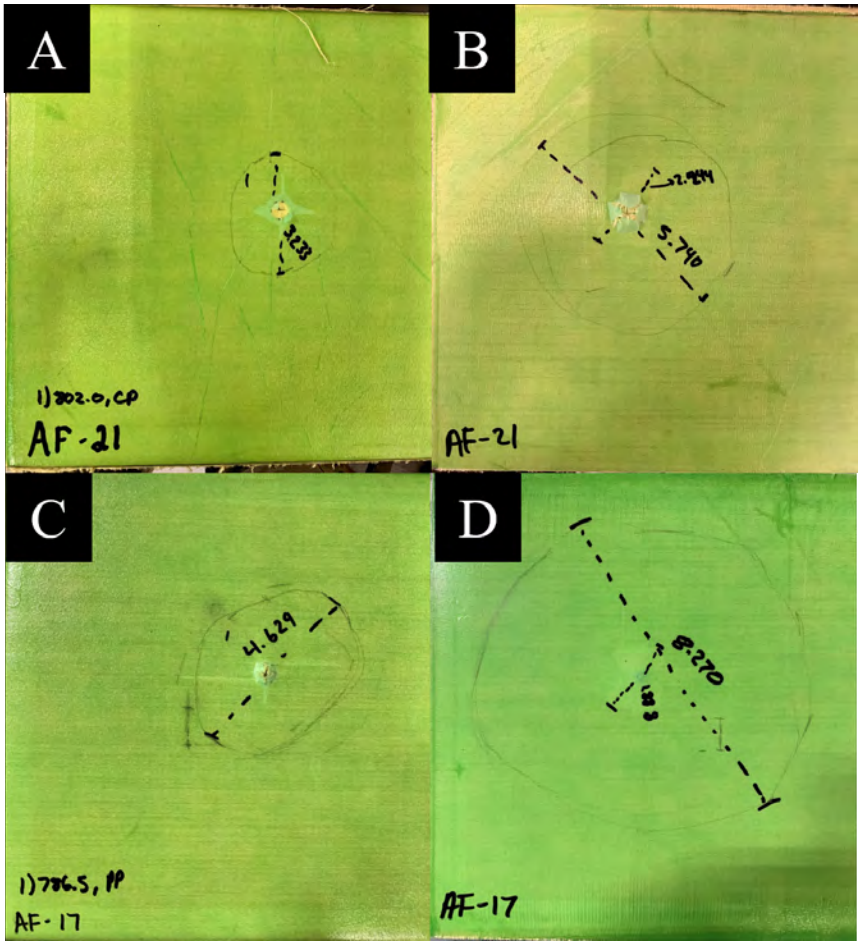

Figure 38: Representative Initial Shots Showing Delamination on Aramid Plates, A: Front, C_P, B: Rear, C_P, C: Front, P_P, D: Rear, P_P

communicate the results and due to the probit model offering a better fit based on the AICc goodness-of-fit statistic. Fig. 39 displays the results showing error bars at a 95% confidence level. Three distinct curves are shown in Fig. 39, the clean regression curve, the C_P series regression, and the P_P series regression. The 3-Pod and JMP regression curves were identical for both of the secondary shot series. Although not statistically significant the C_P series had a V_{50} $9.51 ft/s$ less than the clean V_{50} without a large level of uncertainty about V_{50}. When compared to the original hypothesis, this result was unexpected. Considering delamination extent from a C_P is less extensive than that of a P_P, V_{50} was expected to be as high as, if not higher than, the original

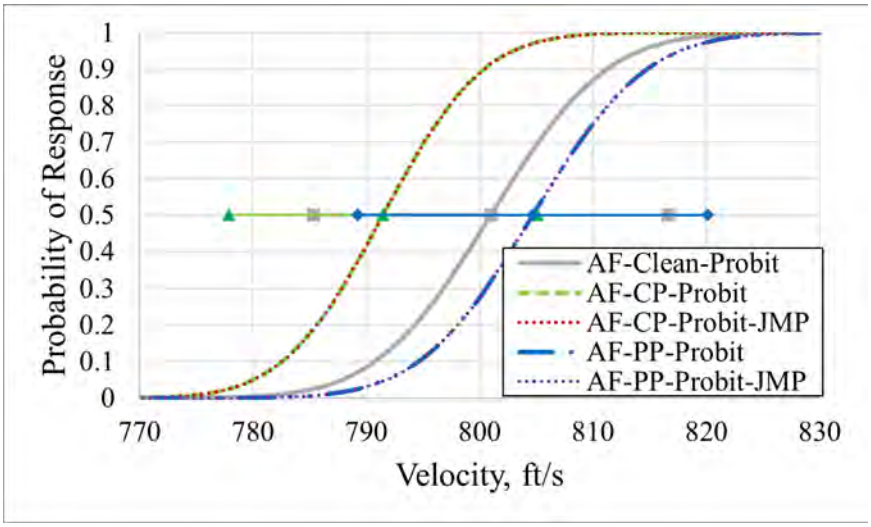

Figure 39: Probit Regression Analysis of Second Shot Ballistic Limits, Aramid Fiber with 95% Confidence Intervals

V_{50} value not less than the original V_{50}. This provided a weak signaler; there may be potential for shot dependency for medium shots against aramid fibers.

To further investigate this result with the available test articles, a 4 shot V_{50} series was performed with the same shot grid as the carbon fiber and glass fiber test articles. Shot placement yielded a similar medium response to the previous test results, but C_P and P_P results were not isolated. A sample plate following the 4 shot grid is shown in Fig. 40.The image on the left showed the front delamination following the shot series. Of note was the significant delamination on the inside of all shots. Unlike the previous shot series, each shot was placed outside the front delamination extent from the previous impact. This effect created an environment similar to the tests of Kinsler and Collins, and the results mirrored the findings: an ultimately insignificant change from the baseline V_{50}. Despite the V_{50} increasing, the increase was only 1.94% of the clean V_{50} and statistically insignificant.

Figure 40: Kevlar® KM2, 600 Denier Plate Following 4 Shot Grid, Left: Front View, Delamination Outline Marked, Right: Rear View, Note Visible Delamination Around the Point of Impact as Well as the Discoloration where the Plate was Clamped.

4.1.2.2 Carbon Fiber Results

The carbon fiber medium shot series yielded four V_{50} estimates, two each for impacts against C_P's and P_P's. No difference between the visual assessment of delamination and the tap test existed for carbon fiber, and delamination was limited to the immediate vicinity of the previous impact. Observations of the plate found matrix cracking on the front Fig. 41 provides a front and rear view of a sample plate exhibiting standard damage modes observed in testing. All shots on this plate were C_P's except for shot number three, where the projectile embedded within the plate. The lighter color markings surrounding the point of impact are the regions of visible matrix cracking. This failure mode contributed the most to marked damage on the front of the plate. On the rear face, the damage was dominated by the petaling of the rear most plies of carbon fiber. Damage occurred along with the primary yarns of the impact and resulted from fibers breaking. The rigidity of the fibers in failure created the impression that the fibers exhibited brittleness when failing with permanent deformation. The end shape of the damage was a diamond centered about the impact point. Statistics describing the observed damage from the initial test against

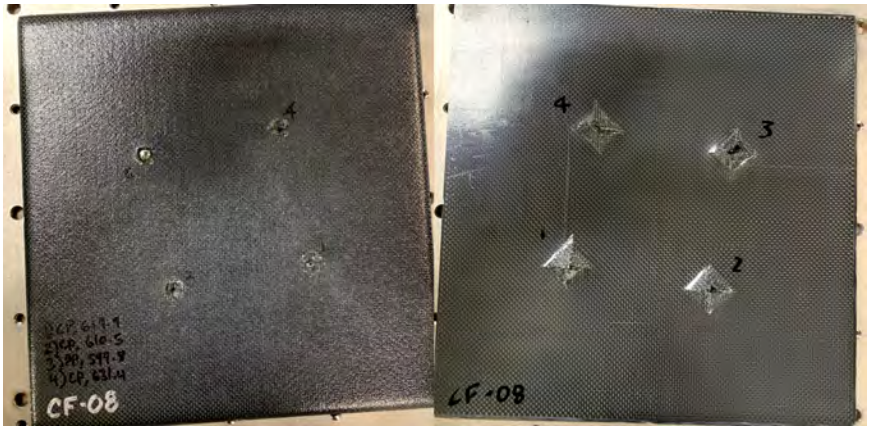

Figure 41: Front and Rear view of a Completed 4 Shot Series Against a Carbon Fiber Test Article.

carbon fiber are presented in Table 13. ANOVA analysis determined no significant difference between the rear face damage based upon the previous impact but found the degree of front face damage to be more significant for previous P_P's. Considering the rear damage diameters were statistically equivalent, this result shows the majority of the shots taken in this analysis were near enough to the V_{50} for the material to require more energy dissipation than C_P's. As seen in the standard deviation, the more significant variation in the P_P's points to a greater response gradient for observed damage from a P_P than a C_P based on velocity.

Table 13: 3K Standard Modulus Carbon Fiber Delamination Statistics

Penetration	Side	Minimum Diameter, in	Maximum Diameter, in	Mean, in	Standard Deviation
Partial	**Front**	0.676	1.054	0.871	0.137
	Rear	0.85	2.163	1.479	0.273
Complete	**Front**	0.52	0.937	0.755	0.098
	Rear	1.315	1.991	1.600	0.164

To avoid undesired bias in the test results the shot-to-shot distance was recorded and assessed. Table 14 shows these results.No statistical difference was observed between the shot distance, and the shot-to-shot distance was confirmed to be greater

than two projectile diameters. As such this test series was considered fair under the definitions of MIL-STD-662F. A representative figure isolating a sample medium shot is provided in Fig. 42.

Table 14: 3K Standard Modulus Carbon Fiber Shot-to-Shot Statistics for Medium Impact

Penetration	Minimum Distance, in	Maximum Distance, in	Mean, in	Standard Deviation
P_P	0.881	1.573	1.281	0.133
C_P	0.634	1.593	1.254	0.212

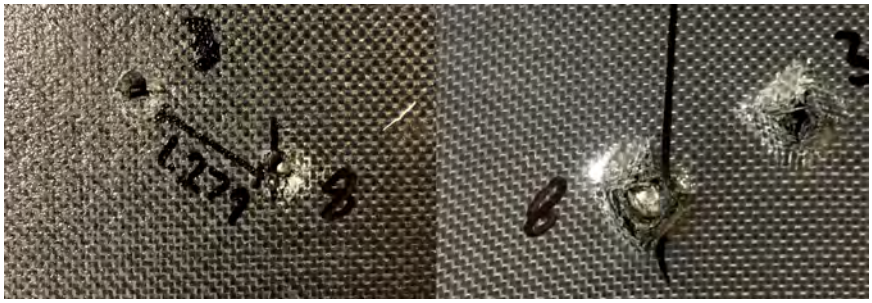

Figure 42: Sample Medium Distance Shot Against Carbon Fiber: Shot 3, C_P, 599.4 ft/s, Shot 8, P_P, 583.6 ft/s, Separation: 1.279 inches Shot-to-Shot

Just as with the clean series, each 3-Pod V_{50} was compared to determine whether they could be treated as statistically similar means. The results of this analysis confirmed there was not enough confidence to reject the null hypothesis that the two sub-groups of V_{50} were equivalent. Although desired, these results were surprising considering the difference in the estimated V_{50}'s for each group. The results are tabulated in Table 15. Despite each test series having $20 ft/s$ differences in the estimates of V_{50}, there was enough uncertainty in the results that the null hypothesis could not be rejected. Two separate ANOVA analyses were performed to interpret the meaning of these results. The first, presented in Fig. 43, compares each mean individually. The second analysis viewed the means based on each objective test series, clean, C_P

medium, and P_P medium in Fig. 44. The green diamonds represent the confidence

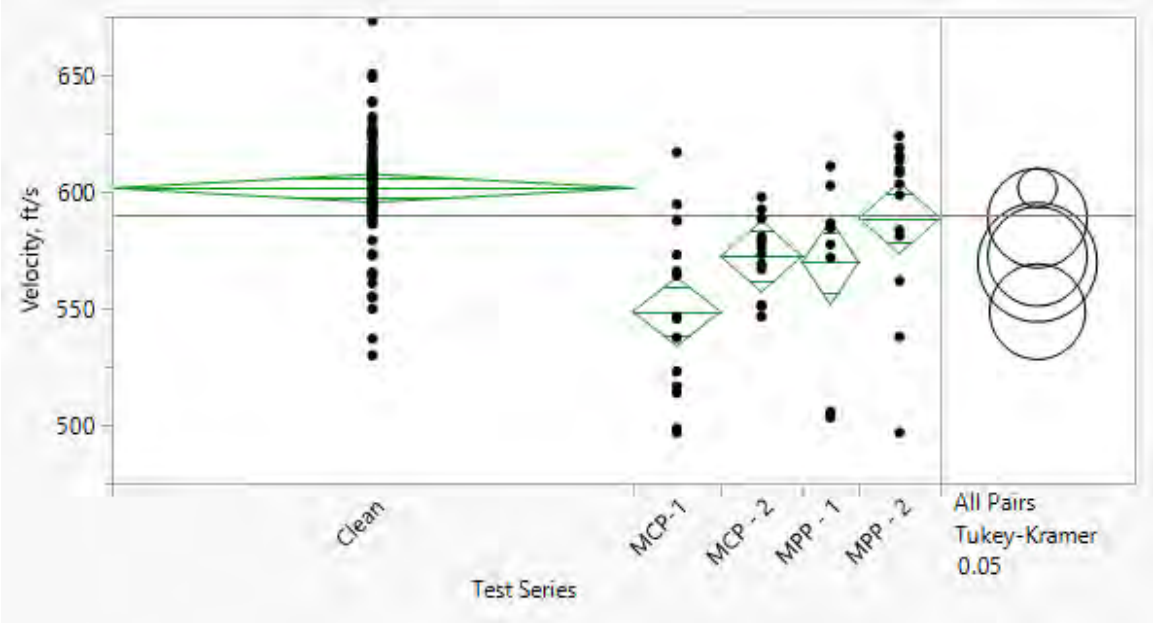

Figure 43: ANOVA Analysis of Carbon Fiber Medium Results, Separated

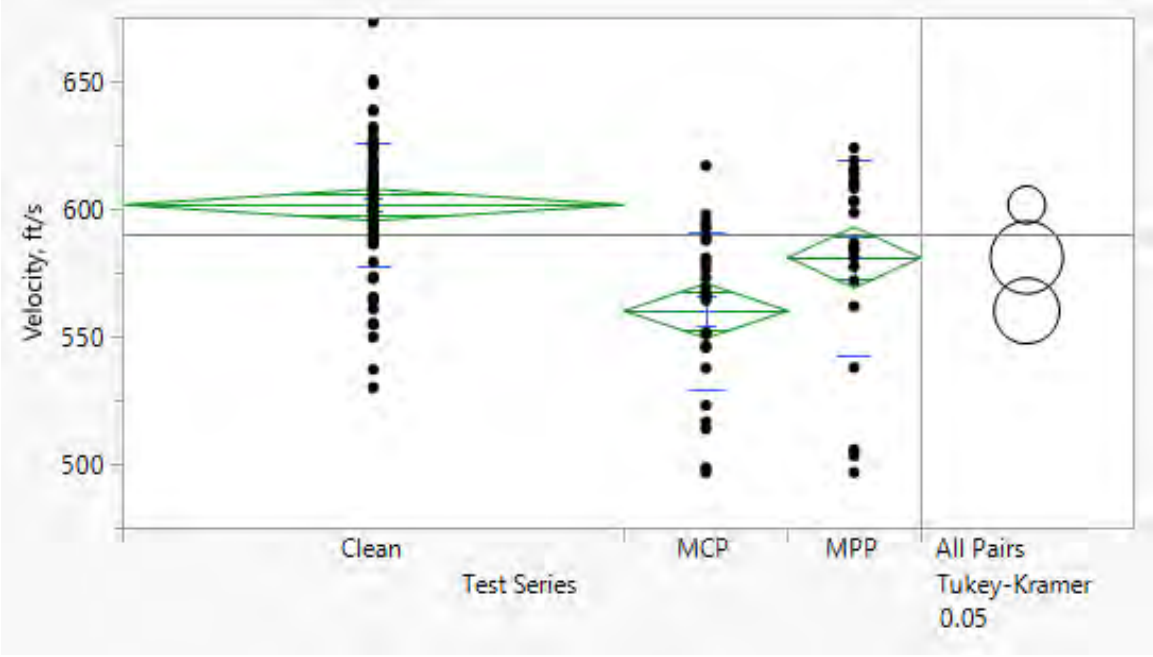

Figure 44: ANOVA Analysis of Carbon Fiber Medium Results, Averaged

region for a 95% ANOVA confidence interval for each of these plots. The black dots are the individual velocity data points, and the horizontal line shows the mean of all

the groups. The ANOVA analysis shows the averaged clean shot series as an independent mean, with the other results isolated as a potential set of statistically similar means. Using Tukey's Test, these means were isolated into three potential groups of similar means. The first set of similar means were the medium P_P series 2 test and the average of the clean tests. The next grouping contained the P_P medium series and C_P medium series 2. The final grouping contained the two C_P medium series and P_P medium series 2. Of these groupings, four pairs of means had significant p-values less than 0.05. These tests and their p-values are presented in Table 16. These results suggest the relationship between V_{50}'s in the carbon fiber medium series to be, C_P $Medium < P_P$ $Medium < Clean$. To expand upon these results, the shot series were condensed into the three test groups shown in Fig. 44. In this representation where the results are averaged for each similar series three distinct V_{50} relationships appear in the order suggested from Fig. 43 and Table 16. The results from Tukey's Test further confirm this assessment and are shown in Table 17.

These results are the opposite of the expected results from Keane for a medium-distanced shot. The response was anticipated to be material-dependent based upon the material's brittleness and its ability to elongate. Considering carbon fiber is sensitive to weakening under impact, a potential extension of these results would be to seek further material properties to characterize the relationships responsible for the variability in shot-to-shot dependency. The material shock characteristics contribute significantly to this response in carbon fiber based on the initial impact energy. Although the P_P was shown to have significantly more visible front damage, the initial shock energies from a C_P would be greater due to the increased velocity. Similarly, the impulse of the event could be assessed for further explanation in future research. Ultimately the results for the medium P_P and C_P shot series produced V_{50} estimates 1.83% and 2.66% different than the clean V_{50} results.

Table 15: Calculated Values of V_{50} for 3k Carbon Fiber from JMP and 3-Pod, Medium Shot Distance

Test Series	JMP Results, (Probit)		3-Pod Results	
	V_{50}, ft/s	σ, ft/s	V_{50}, ft/s	σ, ft/s
Clean Avg	603.0	21.5	601.2	9.986
C_P **Med, 1**	571.6	10.874	571.62	10.87
C_P **Med, 2**	588.4	12.898	599.74	21.56
C_P **Med, Avg**	583.3	15.124	585.7	16.869
P_P **Med, 1**	581.9	46.040	577.7	18.020
P_P **Med, 2**	602.9	9.426	602.9	9.430
P_P **Med, Avg**	592.0	27.112	590.3	13.537

Table 16: Ordered Difference Analysis of Individual Carbon Fiber V_{50} Results, Larger Means are Presented First

V_{50}, **A**	V_{50}, **B**	**P-Value**
Clean, Avg	C_P Med, 1	< 0.0001
Clean, Avg	C_P Med, 2	0.0050
Clean, Avg	P_P Med, 1	0.0119
P_P Med, 2	C_P Med, 1	0.0024

Table 17: Ordered Difference Analysis of Averaged Carbon Fiber V_{50} Results, Larger Means are Presented First

V_{50}, **A**	V_{50}, **B**	**P-Value**
Clean, Avg	C_P Med, Avg	< 0.0001
Clean, Avg	P_P Med, Avg	0.0080
P_P Med, Avg	C_P Med, Avg	0.0297

4.1.2.3 Glass Fiber Results

The glass fiber medium plates were tested with the same methodology as the carbon fiber plates. Unlike the carbon fiber or aramid fiber plates, no damage was observed outside the immediate region of impact. The fiber response on the rear surface was similar to carbon fiber, but the fibers appeared to have snapped rather than cracked. The distinction between these failures provides a qualitative assessment of the glass fiber panel's pliability between carbon fiber and aramid fiber. The same petaling type failure was exhibited in the glass fiber plate as the carbon fiber plate. Fig. 45 provides a close-up example of two medium shots fired against a C_P and a P_P.The upper pair of shots are a C_P initial followed by a P_P, and the lower pair of shots are both P_P's. No visible damage separates the two shots, and no damage was detected in a tap test. The damage statistics are presented in Table 18. No statistically significant differences were observed between the sot type and damage extents, suggesting a slight deviation between a P_P and C_P result.

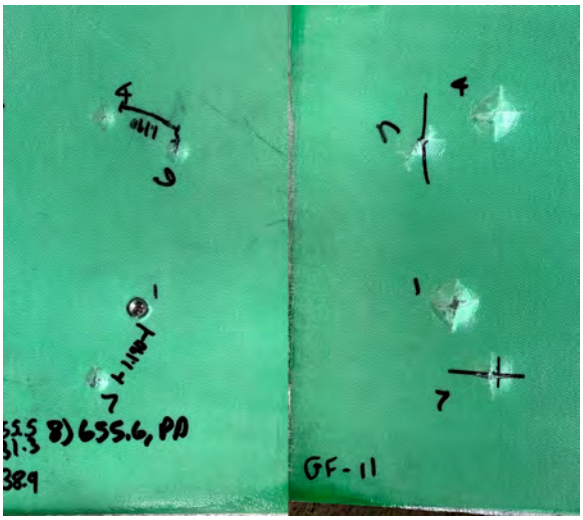

Figure 45: Medium Impacts Against a Glass Fiber Test Article, Left:Panel Front, Right: Panel Rear

Although 4 total V_{50}'s were shot for the medium test series, one set was rejected due to having a statistically significant deviation in the shot-to-shot distance. This

left two medium series, one shot against C_P's and one shot against P_P's, to continue the analysis with a good test series based on MIL-STD-662F. Table 19 provides a comparison of shot to shot distance for the remaining valid test series. ANOVA analysis of the V_{50} estimates revealed no significant variation existed across the estimates. The resulting V_{50} estimates are presented in Table 20.

Table 18: S-glass Fiber Damage Statistics

Penetration	Side	Minimum Diameter, in	Maximum Diameter, in	Mean, in	Standard Deviation
Partial	**Front**	0.52	0.837	0.623	0.101
	Rear	1.051	1.683	1.247	0.147
Complete	**Front**	0.541	0.964	0.663	0.127
	Rear	1.096	2.010	1.280	0.178

Table 19: S-glass Fiber Shot-to-Shot Statistics for Medium Impact

Penetration	Minimum Distance, in	Maximum Distance, in	Mean, in	Standard Deviation
P_P	1.159	1.345	1.252	0.016
C_P	0.856	1.596	1.309	0.153

Table 20: Calculated Values of V_{50} for S-2 Glass Fiber from JMP and 3-Pod, Medium Shot Distance

Test Series	JMP Results, (Probit)		3-Pod Results	
	V_{50}, ft/s	σ, ft/s	V_{50}, ft/s	σ, ft/s
Clean Avg	654.6	11.445	652.5	5.609
C_P **Med, 1**	639.6	2.817	639.6	2.820
C_P **Med, 2**	653.7	7.527	653.7	7.527
C_P **Med, Avg**	646.5	9.700	646.67	5.335
P_P **Med, 1**	648.5	12.75	650.8	14.22
P_P **Med, 2**	650.9	1.719	652.3	3.959
P_P **Med, Avg**	650.9	1.719	651.6	10.058

4.1.3 Close Separation Ballistic Tests

Close separation shots were placed intentionally inside the two projectile diameter specification of MIL-STD-662F. It is within this region where there is uncertainty about how the second series is expected to perform against the material V_{50}. Both carbon fiber and glass plates were shot during this phase of analysis with a total of five V_{50}'s calculated. The shots were placed 1 projectile diameter apart based on the observed front damage with test series separated between P_P's and C_P's

4.1.3.1 Carbon Fiber Results

As with the previous results, analysis began with assessing the similarities between the P_P and C_P sets used to perform the analysis. Unlike the data for the medium tests shots, no significant difference was observed between the front damage for the C_P's or P_P's. Instead, there was a statistically significant difference between the rear damage based on the previous shot result. The results of the statistical analysis are provided in Table 21.Despite the difference in the statistical significance, the trend was the same for both the close and medium carbon fiber series, C_P's exhibited less average front damage than P_P's but more rear face damage than P_P's. This result

shows that the carbon fiber plates were sensitive to the energy state of the projectile throughout the ballistic event. In the case of the P_P's, the initial energy was high enough to create maximum damage, but low enough the fibers did not immediately fail in compression before the tensile damage extended as seen in the P_P's. The energy state of the projectile similarly influenced the rear face damage. In most cases, the damage near V_{50} was similar for both penetrations; however, some P_P did not have the energy to penetrate the final plies of the composite plates resulting in minimal rear face damage.

Table 21: 3K Standard Modulus Carbon Fiber Delamination Statistics, Close Shots

Penetration	Side	Minimum Diameter, in	Maximum Diameter, in	Mean, in	Standard Deviation
Partial	**Front**	0.567	1.151	0.782	0.143
	Rear	0.956	1.81	1.333	0.231
Complete	**Front**	0.536	0.921	0.733	0.131
	Rear	1.256	1.759	1.538	0.158

The shot-to-shot distance was assessed for each test series based upon the C_P and P_P series. No significant difference was found between the shot series. The statistical analysis of these results are shown in Table 22. In Fig. 46 all shots are P_P's except for the shot labeled "1". Both samples showed a crack in the rear plies which extends from one impact to the other. This was expected to weaken the plate and lead to a lower V_{50} when compared with the baseline results. This result is expected to be related to the lack of material elasticity and its overall brittle nature. Fig. 46 both C_P close and P_P close results shows the influence of having both impacts one projectile diameter from each other.

The resulting V_{50}'s proved to be be significantly different based off ANOVA analysis. The significant relationships are provided in Table 23. Consistent with other

Table 22: 3K Standard Modulus Carbon Fiber Shot-to-Shot Statistics for Close Impact

Penetration	Minimum Distance, in	Maximum Distance, in	Mean, in	Standard Deviation
P_P	0.255	0.83	0.513	0.151
C_P	0.230	0.724	0.454	0.166

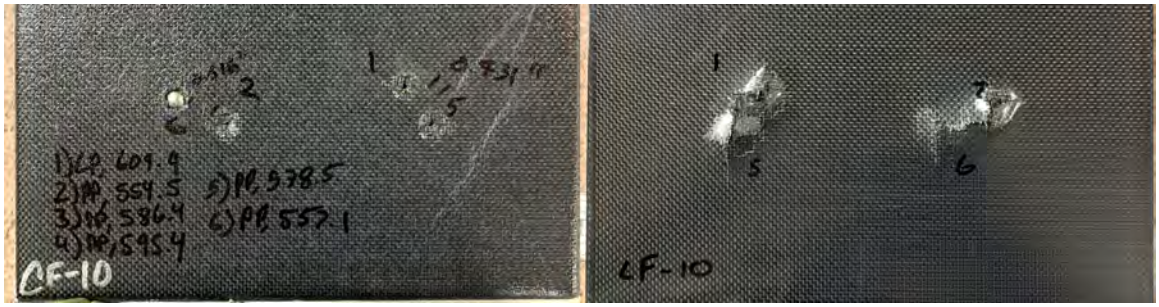

Figure 46: Carbon Close Series Sample Shots, Left: Front, Right: Rear

reported V_{50} values, the probit link function provided the best fit for the test data and was used to extract V_{50} estimates from the carbon fiber close series. The results are tabulated in Table 24. Although there was no statistically significant difference between the C_P and P_P test series, both series were statistically significant from the clean V_{50}. This finding is inconsistent with the results from Keane for close impacts. Keane found a significant decrease in the C_P result but no change in the P_P result despite the P_P V_{50} being larger than the clean configuration. This result is potentially dependent on the test article, but the observed change in performance for this experimental analysis was only 3.15% and 5.65% different from the clean configuration for P_P and C_P results, respectively.

Table 23: Ordered Difference Analysis of Carbon Fiber Close V_{50} Results, Larger Means are Presented First

V_{50}, A	V_{50}, B	P-Value
Clean, Avg	C_P Close, Avg	0.0006
Clean, Avg	P_P Close, Avg	0.0007

Table 24: Calculated Values of V_{50} for 3k Carbon Fiber from JMP and 3-Pod, Close Shot Distance

Test Series	JMP Results, (Probit)		3-Pod Results	
	V_{50}, ft/s	σ, ft/s	V_{50}, ft/s	σ, ft/s
Clean Avg	603.1	21.53	601.8	9.986
C_P **Close, 1**	573.0	19.424	567.8	4.166
C_P **Close, Avg**	573.0	19.424	567.8	4.166
P_P **Close, 1**	571.9	11.444	571.9	11.444
P_P **Close, 2**	592.5	12.308	592.4	12.361
P_P **Close, Avg**	581.4	19.124	582.8	11.953

4.1.3.2 Glass Fiber Results

The glass fiber close series of tests consisted of one V_{50} estimate for both the P_P and C_P cases. Both shot series consisted of twelve shots and utilized the 3-Pod method. Shots were placed one projectile diameter from observed front face damage to test a consistent distance inside of the recommendations of MIL-STD-662F Fig. 47 provides a reference image for the testing with two close shot samples, a medium shot sample, and a single clean shot. The glass fiber close series displayed overlapping damage regions with the carbon fiber plates. The glass fiber damage mechanisms appeared to remain the same between test series as noted by the qualitative similarities between all the test shots on the plate in Fig. 47. The fibers appear to snap under tension rather than cracking or shattering in all cases.

Quantitative comparisons of the front and rear damage for the C_P and P_P revealed no statistically significant difference in the recorded damage. The results of this analysis are provided in Table 25. In a similar manner the resulting shot-to-shot distance between each test series showed no statistical difference. Both series had an average shot-to-shot distance of 0.52 inches. This distance satisfied the desired requirement for close testing, and additional details concerning the shot-to-shot

distance are provided in Table 26.

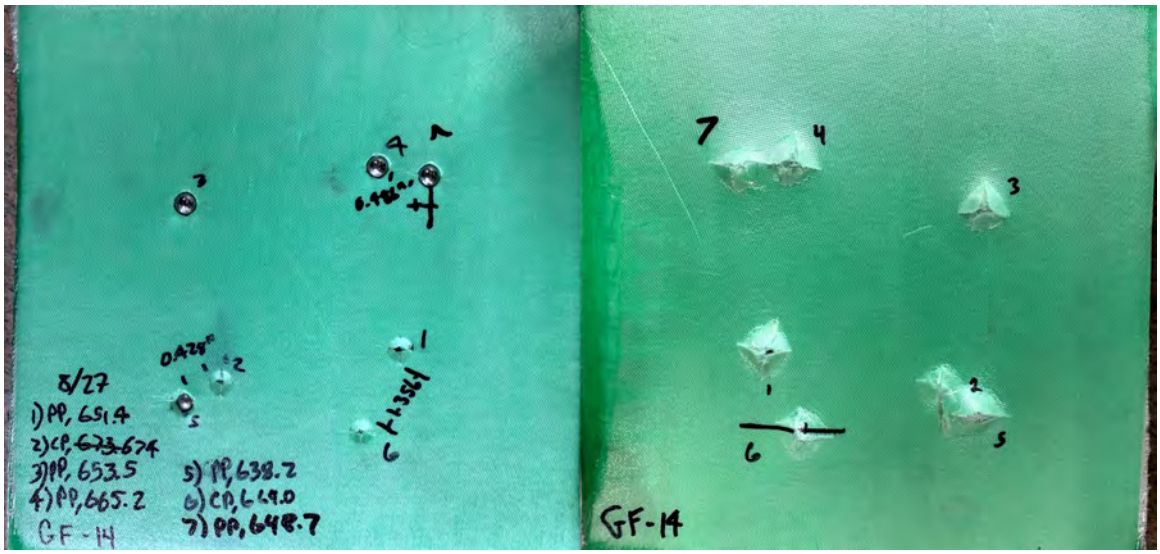

Figure 47: Representative S-Glass Plate with all Test Shot Types

Table 25: S-glass Fiber Delamination Statistics, Close Shots

Penetration	Side	Minimum Diameter, in	Maximum Diameter, in	Mean, in	Standard Deviation
Partial	**Front**	0.485	1.110	0.704	0.190
	Rear	0.583	1.589	1.167	0.261
Complete	**Front**	0.525	1.195	0.671	0.210
	Rear	1.025	1.375	1.166	0.093

As with previous tests for glass fiber no significant deviation from the clean V_{50} was observed. This result was surprising due to the amount of interaction observed between shots and showed the 8HS satin weave S-glass fiber to have very little multi-hit dependency. The resulting V_{50}'s are presented in Table 27. This result is likely due to the high strain-to-failure characteristic of the glass fiber plate tested. This, combined with a large fiber tensile strength, likely created the conditions for the material to behave in a nearly homogeneous material despite being a plied composite material. Further investigation of this result concerning the other materials was conducted in the proceeding section.

Table 26: S-glass Fiber Shot-to-Shot Statistics for Close Impact

Penetration	Minimum Distance, in	Maximum Distance, in	Mean, in	Standard Deviation
P_P	0.232	0.667	0.542	0.122
C_P	0.258	0.684	0.505	0.111

Table 27: Calculated Values of V_{50} for S-glass Fiber from JMP and 3-Pod, Close Shot Distance

Test Series	JMP Results, (Probit)		3-Pod Results	
	V_{50}, ft/s	σ, ft/s	V_{50}, ft/s	σ, ft/s
Clean Avg	654.6	11.445	652.5	5.609
C_P **Close, 1**	648.5	2.669	648.2	0.167
P_P **Close, 1**	655.6	14.538	652.4	3.790

4.2 Overview of Experimental Findings

The structure of this analysis followed a similar pattern to the presented experimental results. First, the delamination effects for each material were discussed comparatively. Following this assessment, initial conclusions were drawn as to the source of composite delamination and its influence on the recorded V_{50}'s. Next, a comparative assessment of several V_{50} methods utilizing the data as collected from 3-Pod was conducted, looking only at the reported V_{50} estimate. Finally, the confidence intervals for the logit, probit, and 3-Pod regressions were presented. Although the probit model offered the best fit for the data when compared to the logit link, the expected confidence interval for the number of shots in an experimental V_{50} was not provided previously.

4.2.1 Delamination Effects

Of the three materials where the experiment was completed, only carbon fiber exhibited shot-to-shot dependency, and the resulting V_{50} decreased from the baseline

V_{50} from the clean results. The visible damage for each material was further investigated to investigate potential reasons for this result. Based upon the similarities between the glass fiber and carbon fiber plates Figs. 48 and 49 present side by side front and rear damage of a sample plate subject to pulsed infrared thermography. Both Figs. 48 and 49 are organized with the thermography plate directly below the observed test plate. The thermography results are collages of four different images of the same plate. Changes in density are denoted by the lighter hue surrounding the impact points. Immediately it was apparent that a density gradient in the carbon fiber plates existed, which was not present in the glass fiber plates. The front damage region on the carbon fiber plates created a halo-like ring about the point of impact. This damage was primarily attributed to the matrix cracking result hypothesized to be a result of the brittleness of the BT250 matrix material compared to the AF163 matrix material used in both the glass fiber and aramid fiber plates. Similarly, this halo effect was seen in Fig. 49 for the rear damage on the carbon fiber plate. In addition to the previous damage, there was also a clear region of suspected delamination about each shot in the carbon fiber plate. For the two close impacts on the left-hand side of the carbon fiber plate in Fig. 49 the delaminated regions are coupled and exhibit a more significant density gradient than the medium shots on the opposite side of the plate. The medium impacts were 1.54 and 1.42 inches apart, with the greater distance being the upper shot. Considering the mean shot-to-shot distance of the medium test series was 1.3 inches, these examples are both far medium shots and represent a best-case scenario to limit observed delamination overlap. Still, damaged regions appear to overlap. The medium shots resulted in overlapped rear delamination to further confirm this assessment. The second shot for both medium results was slow partial penetrations with minimal rear face damage.

The glass fiber plates in Fig. 49 did not exhibit the same delamination results,

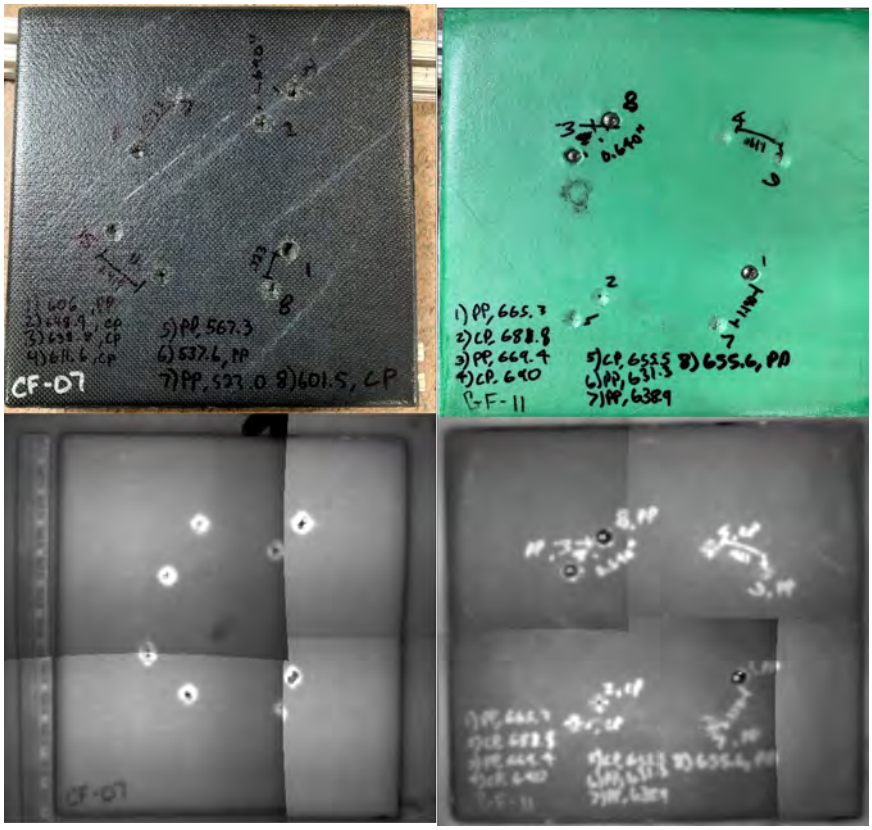

Figure 48: Pulsed Infrared Thermography of Carbon Fiber and Glass Fiber Test Articles, Front

and the only discernible changes in plate density were regions where fiber breakage was observed. This result suggests regions of overlapping damage result in significant depredations in 3K plain weave standard modulus carbon fiber performance. The S-glass 8HS satin weave fiber plate results concluded that no significant region of damage overlap existed. Furthermore, the plate behaved more similarly to a homogeneous material than a plied composite material.

A similar comparison of the aramid fiber results was performed to confirm the classification of the shot were medium on the front face and close in the rear face. Although no statistically significant difference was observed between the aramid V_{50}, results the aramid fiber exhibited overlapping damage regions not seen in the glass fiber plate. Fig. 50 shows the front face damage for a medium shot. The upper

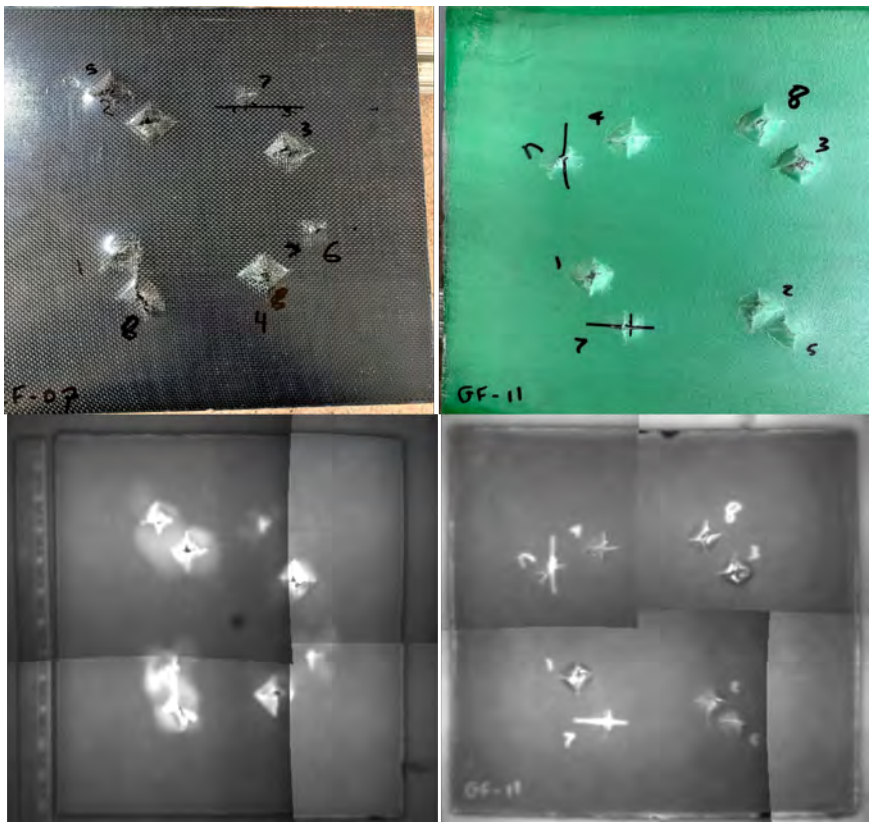

Figure 49: Pulsed Infrared Thermography of Carbon Fiber and Glass Fiber Test Articles, Rear

shot on the plate was a C_P and was the initial shot. The distance between the shots, center-to-center, was 2.3 inches. This was less than the mean shot-to-shot distance of 2.5 inches. Despite the shots being closer than normal, the overlap of the delaminated regions was confirmed, and no overlap signifying a close shot was observed. The rear face delamination results are presented in Fig. 50. Based on the tap test, the circles surrounding the impact region represent the delamination extent. The dark region in the center of each shot's delamination was the visually observed rear face delamination. The circles show the result of the tap test for both results. Considering the rear delamination of P_P's was statistically more significant than C_P's, this test displays evidence that even under the worst-case scenario, the second shot was expected to fall within the delaminated region of the first shot.

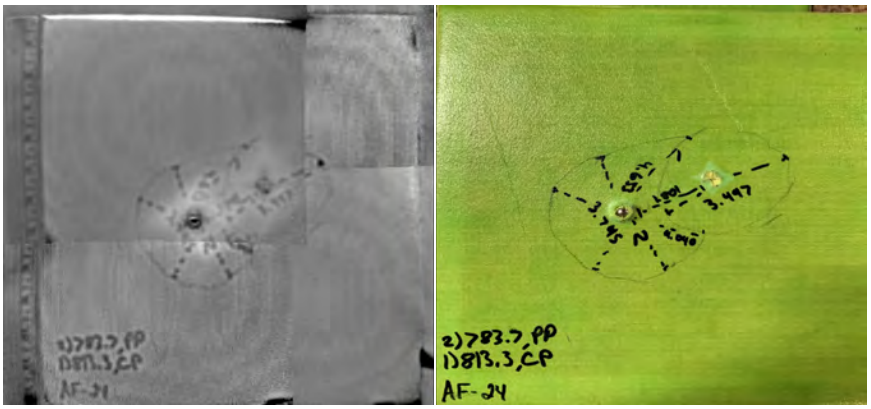

Figure 50: Themographic Image of Aramid Fiber Compared to the Observed Plate, Medium, Front

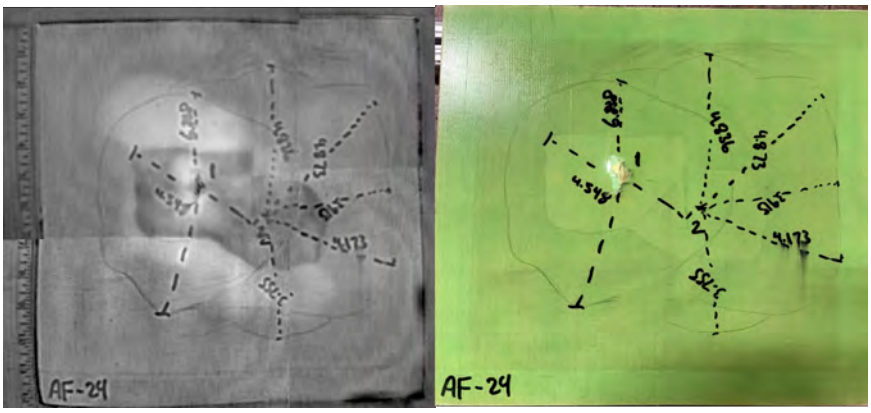

Figure 51: Themographic Image of Aramid Fiber Compared to the Observed Plate, Medium, Rear

Based on these findings, the need to further isolate the driving factor behind delamination is confirmed despite the aramid and glass fiber plates using the same matrix material. Comparing the material properties, the tensile strength, Young's modulus, and strain-to-failure were higher for the glass fiber. Despite this result, the V_{50} for glass fiber and the delamination were both lower than that of the aramid. An additional difference between the materials was the weave. The glass fiber used an 8HS satin weave, while the aramid was a plain weave. The delamination effect may be related to the pliability of the fabric weave, considering the carbon fiber plate was plain-woven and exhibited delamination.

Potential tests to isolate the determining factor include multi-point bending and

tensile tests. These tests would further define the material properties and provide insight into the ductility of the materials. One observation across all plates was that as the material's brittleness decreased, the delamination increased. One additional direction for future investigation is to assess the shock dissipation characteristics for each composite armor. If the tensile shock is severely weakened by the time it reaches the back of the target material, potential rarefaction waves resulting in a rapid transition from tension to compression are prevented, which could keep the plates from exhibiting similar damage modes.

4.2.2 Comparative Analysis of Ballistic Limit Estimates

Although probit and the 3-Pod V_{50} were reported in the experimental results logit and the up-down method were also used to determine the V_{50} estimate. Here all four methods are compared to determine how each method responds to limited sample size. In general, 3-Pod provides the best mean estimate for a given data-set due to the test methodology. 3-Pod utilizes a logistic fit to describe the data once the analysis is complete, but this value may have a weak correlation with the mean of the data-set. Since no data in this investigation failed to refute the null hypothesis, the distribution was normal at a 95% confidence level. A probit or logit GLM fit is appropriate to model the entire data set. As the number of shots increases for a data set, the more likely the means from all methods were equivalent.

The first material assessed in this method was the aramid fiber plates. In this assessment and the remaining up-down methods in this section, Up-Down A is the smallest number of shot pairs needed to have the average C_P value be greater than the average P_P's. Up-Down B is the maximum number of pairs from which a valid result could be recorded. Table 28 displays the result of this analysis for the aramid plates. Overall, the results are very similar for each method, even with limited shots. This

speaks to the overall consistency of the aramid fiber tests. The symmetry of the 3-Pod methodology is displayed based on the up-down methods nearing the same conclusion for each test series. The exception to this was the 4 shot series. The resulting up-down method showed the danger of taking too many samples to compute the mean result in this series. Despite all methods suggesting the V_{50} for this test series was $816 ft/s$, the maximum number of tests to produce a valid up-down method analysis yielded a V_{50} of $807 ft/s$. This is due to the test extending into regions where the estimate for V_{50} was still in the search phase, expanding the spread of velocities used to calculate the V_{50} estimate.

Table 28: Ballistic Limit Estimations for Aramid Fiber

Aramid	Up-Down, A	Up-Down, B	Logit	Probit	3-Pod	Shots
Clean	800.36	-	798.82	799.17	800.99	21
4 Shot	812.33	807.40	816.37	816.55	816.60	10
Med, C_P	791.48	791.66	791.45	791.48	791.48	11
Med, P_P	804.40	805.31	804.41	804.69	804.69	10

Similar analysis was performed for both the carbon fiber and glass fiber test articles. The results are shown in Tables 29 and 30. Unlike the up-down results for the aramid fiber 4 shot analysis, each V_{50} estimate is within $2 ft/s$ of each other. For the clean estimates with over 80 test shots, all estimates were similar except for the 3-Pod estimate. This was due to the 3-Pod results being an average of several independent tests compared to the other methods using the total data-set to generate a solution. The deviations were not significant to the validity of the V_{50} estimate.

Table 29: Ballistic Limit Estimations for Carbon Fiber

Carbon	Up-Down, A	Up-Down, B	Logit	Probit	3-Pod	Shots
Clean	603.63	603.19	603.03	603.08	601.75	85
Med, C_P	592.91	590.90	592.35	592.00	590.28	11
Med, P_P	581.46	583.02	583.01	583.33	585.68	27
Close, C_P	572.73	571.98	572.17	572.99	567.75	12
Close, P_P	579.99	580.61	580.90	581.40	582.17	24

Table 30: Ballistic Limit Estimations for Glass Fiber

Glass	Up-Down, A	Up-Down, B	Logit	Probit	3-Pod	Shots
Clean	654.28	654.72	654.49	654.62	652.48	87
Med, C_P	648.44	649.09	649.09	646.35	646.66	26
Med, P_P	654.88	653.47	650.86	650.90	651.55	21
Close, C_P	648.52	648.78	648.50	648.50	648.20	12
Close, P_P	653.26	-	655.10	655.61	652.40	12

4.2.3 Impacts of Regression Analysis Confidence Intervals

The final assessment of the experimental data addressed the confidence in the results. Inverse prediction from the regression models was performed to accomplish this. The results are a mixture of GLR confidence ratios and Wald confidence ratios. V_{50} is the mean response for the presented data; therefore, the Wald test is expected to present a valid 95% confidence interval despite being limited at more extreme quantiles. If the quantile of interest had been V_{10} or V_{90}, the confidence in the Wald's interval would have been expected to undervalue the confidence interval. The GLR method is preferred based on whether the model has an appropriate level of fidelity to predict the results confidently.

Beginning with the aramid fiber results, the regression curves for all averaged test series were plotted for both the logit and probit link functions. The velocities between the horizontal asymptotes represent the ZMR from the results. Where the curves cross the 50% probability of response is the estimated V_{50} These results are

presented in Fig. 52. No tests for the aramid fibers resulted in statistically significant differences between the estimated V_{50}, but there where three different sets of similar responses: C_P medium, the 4-shot grid, and the remaining tests. To understand why these results were not significant the confidence interval are presented in Table 31.

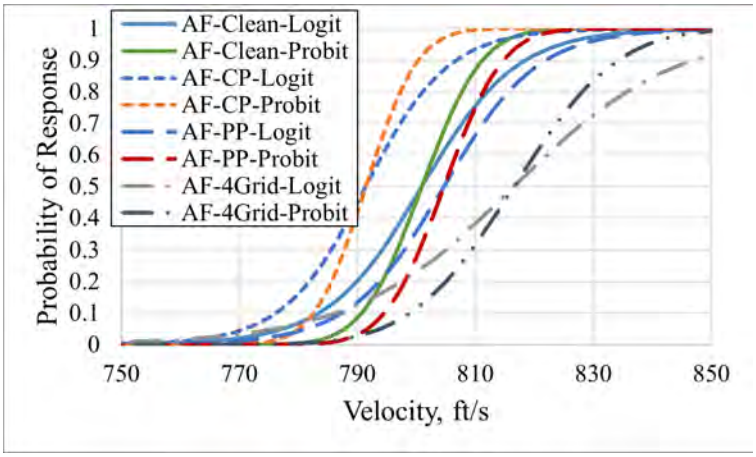

Figure 52: Probit and Logit Generalized Regression Models for all Averaged Aramid Fiber Results

Table 31: Aramid Fiber 95% Confidence Interval about all V_{50} Series, Units are ft/s

Series	Model	Lower 95%	Mean	Upper 95%	Interval
Clean	Logit	765.25	798.64	810.78	45.53
	Probit	774.79	798.97	808.85	34.06
	3-Pod	785.34	800.99	816.64	31.3
Medium, C_P	Logit	784.66	791.45	798.25	13.59
	Probit	785.06	791.48	797.90	12.84
	3-Pod	777.86	791.48	805.10	27.24
Medium, P_P	Logit	796.31	804.41	812.51	16.2
	Probit	796.74	804.69	812.65	15.91
	3-Pod	789.26	804.69	820.12	30.86
4 Shot	Logit	799.02	816.37	833.72	34.7
	Probit	800.43	816.55	832.67	32.24
	3-Pod	789.611	816.60	843.59	53.98

As expected, considering the probit regression had the best overall fit, the probit model had the smallest average confidence interval. The 3-Pod results were larger in all cases except the clean configuration. The logit model generally had a larger confidence interval than the probit model. This result is attributed to the logit model distributing more probability of response to the tails of the distribution. To provide a common comparison across all results the Wald's Statistic confidence interval from the 3-Pod results was utilized to graphically compare the confidence intervals for each test series. Fig. 53 shows the confidence intervals platted against test series. For all results, the confidence intervals overlap, and none of the means are outside the clean series's confidence interval. Although visual depictions of overlapping confidence intervals do not provide a foolproof assessment of the significance of the results, they do provide a visual understanding of the data.

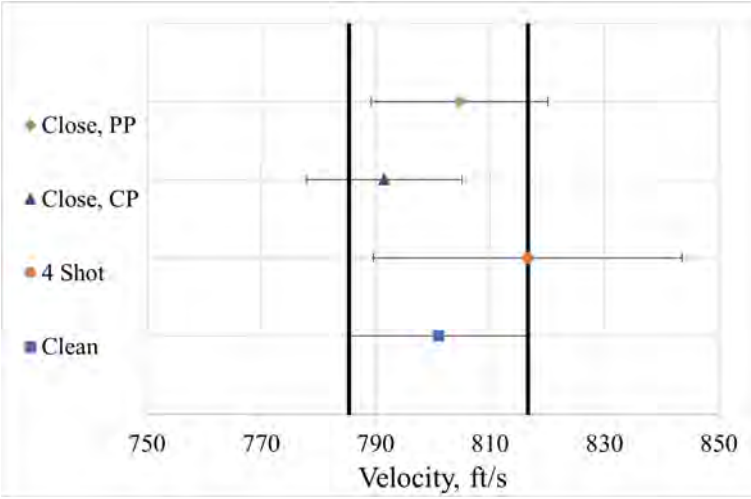

Figure 53: Comparison of 3-Pod Confidence Intervals for Aramid Fiber

Similar analysis was performed for the carbon fiber test articles. For carbon fiber, the close and medium shot series were both significantly different than the clean shot series. The first level of analysis for this material was Table 32 containing the confidence interval results for the regression analysis. The same general trends in the confidence interval were present as in the previous example, but in the case of

medium P_P the GLR estimate for the confidence interval provided extreme values for the lower 95% bound compared to the 3-Pod result.

Table 32: Carbon Fiber 95% Confidence Interval about all V_{50} Series, Units are ft/s

Series	Model	Lower 95%	Mean	Upper 95%	Interval
Clean	Logit	595.16	603.03	610.50	15.34
	Probit	595.33	603.08	610.40	15.07
	3-Pod	582.18	601.75	621.33	19.57
Medium, C_P	Logit	570.20	583.05	618.97	48.77
	Probit	571.40	583.33	611.12	27.79
	3-Pod	552.62	585.68	618.74	66.13
Medium, P_P	Logit	454.31	592.35	639.29	184.98
	Probit	498.75	592.00	631.23	132.49
	3-Pod	563.75	590.28	616.81	53.06
Close, C_P	Logit	556.79	572.17	587.55	30.76
	Probit	557.44	572.99	588.55	31.11
	3-Pod	559.59	567.75	575.92	16.33
Close, P_P	Logit	564.67	580.89	607.65	42.98
	Probit	566.39	581.41	602.82	36.41
	3-Pod	558.74	582.17	605.6	46.86

While it is true this test series exhibited a wide degree of variation in results, the test was not significantly different from the other damaged carbon fiber results. This is clearly seen in Fig. 54. Three significant groupings of regression curves appeared in this plot; the group with the lowest V_{50} was the C_P close series, the middle group with all tests other than the previous test, and the clean results, and the clean test series. Similar to the presentation of the V_{50}'s for each value, there is little difference between the logit and probit response other than the inherent difference in the underlying distribution. The medium P_P test result of concern is in the intermediate grouping showing a significant decrease from the clean V_{50}, but not the same degree of degradation as the worst-case scenario. The reason for the large lower bound was that

the test series lacked the data necessary to increase confidence in the P_P response due to the P_P's outnumbering the C_P's by 13 test points. Based on the unstable probit and logit response, the 3-Pod results were used to compare the V_{50}'s graphically in Fig. 55 Both the C_P and P_P close V_{50}'s were outside of the confidence interval for the clean V_{50} Although the medium results were also statistically different than the mean at a 95% confidence level, both V_{50}'s reside inside the confidence interval for the clean V_{50}. This confirms that the graphical representation of the confidence intervals is valuable to visualize the test results but not a valuable tool for statistical analysis.

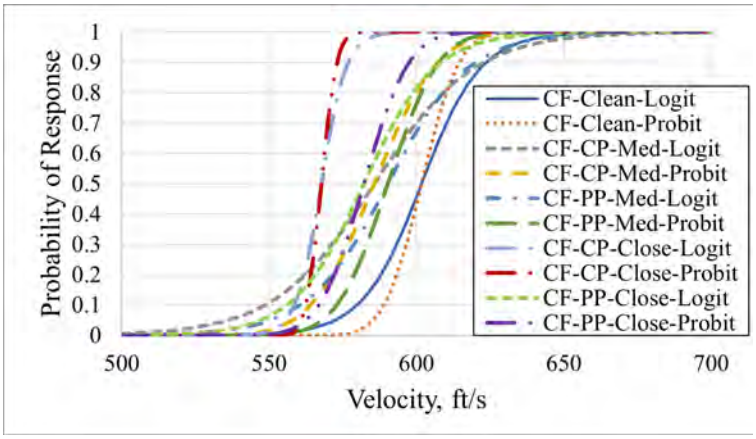

Figure 54: Probit and Logit Generalized Regression Models for all Averaged Carbon Fiber Results

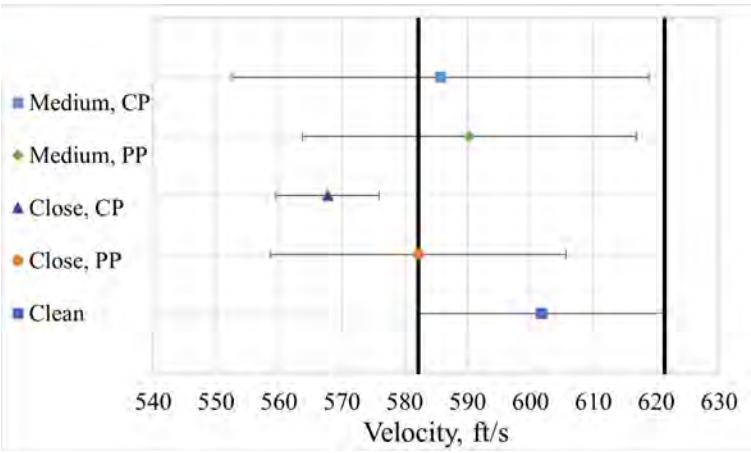

Figure 55: Comparison of 3-Pod Confidence Intervals for Carbon Fiber

The final set of confidence intervals was calculated for the glass fiber test results.

No statistically significant deviation from the clean V_{50} was observed, and Fig. 56 visually confirms this result. All of the regression models were clearly focused about the same narrow range of velocities. The confidence intervals for these tests are presented in Table 33 for completeness.

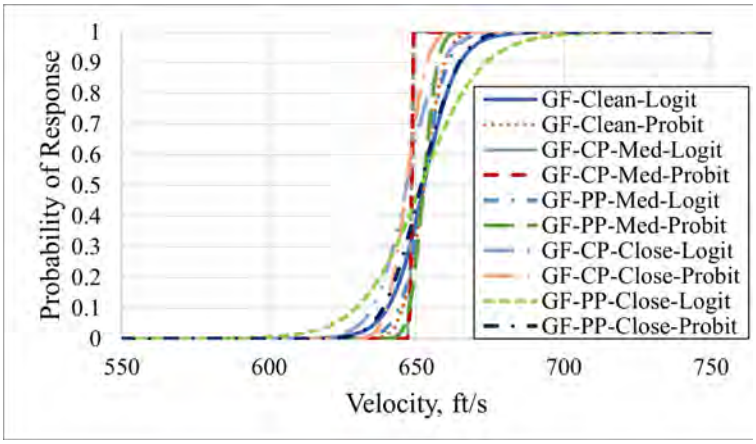

Figure 56: Probit and Logit Generalized Regression Models for all Averaged Glass Fiber Results

For the glass fiber results there was no confidence interval which stood out as being significantly more significant than the other. Each method has a test series where it is the best confidence interval and one where it is the worst confidence interval. This result proves the significance of running multiple levels of analysis on ballistic data to come to a clear conclusion. As with the other materials Fig. 57 depicts a visual representation of the 3-Pod confidence intervals.Notice that all of the results are well within the confidence bounds for the clean V_{50} result providing greater confidence that the glass fiber plate showed no shot dependency throughout the test matrix.

Table 33: Glass Fiber 95% Confidence Interval about all V_{50} Series, Units are ft/s

Series	Model	Lower 95%	Mean	Upper 95%	Interval
Clean	Logit	649.95	654.49	659.27	9.32
	Probit	650.04	654.62	659.32	9.28
	3-Pod	641.49	652.48	663.48	21.99
Medium, C_P	Logit	636.60	646.35	661.89	15.55
	Probit	637.94	646.50	658.95	21.01
	3-Pod	636.20	646.66	657.12	20.91
Medium, P_P	Logit	649.03	650.86	652.69	3.66
	Probit	648.64	650.89	6653.15	4.508
	3-Pod	631.84	651.55	671.26	39.43
Close, C_P	Logit	646.88	648.46	650.04	3.16
	Probit	645.23	648.54	651.85	6.62
	3-Pod	647.87	648.2	648.53	0.65
Close, P_P	Logit	641.85	655.09	668.32	26.47
	Probit	642.72	655.60	668.49	12.89
	3-Pod	644.97	652.4	659.8	14.86

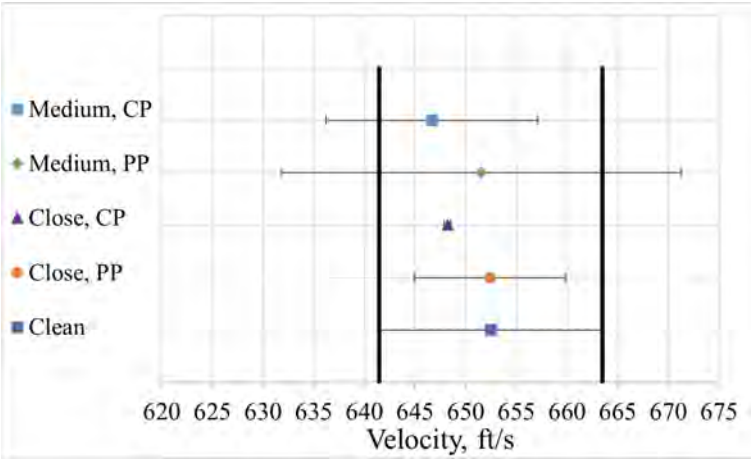

Figure 57: Comparison of 3-Pod Confidence Intervals for Glass Fiber

4.3 Ensemble Regression Analysis

After running the code for each potential model, the first method of assessing the results was to review the importance of each design variable entered in the regression

model to track V_{BL}. Table 34 shows the results of the design variable importance. The first exciting result from the simulation was that both "Bagged" regression models yielded the same variable importance. Based on this result, optimizing the "Bagged" models were not expected to yield significantly different results from the original model. It was surprising that h^b had no impact on the result, but this parameter was utilized in both h and h^c/h. This coupling could have been identified by the regression model meaning h^b was extraneous in the determinant of V_{BL}. This does not mean h^b does not affect V_{BL}. The heavy reliance on areal density to drive V_{BL} led to a less sensitive model more likely to follow the mean V_{BL} for each of the nine areal density cases presented in the data[53] rather than track the extrema. For the "LSBoost" results, the trends were as anticipated. Initially, the model favored h^c to make predictions with little influence from the other variables. Unlike the "Bagged" model, the optimized "LSBoost" model redistributed the influence of each parameter with h^c, areal density, h^b, and h^c/h gaining relevance. Based on this result, the "LSBoost" algorithms were expected to model the results more faithfully than the "Bagged" algorithms. This could change if a different data set were used and is not assumed to be true for all ballistic models.

Table 34: Variable Significance for Ensemble Regression Model

Model	**Ceramic Thickness,** h^c	**Backing Thickness,** h^b	**Total Thickness,** h	$\frac{h^c}{h}$	**Areal Density**
Bagged	1,070.5	0	6,872.8	455.5	41,017
Bagged Opt	1,070.5	0	6,872.8	455.5	41,017
LSBoost	1,476.2	10.6	5.1	17.6	8.0
LSBoost Opt	2,068.9	495.8	113.7	367.7	504.8

The next analysis phase was to track the iteration history on the optimized regression models. Both models used the same optimization scheme to standardize the evaluation process. After 30 iterations, the optimization stopped, and the regres-

sion algorithm accepted the best model. Fig. 58 shows the iteration history for the "Bagged" regression model subject to Bayesian optimization. Bayesian optimization was used for the regression models because it does not require a cost function and was designed to optimize "black-box" systems where the cost function is unknown[57]. Each learning cycle attempted to minimize the objective function. Fig. 59 shows a graphical review of the iterative history. As expected, based on the design variable importance factor, the "Bagged" model struggled to improve its design throughout the optimization sequence beyond the initial results. This was most clearly seen in the relative difference between the minimum observed objective and the estimated minimum objective.

Iter	Eval result	Objective: log(1+loss)	Objective runtime	BestSoFar (observed)	BestSoFar (estim.)	NumLearningCycles	MaxNumSplits
1	Best	11.886	2.7184	11.886	11.886	75	14
2	Accept	11.967	1.0359	11.886	11.893	28	5
3	Accept	11.916	0.80222	11.886	11.89	25	1
4	Accept	12.157	8.0134	11.886	11.886	255	2
5	Accept	12.098	0.6181	11.886	12.005	19	1
6	Accept	12.015	1.8943	11.886	12.006	65	14
7	Accept	11.925	2.0871	11.886	11.995	86	14
8	Accept	12.268	5.1356	11.886	11.886	211	5
9	Accept	12.153	1.9873	11.886	11.886	79	5
10	Accept	12.21	2.072	11.886	12.059	78	12
11	Accept	12.266	6.3177	11.886	12.025	255	2
12	Accept	11.972	14.134	11.886	12.026	500	6
13	Accept	12.028	3.181	11.886	12.025	119	14
14	Accept	12.093	0.30871	11.886	12.029	10	14
15	Accept	12.002	1.1138	11.886	12.021	43	14
16	Accept	12.197	9.1753	11.886	12.023	378	13
17	Accept	11.952	0.37507	11.886	12.018	13	1
18	Accept	12.126	0.94501	11.886	12.041	33	1
19	Accept	12.072	1.4914	11.886	12.042	53	14
20	Accept	12.128	0.62505	11.886	12.058	25	14
Iter	Eval result	Objective: log(1+loss)	Objective runtime	BestSoFar (observed)	BestSoFar (estim.)	NumLearningCycles	MaxNumSplits
21	Accept	12.011	0.40935	11.886	12.055	10	1
22	Accept	12.279	12.549	11.886	12.048	500	1
23	Accept	11.963	0.4673	11.886	12.03	10	4
24	Accept	11.919	2.9953	11.886	12.047	111	1
25	Accept	12.111	2.8445	11.886	12.05	103	14
26	Accept	11.99	0.39845	11.886	12.034	13	1
27	Accept	12.13	0.37531	11.886	12.046	12	1
28	Best	11.87	3.5687	11.87	11.96	133	1
29	Accept	12.129	3.3051	11.87	12.063	122	1
30	Accept	11.961	1.8724	11.87	12.043	72	1

Figure 58: Iterative History of the Optimization of the Bagged Regression Model

Figs. 60 and 61 provide the same analysis for the "LSBoost" model subject to the same Bayesian optimization as the "Bagged" models. When comparing the optimization results, it is clear that the "LSBoost" model has a lower minimum objective and

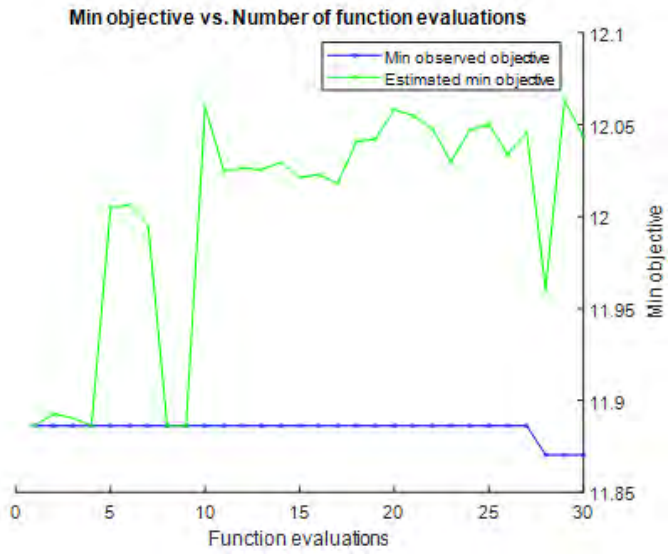

Figure 59: Iteration History of the Bagged Regression Model During Optimization

Iter	Eval result	Objective: log(1+loss)	Objective runtime	BestSoFar (observed)	BestSoFar (estim.)	NumLearningCycles	LearnRate	MaxNumSplits
1	Best	10.266	11.602	10.266	10.266	383	0.51519	2
2	Accept	10.98	0.4637	10.266	10.304	16	0.66503	3
3	Best	10.171	0.91575	10.171	10.203	33	0.2556	13
4	Accept	14.678	0.38975	10.171	10.171	13	0.0053227	3
5	Accept	10.648	0.8248	10.171	10.433	31	0.3402	3
6	Best	10.035	12.069	10.035	10.055	500	0.16136	2
7	Accept	10.711	11.903	10.035	10.342	498	0.22365	2
8	Best	9.8754	7.7115	9.8754	10.136	321	0.118	13
9	Best	9.8259	1.5426	9.8259	9.9369	62	0.082883	10
10	Accept	9.9073	1.0371	9.8259	9.8275	40	0.079324	11
11	Accept	9.8871	11.758	9.8259	9.8857	494	0.083845	1
12	Accept	14.296	6.1998	9.8259	9.8918	259	0.0010001	6
13	Accept	12.521	1.3434	9.8259	9.9123	54	0.021398	11
14	Accept	11.304	1.0944	9.8259	9.8856	43	0.04454	13
15	Accept	11.779	0.40812	9.8259	9.8163	14	0.10863	7
16	Accept	10.596	2.7449	9.8259	10.026	112	0.13551	3
17	Accept	14.793	0.31801	9.8259	10.051	10	0.0010017	3
18	Accept	10.231	12.333	9.8259	10.055	499	0.10792	5
19	Accept	10.108	12.483	9.8259	9.9392	500	0.0065145	2
20	Accept	10.662	12.381	9.8259	10.067	499	0.021482	1
Iter	Eval result	Objective: log(1+loss)	Objective runtime	BestSoFar (observed)	BestSoFar (estim.)	NumLearningCycles	LearnRate	MaxNumSplits
21	Accept	10.864	1.1999	9.8259	10.092	47	0.12932	8
22	Accept	10.156	3.6529	9.8259	10.098	149	0.188	3
23	Accept	10.293	12.038	9.8259	10.116	499	0.053102	10
24	Accept	10.64	2.9125	9.8259	10.113	119	0.99242	11
25	Accept	14.347	1.9372	9.8259	10.124	79	0.0029817	2
26	Accept	9.9185	4.0949	9.8259	10.096	170	0.13805	3
27	Accept	10.334	11.767	9.8259	10.105	497	0.98371	10
28	Accept	9.8984	0.30764	9.8259	10.102	10	0.33628	2
29	Accept	12.824	11.908	9.8259	10.099	500	0.002039	2
30	Accept	10.436	0.30685	9.8259	10.1	10	0.99911	1

Figure 60: Iterative History of the Optimization of the LSBoost Regression Model

was more responsive to the optimization routine in general. This result falls in line with the expectations from the design variable importance in Table 34.

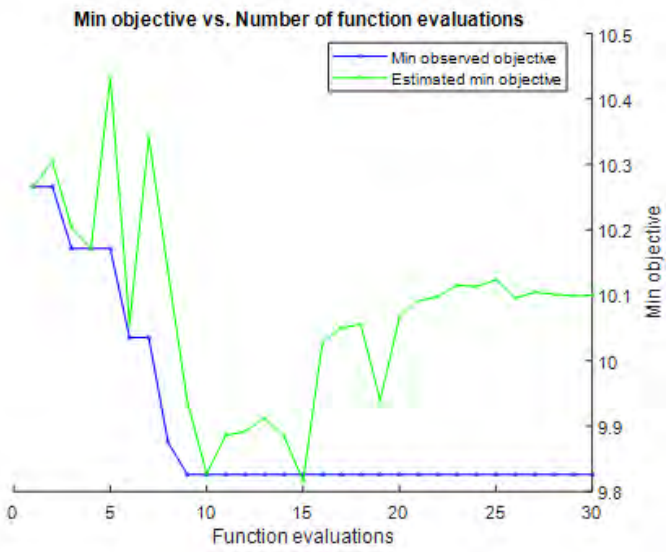

Figure 61: Iteration History of LSBoost Regression Model During Optimization

The next way the models were tested was to plot the respective models against the actual data from Kumar et al. Fig. 62 shows the learned response for each model and the actual data. Initial observations show the drastic changes in V_{BL} from one areal density to the next. Each of the peaks shows the transition from one areal density to the next. The original data was sorted with the thickness of the plate backing increasing within each areal density trial. The result, when plotted, thus gave the appearance of a series of square waves. This followed the same trend as Fig. 27 simply plotted by iteration rather than overall plate thickness. At first glance, the "Bagged" regression models appeared to follow the mean of the entire data set very roughly instead of following the peaks and valleys in the data. As expected, the optimized "Bagged" model varied very little from the non-optimized model. From the variable importance factor in Table 34, it appears areal density is too highly valued in the "Bagged" regression model. When the peaks of the "Bagged" models were compared to the peaks of the actual data, visually, there was some adjustment in the optimized design, but not enough to change the quality of the model greatly. Checking the

minimum objective function from the optimization iterations again confirms these findings by showing very little change in the objective function from iteration 1 to iteration 30.

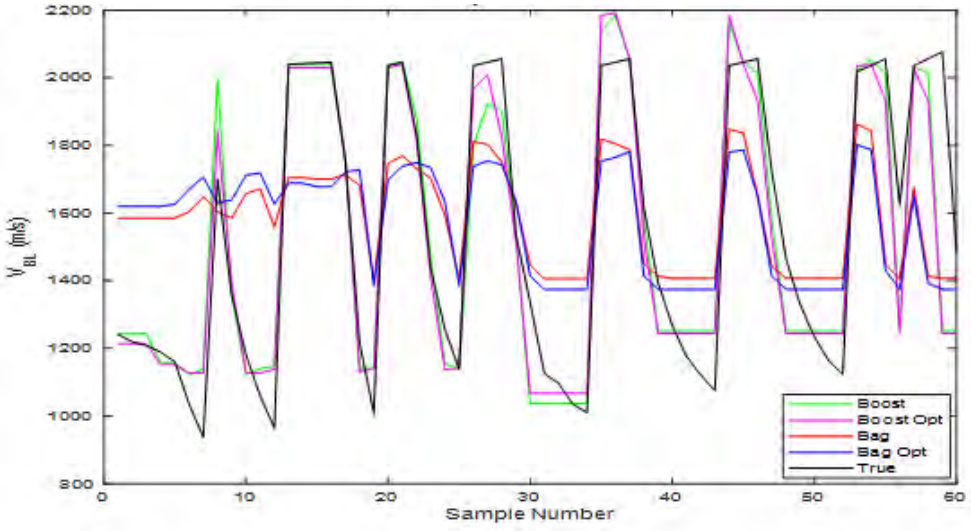

Figure 62: Learned Model Response Absolute Error from Kumar et al. Data

Observations of the "LSBoost" model were much more favorable than the "Bagged" model. Although there were significant error regions within the "LSBoost" models, they tend to track the correct response for all regions except the transitions between areal densities. Looking back at Fig. 61, the optimized "LSBoost" model improved the minimum objective function by a more significant margin than the "Bagged" model. Both regression models ended the optimization routine with estimated errors higher than the minimum observed objective function. This could be indicative of the optimizer struggling to adjust to the data, as sorted, from Kumar et al. Fig. 63 shows the percent error at each sample for the respective regression models. It is interesting to note for both respective optimized routines there appears to be little change from the non-optimized solution. Table 35 reports the extremes of the model error, the average error, the variation in the error, and the standard deviation of the error. The optimized solutions behaved worse than their counterparts for nearly all

the respective categories. The exceptions are the variance and standard deviation of the "LSBoost" optimized regression model. Ultimately, this means the optimization for this model failed to improve upon the results from the original regression models but created a more consistently wrong model with minor overall variation from the correct response. Potential sources of error in the optimization are likely based on the data sort method used to generate the iterations. A potential correction for this would be to sort the data by V_{BL} to remove the abrupt changes within the model. Beyond this, the model was trained with only a single training set providing a small sampling of the design space with very few design parameters. The overall robustness of the fit and the relationships between design variables could be further investigated with crossed properties or squared of the design variables to change the weighting of the developed cost function.

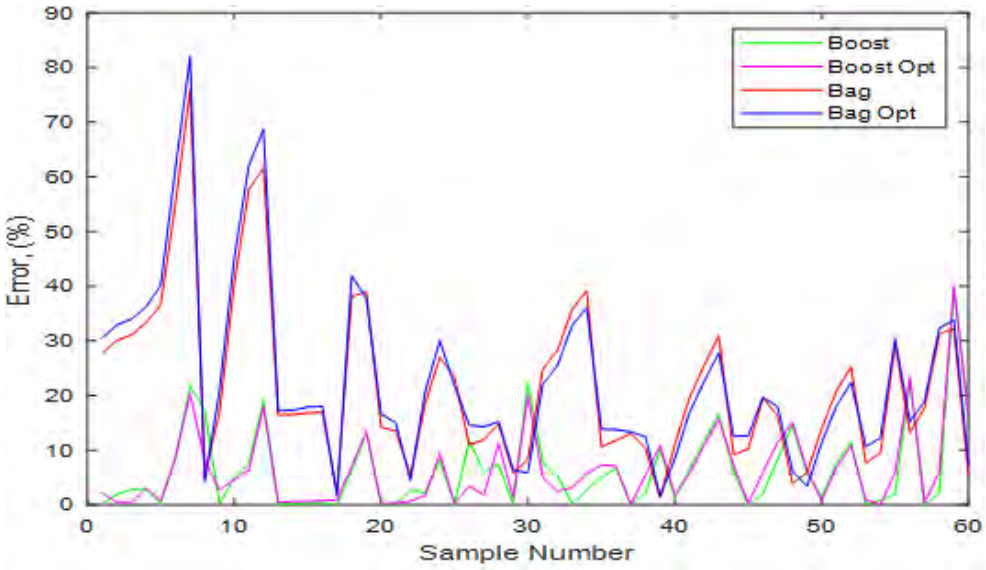

Figure 63: Learned Model Response Percent Error from the Kumar et al. Data

A final method of reviewing the regression models was to apply normal fits to the error terms to determine any potential skewness in the results. Fig. 64 shows a histogram normal distribution fit for each of the models. For both the "LSBoost"

Table 35: Common Statistical Values Comparing the Results of the Ensemble Regression Models

Regression Model	Mean Error	Minimum Error	Maximum Error	Variance	Standard Deviation
Bagged	21.76%	1.3%	76.0%	234.5	15.31
Bagged Opt	22.79%	1.5%	82.0%	269.9	16.42
LSBoost	6.42%	0.005%	39.7%	58.9	7.68
LSBoost Opt	6.49%	0.03%	40.1%	53.7	7.33

methods, an outlier skews the data to the left. This was interpreted as a tendency for the data to underestimate the value for V_{BL}. Another histogram observation was that the probability density was the most contained around zero error for the non-optimized "LSBoost" model. The "Bagged" models both show poor adherence to a normal distribution but do not have the outlier of the "LSBoost" methods. Model assessment using a normal probability plot confirmed the findings of the histogram fits. Fig. 65 confirms the left-hand skewness of the "LSBoost" models and the overall poor results from the "Bagged" methods. The slope of the normal probability plot is indicative of the variability in the model, with the greater the slop, the lesser the variability. The "LSBoost" optimized model distributes the error with greater normality for overestimates and was comparable to the non-optimized model in the underestimates. The other models exhibit a greater error spread and less normality in the error distribution.

In conclusion, the "LSBoost" regression model within MATLAB provided an estimation of V_{BL} for the ceramic armor testing described in Kumar et al. using 15 of 60 data points spanning 9 different areal densities. The model was shown to be limited to predicting V_{BL} at the extrema of the provided data set but had an average error of 6.42% across the sample set. Optimization attempts of 30 iterations of the Bayesian optimization scheme failed to improve the results from the initial

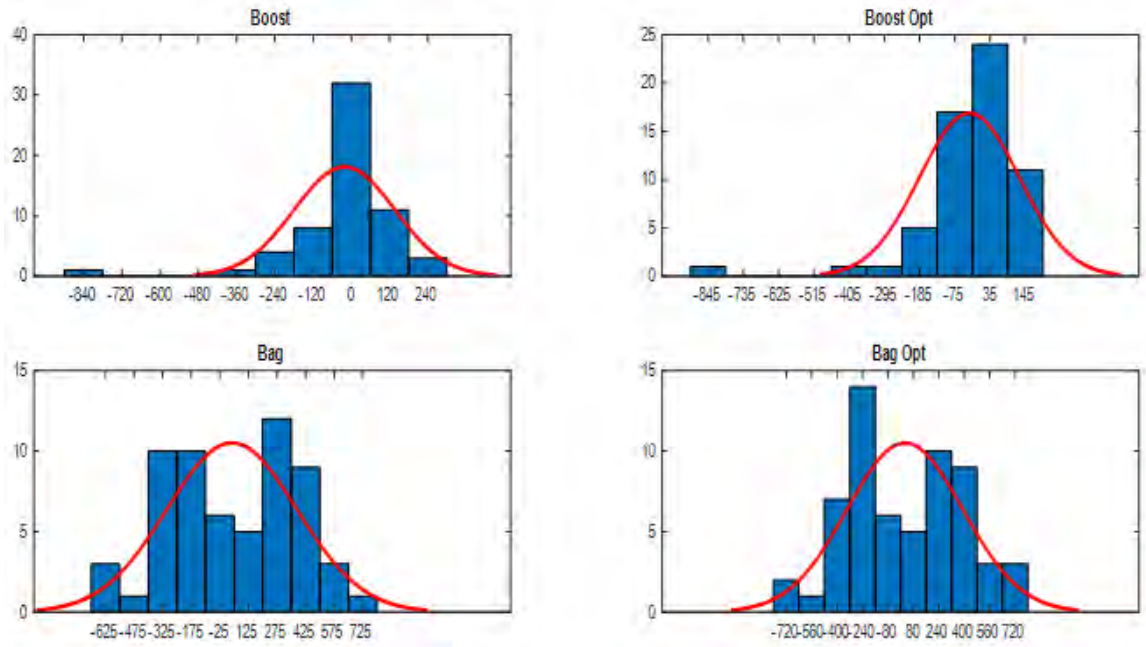

Figure 64: Normal Fit of Error Residuals for Regression Models

optimization scheme. At this point in the investigation, optimization emphasized the ceramic thickness, the backing thickness, and the areal density as critical parameters in determining the V_{BL} of ceramic composite armor. Without applying the optimization routine, the only variable of significance was the thickness of the ceramic plate. Improvements to the model could potentially be made by expanding the learning set and resorting to the provided data such that the data moves from the lowest V_{BL} to the highest V_{BL}. Although the model ultimately is the same as if optimization had not been performed, further testing of the optimization techniques with a more significant number of iterations should lead to more informed decisions for future V_{BL} regression fitting.

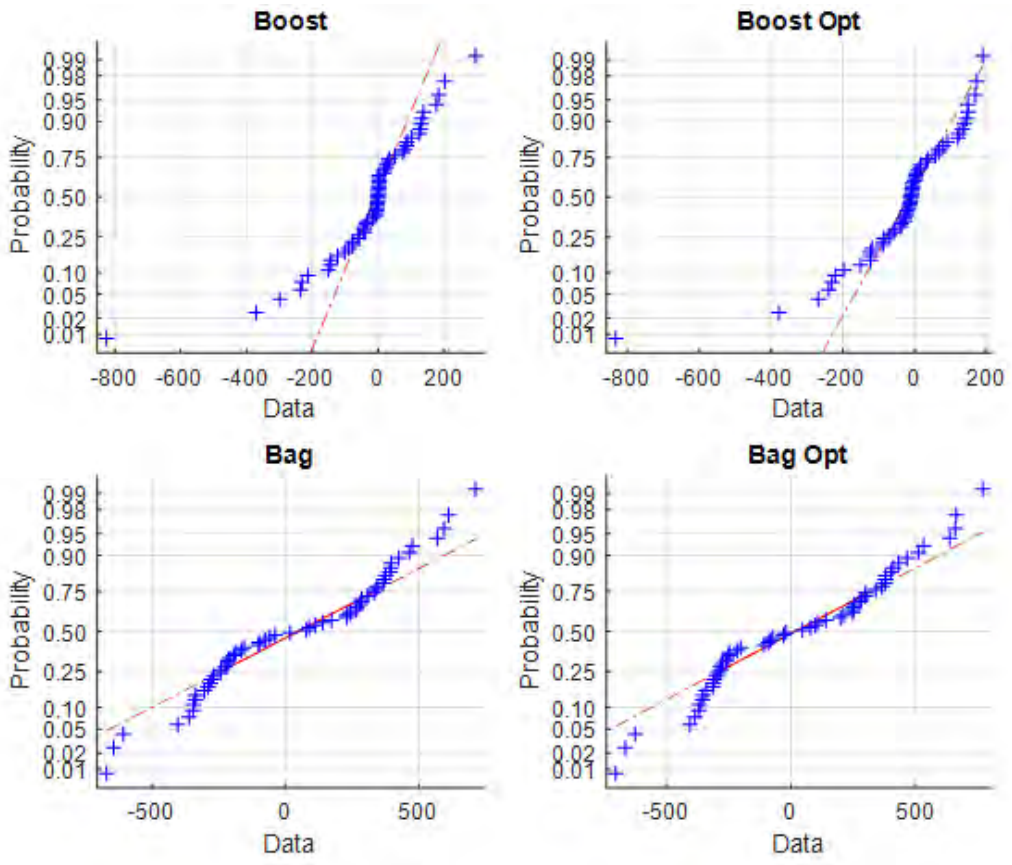

Figure 65: Normal Probability Plots for the Regression Models

4.3.1 Limitations

This model was primarily limited by the lack of consistent material and projectile data. The realm of ballistic testing is highly dependent on the material and the projectiles used in testing. A model such as this is not particularly practical unless it can be applied in a wide variety of applications. Another limitation of this study was that only single factors were assessed. Considering the complex nature of ballistic impacts, it stands to reason there may be better cross relationships to describe how a material responds in the ballistic environment. A potential methodology to determine functional relationships would replace a negligible design variable with a cross of the most influential variables. This would allow the interested researcher to identify design variables with the most significant impact on the overall performance

and identify additional predictors that may not have been expected. Other design limitations were the models themselves. The "Bagged" and "LSBoost" regression ensembles were chosen for their robustness, but refining the model to exploit known relationships could further improve the model's fidelity and increase its applicability beyond this ceramic test set. Refinement could include a new model or weighting existing models to correct specific errors. A significant improvement to the model would be effective optimization. Although an optimization scheme was applied with limited success, further investigation into the optimization scheme and potential modifications is warranted. Perhaps the most straightforward modification to the model would be to increase the number of iterations to confirm that the model has converged to an optimal solution. Once this has been accomplished, adaptive training of the model alternating between several subdivided groups as data would reduce the potential error in the prospective model.

4.3.2 Current Applications

As developed, this exercise is little more than a demonstrator of potential modeling techniques that may better resource application than other forms of modeling. Applicability would be primarily limited to a designer seeking to improve his capability to predict preliminary performance estimates. This reduces the potential development costs of developing armor by preserving resources and reducing the need to test early prototypes experimentally. This capability would also provide an initial tool to refine an existing model or identify regions of interest within the design space. Applied to larger data sets with different materials and threats, this model serves as a base architecture to assess alternate modeling schemes and machine learning within ballistic modeling.

4.3.3 Future Applications

Future applications of machine learning in ballistic testing are promising. As a researcher, the technical nuances and physics of the ballistic event are of the most significant interest. This allows for new technology and innovative research into the phenomena that make certain materials significantly better for ballistic protection than others. Machine learning techniques with a reasonable database of past materials and properties could lead the researcher to profitable relationships not yet exploited. Rather than developing and testing several prototypes, specific applications of machine learning techniques could relate physical material properties to performance as in the sample in this thesis. If non-destructive analysis can lead to insight into the ballistic performance of a material, the research and developmental risks are significantly decreased. The cost associated with development can be reduced, and the human resources necessary to complete a test series also deceases if physical testing is not needed or non-optimal solutions are dismissed before incurring developmental costs. A further extrapolation of this family of models could allow the supplier to provide prospective customers with mission-specific armors without traditional research and development costs.

4.4 Summary of Results

This section aims to synthesize the results of the previous three sections and contextualize the work outside of the academic environment. This study has investigated the ballistic testing of 3K standard modulus carbon fiber, S-glass fiber, 600 denier Kevlar® KM2, and UHMWPE, Confidence in factors affecting ballistic results, and an ensemble regression analysis of ceramic armors. Several test configurations were used to assess multi-hit shot dependency in ballistic testing, and damage modes were assessed. The similarity of the logit and probit links was confirmed, and it was de-

termined that the GLR confidence interval might be limited if the data-set contains less than twenty runs due to a poorly defined likelihood function. For ballistic limit testing at V_{50} the Wald's Test was sufficient to express confidence in experimental results.

4.4.1 Material Performance

Of the materials tested, UHMWPE performed the greatest in terms of V_{50} exceeding the range limitations. This material also had the greatest delamination response and deformed significantly in the limited number of tests. The aramid fiber plate provided the most significant ballistic resistance of the reaming test articles and delaminated significantly. Ultimately, no shot-to-shot dependency was observed despite the damage to the plate. The glass fiber plate did not display any shot-to-shot dependency and behaved similarly to a homogeneous test article with minor damage occurring outside of the immediate region of impact. Although the carbon fiber plate appeared to exhibit similar behaviors as the glass fiber plate, it was ultimately determined that significant damage occurred in the immediate region surrounding the point of impact. This resulted in a statistically significant decrease from the V_{50} estimate of an undamaged plate. This result was different from both Keane and Kinsler and Collins, where increases in V_{50} were observed for multiple hit events.

4.4.2 Factors Influencing Ballistic Limit

Several factors were discussed to explain the observed damage modes in the test articles. Overall, V_{50} appeared to be dependent on the materials' tensile strength, weave, strain to failure, and brittleness. No clear link between these variables and material performance was isolated due to variations between test articles, but the plates with the greatest delamination and V_{50} results had high tensile strength and

strain to failure. These performance characteristics were hypothesized to influence fabric failure modes and allow optimal energy dissipation from ply to ply. The fabric weave was considered significant based on the glass fiber results. Although glass fiber had the greatest tensile strength and strain to failure of the materials tested, it performed similar to carbon fiber and worse than the aramid fiber plates of the same thickness. The carbon and aramid fiber plates were plain weave fabrics, and the glass fiber was 8HS satin weave.

4.4.3 Survivibility Application

Behind the academic structure of this thesis was the underlying connection to survivability analysis. Ballistic testing is most relevant when applied to the design and application of armors or structures likely to be exposed to ballistic impacts. As seen with the regression models from this work, the number of test points available for a designer directly correlates to their ability to create a quality model of the relationships exposed by their analysis. Thus, the more information is available to contextualize complex events such as ballistic impacts, the more likely a significant conclusion was provided. While the 2.66% deviation from the clean V_{50} in the carbon fiber results is minor, applied to a full-scale design, the confidence in this result may force a designer to adjust their margin of safety to ensure the final design meets a required specification. Failed development projects are costly and could be disastrous, dependent on the scale of the project. Advanced regression analysis capable of being computed on a standard desktop was proven to provide a cost-effective tool to estimate the performance of an initial design, given that a requisite amount of relevant data is available to formulate a reasonable model. By creating a model from existing experimental results, a designer gains insight into potentially viable solutions for otherwise costly research and design process. Applied practically, this allows a

company to devote resources for complex numerical solutions and experimental testing for final design iterations without testing several intermediate solutions with the same level of rigor. This allows for rapid development without incurring substantial costs in research and development.

V. Conclusions

Throughout this investigation, a total of 32 V_{50} ballistic limits were obtained using the 3-Pod method. Each test series averaged 12 shots to determine V_{50}. This allowed adequate data to conclude the shot dependency of 3k standard modulus plain weave carbon fiber, 8HS satin weave S-glass fiber, and plain weave Kevlar ® KM2 600 Denier fiber. Utilizing visual inspection and a tap test, the extent of material delamination was determined and generally characterized. Initial conclusions on the material properties influencing delamination were presented. Additionally, an ensemble regression model was developed to provide an alternate means of generating a model for ballistic events. All investigations included confidence intervals presenting the findings robust and meaningfully. The following sections review the objectives of this thesis and suggest future investigations.

5.1 Research Conclusions

Ballistic testing revealed no statistically significant increase in the V_{50} of multi-hit test items. This result was not consistent with that of Kinsler and Collins or Keane. While this result was not as hypothesized, the delamination effects on each of the panels assisted in understanding the results. The material exhibited no delamination for S-glass fiber, had high tensile strength, and had a high strain to failure. This led to the material acting as a homogeneous isotropic material rather than a plied composite material. The carbon fiber plates behaved similarly to the naked eye, but these plates were the only test articles to show a statistically significant decrease in V_{50} for the secondary shots. Regardless of the initial shot's penetration, both the close and medium test series resulted in a $1-2\%$ decrease in ballistic performance. Thermography results determined a region of damage existed around the point of

impact, which weakened the plate. It was proposed that this result was due to the carbon fiber material's brittle nature and a more brittle matrix material than the other composite armors tests. The aramid fiber tests exhibited the greatest degree of delamination, but no significant deviation from the clean V_{50} was observed.

Delamination extent appeared to be directly related to the rigidity of the armors tested. The carbon and glass fiber plates were the least ductile and the densest. These plates exhibited little to no visible delamination and also had significantly lower V_{50}'s compared to the aramid and UHMWPE plates of the same thickness. Based on this finding, delamination is a significant driver in a material's ballistic performance despite analytical methods dismissing delamination as a minor energy dissipating mode. Delamination results followed theory with the front face delamination for P_P's exceeding that of C_P's. The rear face delamination extent was similar for each penetration type on all plates except the aramid fiber, where the P_P exhibited significantly more delamination. These results were as expected from tests occurring near the ballistic limit velocity.

The final investigation of this work showed the potential of ensemble regression models to predict ballistic results within 6.5% of the actual V_{50}. This shows the potential for machine learning algorithms being used by a designer to predict the performance of a family of armors with limited ballistic testing. A mature form of this model could form the backbone of a streamlined research and development process for the armor producer, allowing greater assurance of material performance before testing prototypes or utilizing high-powered computing to run expensive finite element models.

5.2 Applications for Future Work

3-Pod provided a consistent and efficient test algorithm vastly superior to the up-down method presented in MIL-STD-662F. The up-down method is simple but lacks a reasonable means to conduct statistical analysis on the resulting V_{50}. Fitting a generalized linear regression model to the data assists in determining the confidence in the results, but the fit is not optimized about the point of interest unless it is designed into the test algorithm. 3-Pod has also been proven to handle poor guesses rapidly and converge to a solution without wasting a significant number of runs redefining the limits of the test. As such ballistic testing methods such as 3-Pod are recommended for future tests.

Based on the ballistic findings of this work, it is best to avoid overlapping regions of delamination, if possible. Although there was little evidence of a statistically significant deviation from an undamaged plate to a plate with a pair of shots in close proximity, the potential for changes in material performance was still present. Without further testing of plates with significant delamination, such as aramid fibers or UHMWPE, delamination should be viewed as a damage source requiring the experimenter to document its extent and place secondary shots outside the delamination region and such that no overlapping damage occurs. This follows the guidance of STANAG 2920 more closely than MIL-STD-622F suggesting the former's definition of a fair hit is more conservative guidance for hard composite armors. In ceramic armors and the S-glass configuration of this assessment, the MIL-STD-662F guidance was shown to be appropriate. This was due to these materials' isotropic behavior, making their performance similar to that of metals with a margin of safety for potential shot-to-shot interactions. A similar conclusion cannot be drawn for the delamination effects of aramid fibers and UHMWPE.

A final application of this investigation is to continue seeking to exploit modern

improvements in computing power to describe the complexities of ballistic events. This investigation utilized an ensemble regression model with success, but additional models are available to build a model from weak learners gleans relationships not previously realized. This analysis does not remove the need for experimental testing or enhanced numerical methods, but it does provide the potential to develop initial performance estimates from minimal material physical properties. This method is most applicable for a manufacturer seeking to extend current production lines with less need to test intermediate prototypes within a family of materials. Provided the model matures, it could be implemented within an enhanced database to create an optimal armor design.

5.3 Recommendations for Future Work

This research countered the findings of previous introductory work on the shot dependency of composite materials. This investigation is still in its infancy, with several design variables to isolate for future testing. In the experimental realm, tests to characterize the ballistic performance of a family of materials at various areal densities and thicknesses could lead to significant findings for an optimal performance level. There may exist a point in the material design that the law of diminishing returns no longer makes the composite armor light enough or strong enough to withstand the threat environment. Similarly, this investigation tested several fabric weaves, creating an additional variable in performance. It is possible that the fabric weave significantly affects a material's likelihood of a delamination. Additional testing is warranted to characterize this effect on delamination and overall material performance. Another critical design parameter not explored in this experiment was the effect of the geometry ratio on the observed delamination and shot dependency of armors. A test could be proposed examining thick and thin armors to determine how delamination

propagates in different materials with varying thicknesses. In sum, continued testing should isolate design parameters of interest to minimize coupled interactions. This includes standardizing the data processing procedures and establishing additional best practices for all experiment phases.

Another aspect of ballistic testing that could provide insight into material performance is shock loading. Four different materials were tested in this investigation, and all exhibited varying degrees of damage, and each appeared to dissipate energy uniquely. Understanding how the energy is transferred from the projectile to the armor could aid future investigations and develop the next generation of composite armors. Ballistic impacts are unique in the magnitude of the immediate impulse placed on the test article once the event begins. This complicates the relationships between static material properties and performance under such a dynamic loading event. A starting place for this investigation would be to determine the material's shock speed of sound to build a representative model of shock propagation in the test material.

Although ballistic events are dynamic loading events, an investigation into the static material properties of the completed composites could provide a link between the material's delamination response. Testing designed to determine the tensile strength and the ductility of the material would be reasonable starting points to characterize a material's fundamental properties. Based on the relative rigidity of the test articles in this study, bending tests may provide the most significant insight into the ballistic event.

Other non-experimental research should be focused on developing high fidelity finite element models capable of accurately predicting both the ballistic properties of an impact and the extent of delamination. As these codes mature, analysis of shot dependencies can be further investigated. This may lead to enhanced simulations

of the ballistic event and provide researchers tools to develop new materials with dynamic properties to exploit any potential strengthening of the material observed post-impact.

At a minimum, the data from this investigation provides a valuable link to the survivability of composite materials under a wide variety of environments. In civilian and military applications, maintainers must accurately predict the life-cycle of the materials used on their equipment. They must know when to be concerned with damage and prioritize repairs. This is aided by survivability codes which require empirical data to make critical assessments for fielded technologies. Continued exploration of nuances within ballistic testing makes it possible to develop more accurate predictions and ultimately better supply solutions to problems encountered in the field. As greater conclusions can be reached on the peculiarities of composites, these materials can improve the efficiency of countless designs, ultimately leading to better means to improve all aspects of everyday life.

Appendix A. Crossimage Correlation Code

The following code was developed to analyze .avi video files. The code was previous developed by Capt. Michael Keane. The code reads an inputted video file and filters the background image to isolate variations in the video. The user determines at what frame and region of the image to search for variations. Finally, the code assesses the frame to frame variation to determine the velocity of the projectile captured in the frame. This analysis is pixel to pixel.

```
%******   Crossimage Correlation Code as Utilized by 2d Lt
    Hankins **************
close all
clear all

% Resolution 1008X200
File='TS20_CF_159PSI_08272021.avi';
%File = 'Test_Shot_8_136PSI.avi';
vid=VideoReader(File);
n=vid.FrameRate*vid.Duration;
% Set time to 12 seconds for background
%vid.CurrentTime = 13;
ftperpixel = 0.001298591791445 % 08242021 Cal
fps=39603;%frames per second
%fps=46000; %frames per scond 704th testing
scale=[0 2^vid.BitsPerPixel];
zz=5;%how many frames to jump

%% create average matrix for background subtraction
```

```
k=1;
i=1;
while i<=n
    imgavg(:,:,k)=double(readFrame(vid));
    i=i+1;
    k=k+1;
end
imginv=scale(2)-imgavg; %inverse the matrix
backgroundmean=mean(imginv,3); %average background

%%
%subtract average image from all frames

for l=1:n
    imgnew(:,:,l)=imginv(:,:,l)-backgroundmean(:,:);
    imgmax(l)=max(max(imgnew(:,:,l))); %build vector to
       help determine where frag enters frame

end
 %%
 %determine when/where frag enters frame
 framestart=6*5;
 imgnew(:,:,1:framestart-1)=[]; % pay attention here!
 velsample=5; % Number of Places the Velocity is
    Calculated
 b=1;
```

```
for b=1:velsample
[y1,x1] = find(imgnew(:,:,b) == max(max(imgnew(:,:,b))));
y(b)=y1(1);
x(b)=x1(1);
end

%create "area of interest"
%x1=300;
%x2=512;
%x1=320;
%x2=256;
x1 = 260;
x2 = 525;
y1=min(y);
y2=max(y);
if y1 <=0
    y1 = 1;
end

%y2final=round((y1+y2)/2+45);%bottom frame
%y1final=round((y1+y2)/2-45); %top frame

y2final= 135;
y1final= 55;

if y1final <= 0
```

```
    y1final =1;
end
if y2final >= 158
    y2final =155;
end

%%

framesize=[x1, y1final, x2, y2final]; %[top left corner
   coords],[bottom right coords]
%%
%image correlation and then finding peak of the difference
    of the two
%images to find the overall change in position. relate the
    peak location to
%area of inerest to find the change in to calculate x and
   y velocity

for i=1:velsample

    img1=imgnew(framesize(2):framesize(4),framesize(1):
       framesize(3),i); %span given coords
    img2=imgnew(framesize(2):framesize(4),framesize(1):
       framesize(3),i+zz);%span given coords %%this is how
        to jump frames
    figure
```

```
    imshowpair(img1,img2)
   pause(1)
%   close
   correlation=normxcorr2(img1,img2);
    figure
    surf(correlation), shading flat
    pause(1)
   close

[peakcoords,maxvaluepeak]=max(abs(correlation(:)));%find
   coordates of peak

[ypeakcoord,xpeakcoord]=ind2sub(size(correlation),
   maxvaluepeak(1));

output(i,:)=mydftregistration(fft2(img1),fft2(img2),20);

offset2(i,1) = output(i,4);
offset2(i,2) = output(i,3);
offset(i,1)=(framesize(3)-framesize(1))-xpeakcoord; %
   xoffset of peak coords to frame coords
offset(i,2)=(framesize(4)-framesize(2))-ypeakcoord;

end

 %velo city=offset.*((spacing/pixelcal)*(1/(1/11423)));
```

```
velocity=offset.*fps/zz*ftperpixel;%pix*1/sec*ft/px
velocityfft=offset2.*fps/zz*ftperpixel;
if mean(velocity(:,1))<0
    velocity1(:,1)=velocity(find(velocity(:,1)>=mean(
       velocity(:,1)) & velocity(:,1)>0));
    velocity1(:,2)=velocity(find(velocity(:,1)>=100+mean
       (velocity(:,1)) & velocity(:,1)>0),2);
else

  velocity1(:,1)=velocity(find(velocity(:,1)<=100+mean(
     velocity(:,1)) & velocity(:,1)>0));

  velocity1(:,2)=velocity(find(velocity(:,1)<=100+mean(
     velocity(:,1)) & velocity(:,1)>0),2);
end
velocitymag=(velocity1(:,1).^2+velocity1(:,2).^2).^.5;
Velocitymagaverage=mean(velocitymag)
VelocityFFTavg=mean(velocityfft(:,1))
Velocitymagfft=sqrt(velocityfft(:,1).^2+velocityfft(:,2)
   .^2);
error1=(offset+1).*fps/zz*ftperpixel-offset.*fps/zz*
   ftperpixel;
errormag=sqrt(error1(:,1).^2+error1(:,2).^2)
errorfft=(offset2+1/20).*fps/zz*ftperpixel-offset2.*fps/
   zz*ftperpixel;
errormagfft=sqrt(errorfft(:,1).^2+errorfft(:,2).^2)
```

Appendix B. Code for Sub-pixel Analysis

The following code applies Fast-Fourier Transforms to complete sub-pixel analysis of the cross-correlation results using the code in Appendix A. This code was previously developed, and no changes were made to apply the code in the present investigation. The image was registered to $1/20th$ of a pixel.

```
function [output, Greg] = mydftregistration(buf1ft,buf2ft,
    usfac)
% function [output Greg] = dftregistration(buf1ft,buf2ft,
    usfac);
% Subpixel image registration by crosscorrelation. It
    obtains an initial
% estimate of the crosscorrelation peak by an FFT and then
     refines the
% shift estimation by upsampling the DFT in a small
    neighborhood of that
% estimate by means of a matrix-multiply DFT. With this
    procedure all the
% image points are used to compute the upsampled
    crosscorrelation.
%
% Citation:
% Manuel Guizar-Sicairos, Samuel T. Thurman, and James R.
    Fienup,
% "Efficient subpixel image registration algorithms," Opt.
     Lett. 33,
% 156-158 (2008).
```

```
%
% Inputs
% buf1ft    Fourier transform of reference image,
%           DC in (1,1)   [DO NOT FFTSHIFT]
% buf2ft    Fourier transform of image to register,
%           DC in (1,1) [DO NOT FFTSHIFT]
% usfac     Upsampling factor (integer). Images will be
   registered to
%           within 1/usfac of a pixel. For example usfac =
    20 means the
%           images will be registered within 1/20 of a
   pixel. (default = 1)
%
% Outputs
% output =  [error,diffphase,net_row_shift,net_col_shift]
% error     Translation invariant normalized RMS error
   between f and g
% diffphase     Global phase difference between the two
   images (should be
%               zero if images are non-negative).
% net_row_shift net_col_shift   Pixel shifts between
   images
% Greg      (Optional) Fourier transform of registered
   version of buf2ft,
%           the global phase difference is compensated for
   .
```

```
%

if ~exist('usfac','var')
    usfac = 20;
end

[nr,nc]=size(buf2ft);
Nr = ifftshift(-fix(nr/2):ceil(nr/2)-1);
Nc = ifftshift(-fix(nc/2):ceil(nc/2)-1);

if usfac == 0
    % Simple computation of error and phase difference
       without registration
    CCmax = sum(buf1ft(:).*conj(buf2ft(:)));
    row_shift = 0;
    col_shift = 0;
elseif usfac == 1
    % Single pixel registration
    CC = ifft2(buf1ft.*conj(buf2ft));
    CCabs = abs(CC);
    [row_shift, col_shift] = find(CCabs == max(CCabs(:)));
    CCmax = CC(row_shift,col_shift)*nr*nc;
    % Now change shifts so that they represent relative
       shifts and not indices
    row_shift = Nr(row_shift);
    col_shift = Nc(col_shift);
```

```
elseif usfac > 1
    % Start with usfac == 2
    CC = ifft2(FTpad(buf1ft.*conj(buf2ft),[2*nr,2*nc]));
    CCabs = abs(CC);
    [row_shift, col_shift] = find(CCabs == max(CCabs(:))
       ,1,'first');
    CCmax = CC(row_shift,col_shift)*nr*nc;
    % Now change shifts so that they represent relative
       shifts and not indices
    Nr2 = ifftshift(-fix(nr):ceil(nr)-1);
    Nc2 = ifftshift(-fix(nc):ceil(nc)-1);
    row_shift = Nr2(row_shift)/2;
    col_shift = Nc2(col_shift)/2;
    % If upsampling > 2, then refine estimate with matrix
       multiply DFT
    if usfac > 2,
        %%% DFT computation %%%
        % Initial shift estimate in upsampled grid
        row_shift = round(row_shift*usfac)/usfac;
        col_shift = round(col_shift*usfac)/usfac;
        dftshift = fix(ceil(usfac*1.5)/2); %% Center of
           output array at dftshift+1
        % Matrix multiply DFT around the current shift
           estimate
        CC = conj(dftups(buf2ft.*conj(buf1ft),ceil(usfac
           *1.5),ceil(usfac*1.5),usfac,...
```

```
            dftshift-row_shift*usfac,dftshift-col_shift*
               usfac));
        % Locate maximum and map back to original pixel
           grid
        CCabs = abs(CC);
        [rloc, cloc] = find(CCabs == max(CCabs(:)),1,'
           first');
        CCmax = CC(rloc,cloc);
        rloc = rloc - dftshift - 1;
        cloc = cloc - dftshift - 1;
        row_shift = row_shift + rloc/usfac;
        col_shift = col_shift + cloc/usfac;
    end

    % If its only one row or column the shift along that
       dimension has no
    % effect. Set to zero.
    if nr == 1,
        row_shift = 0;
    end
    if nc == 1,
        col_shift = 0;
    end

end
```

```
rg00 = sum(abs(buf1ft(:)).^2);
rf00 = sum(abs(buf2ft(:)).^2);
error = 1.0 - abs(CCmax).^2/(rg00*rf00);
error = sqrt(abs(error));
diffphase = angle(CCmax);

output=[error,diffphase,row_shift,col_shift];

% Compute registered version of buf2ft
if (nargout > 1)&&(usfac > 0),
    [Nc,Nr] = meshgrid(Nc,Nr);
    Greg = buf2ft.*exp(1i*2*pi*(-row_shift*Nr/nr-col_shift
       *Nc/nc));
    Greg = Greg*exp(1i*diffphase);
elseif (nargout > 1)&&(usfac == 0)
    Greg = buf2ft*exp(1i*diffphase);
end
return

function out=dftups(in,nor,noc,usfac,roff,coff)
% function out=dftups(in,nor,noc,usfac,roff,coff);
% Upsampled DFT by matrix multiplies, can compute an
   upsampled DFT in just
% a small region.
% usfac         Upsampling factor (default usfac = 1)
```

```
% [nor,noc]     Number of pixels in the output upsampled
   DFT, in
%               units of upsampled pixels (default = size(
   in))
% roff, coff    Row and column offsets, allow to shift the
    output array to
%               a region of interest on the DFT (default =
    0)
% Recieves DC in upper left corner, image center must be
   in (1,1)

[nr,nc]=size(in);
% Set defaults
if exist('roff', 'var')~=1, roff=0;  end
if exist('coff', 'var')~=1, coff=0;  end
if exist('usfac','var')~=1, usfac=1; end
if exist('noc',  'var')~=1, noc=nc;  end
if exist('nor',  'var')~=1, nor=nr;  end
% Compute kernels and obtain DFT by matrix products
kernc=exp((-1i*2*pi/(nc*usfac))*( ifftshift(0:nc-1).' -
   floor(nc/2) )*( (0:noc-1) - coff ));
kernr=exp((-1i*2*pi/(nr*usfac))*( (0:nor-1).' - roff )*(
   ifftshift([0:nr-1]) - floor(nr/2)  ));
out=kernr*in*kernc;
return
```

```
function [ imFTout ] = FTpad(imFT,outsize)
% imFTout = FTpad(imFT,outsize)
% Pads or crops the Fourier transform to the desired ouput
    size. Taking
% care that the zero frequency is put in the correct place
    for the output
% for subsequent FT or IFT. Can be used for Fourier
   transform based
% interpolation, i.e. dirichlet kernel interpolation.
%
%   Inputs
% imFT      - Input complex array with DC in [1,1]
% outsize   - Output size of array [ny nx]
%
%   Outputs
% imout     - Output complex image with DC in [1,1]

if ~ismatrix(imFT)
    error('Maximum number of array dimensions is 2')
end
Nout = outsize;
Nin = size(imFT);
imFT = fftshift(imFT);
center = floor(size(imFT)/2)+1;
```

```
imFTout = zeros(outsize);
centerout = floor(size(imFTout)/2)+1;

% imout(centerout(1)+[1:Nin(1)]-center(1),centerout(2)+[1:
   Nin(2)]-center(2)) ...
%      = imFT;
cenout_cen = centerout - center;
imFTout(max(cenout_cen(1)+1,1):min(cenout_cen(1)+Nin(1),
   Nout(1)),max(cenout_cen(2)+1,1):min(cenout_cen(2)+Nin
   (2),Nout(2))) ...
    = imFT(max(-cenout_cen(1)+1,1):min(-cenout_cen(1)+Nout
       (1),Nin(1)),max(-cenout_cen(2)+1,1):min(-cenout_cen
       (2)+Nout(2),Nin(2)));

imFTout = ifftshift(imFTout)*Nout(1)*Nout(2)/(Nin(1)*Nin
   (2));
return
```

Appendix C. Optimized Ensemble regression Analysis

The following code was developed to run initial ensemble regressions of the data presented from Kumar et al. It was developed by 2d Lt Hankins. The code provides a base to build additional models and further assess the potential for ensemble regression in the design of ballistic armors.

```
close all
clear all
clc
DataTable = readtable('Test_Excel_Sort.xlsx');
[hc,hb,h,ad,hcoh,hchb,hch,haad,hchcoh,hbh,hbad,hbohch,had,
   hhcoh,adhcoh,hchc,hbhb,hh,adad,hcohhcoh,Vbl] = readvars
   ('Test_Excel_Sort.xlsx'); %readvars('
   Execl_Data_VblLastColumn.xlsx');
X_Vars = [hc,hb,h,ad,hcoh];
Y_Vars = Vbl;
X_Vars_Fit = X_Vars(1:4:60,:);
Y_Vars_Fit = Y_Vars(1:4:60);
tic

rng default
Md1a = fitrensemble(X_Vars_Fit,Y_Vars_Fit,...
    'Method','LSBoost',...
    'PredictorNames',{'Ceramic␣Thickness','Back␣Plate␣
       Thickness','Total␣Thickness', 'Areal␣Density', '
       Ceramic␣Ratio'})
```

```
rng default
Md2a = fitrensemble(X_Vars_Fit,Y_Vars_Fit,...
    'Method','Bag',...
    'PredictorNames',{'Ceramic␣Thickness','Back␣Plate␣
      Thickness','Total␣Thickness', 'Areal␣Density', '
      Ceramic␣Ratio'})

rng default
Md2b = fitrensemble(X_Vars_Fit,Y_Vars_Fit,...
    'Method','Bag',...
    'OptimizeHyperparameters',{'NumLearningCycles','
      MaxNumSplits'},...
    'HyperparameterOptimizationOptions',struct('
      Repartition',true,...
    'AcquisitionFunctionName','expected-improvement-plus'
      ,...
     'SaveIntermediateResults',1),...
    'PredictorNames',{'Ceramic␣Thickness','Back␣Plate␣
      Thickness','Total␣Thickness', 'Areal␣Density', '
      Ceramic␣Ratio'})


rng default
Md1b = fitrensemble(X_Vars_Fit,Y_Vars_Fit,...
    'Method','LSBoost',...
```

```
    'Learner',templateTree('Surrogate','on'),...
    'OptimizeHyperparameters',{'NumLearningCycles','
       MaxNumSplits','LearnRate'},...
    'HyperparameterOptimizationOptions',struct('
       Repartition',true,...
    'AcquisitionFunctionName','expected-improvement-plus'
       ,...
     'SaveIntermediateResults',1),...
    'PredictorNames',{'Ceramic Thickness','Back Plate
       Thickness','Total Thickness', 'Areal Density', '
       Ceramic Ratio'})
toc

for index = 1:length(X_Vars)
PVBL1a(index)= predict(Md1a,[X_Vars(index,1) X_Vars(index
   ,2) X_Vars(index,3) X_Vars(index,4) X_Vars(index,5)]);
PVBL2a(index) = predict(Md2a,[X_Vars(index,1) X_Vars(index
   ,2) X_Vars(index,3) X_Vars(index,4) X_Vars(index,5)]);
PVBL1b(index) = predict(Md1b,[X_Vars(index,1) X_Vars(index
   ,2) X_Vars(index,3) X_Vars(index,4) X_Vars(index,5)]);
PVBL2b(index) = predict(Md2b,[X_Vars(index,1) X_Vars(index
   ,2) X_Vars(index,3) X_Vars(index,4) X_Vars(index,5)]);
error1a(index) = abs((PVBL1a(index)-Vbl(index))/Vbl(index)
   )*100;
error1b(index) = abs((PVBL1b(index)-Vbl(index))/Vbl(index)
   )*100;
```

```
error2a(index) = abs((PVBL2a(index)-Vbl(index))/Vbl(index)
   )*100;
error2b(index) = abs((PVBL2b(index)-Vbl(index))/Vbl(index)
   )*100;
end
Import1a = predictorImportance(Md1a);
Import1b = predictorImportance(Md1b);
Import2a = predictorImportance(Md2b);
Import2b = predictorImportance(Md2b);
%% Plots

figure(4)
plot(PVBL1a,'g'),hold on, plot(PVBL1b,'m') ,plot(PVBL2a,'r
   '),plot(PVBL2b,'b'),plot(Y_Vars,'k')
legend({'Boost','Boost␣Opt','Bag','Bag␣Opt','True'});
title('Learned␣Responses␣vs␣True␣Values');
xlabel('Sample␣Number');
ylabel('V_B_L␣(m/s)');
hold off

figure(5)
plot(error1a,'g'),hold on, plot(error1b,'m') ,plot(error2a
   ,'r'),plot(error2b,'b')
legend({'Boost','Boost␣Opt','Bag','Bag␣Opt'})
title('Percent␣Error␣From␣True␣Results');
xlabel('Sample␣Number');
```

```
ylabel('Error␣(%)');
hold off

Errors1a = predict(Md1a,X_Vars) - Vbl;
Errors1b = predict(Md1b,X_Vars) - Vbl;
Errors2a = predict(Md2a,X_Vars) - Vbl;
Errors2b = predict(Md2b,X_Vars) - Vbl;

figure(6)
hold on
subplot(2,2,1)

histfit(Errors1a,10)
title('Boost')
subplot(2,2,2)

histfit(Errors1b,10)
title('Boost␣Opt')
subplot(2,2,3)

histfit(Errors2a,10)
title('Bag')
subplot(2,2,4)

histfit(Errors2b,10)
title('Bag␣Opt')
```

```
sgtitle('Normal Histogram Fit')
hold off

figure(7)
hold on
subplot(2,2,1)

normplot(Errors1a)
title('Boost')
subplot(2,2,2)

normplot(Errors1b)
title('Boost Opt')
subplot(2,2,3)

normplot(Errors2a)
title('Bag')
subplot(2,2,4)

normplot(Errors2b)
title('Bag Opt')
sgtitle('Normal Probability Plot')
hold off

figure(8)
hold on
```

```
scatter(Vbl, Errors1a,'.','r')
scatter(Vbl, Errors1b,'.','b')
scatter(Vbl, Errors2a,'+','g')
scatter(Vbl, Errors2b,'+','k')
refline(0,1);
xlabel('Predicted');
ylabel('Residuals');
title('Residual␣Scatter␣Plot');
legend({'Boost','Boost␣Opt','Bag','Bag␣Opt'});
hold off

figure(9)
hold on
boxplot(Errors1a,X_Vars(:,1),'PlotStyle','compact');
%boxplot(Errors1b,X_Vars(:,1),'PlotStyle','compact');
%boxplot(Errors2a,X_Vars(:,1),'PlotStyle','compact');
%boxplot(Errors2b,X_Vars(:,1),'PlotStyle','compact');
xlabel('Ceramic␣Plate␣Thickness,␣(mm)');
ylabel('Errors');
title('Errors␣by␣Ceramic␣Plate␣Thickness');
hold off

figure(10)

hold on
boxplot(Errors1a,X_Vars(:,2),'PlotStyle','compact');
```

```
%boxplot(Errors1b,X_Vars(:,2),'PlotStyle','compact');
%boxplot(Errors2a,X_Vars(:,2),'PlotStyle','compact');
%boxplot(Errors2b,X_Vars(:,2),'PlotStyle','compact');
xlabel('Composite␣Backing␣Plate␣Thickness,␣(mm)');
ylabel('Errors');
title('Errors␣by␣Composite␣Backing␣Plate␣Thickness');
hold off

figure(11)
hold on
boxplot(Errors1a,X_Vars(:,3),'PlotStyle','compact');
%boxplot(Errors1b,X_Vars(:,3),'PlotStyle','compact');
%boxplot(Errors2a,X_Vars(:,3),'PlotStyle','compact');
%boxplot(Errors2b,X_Vars(:,3),'PlotStyle','compact');
xlabel('Total␣Armor␣Thickness,␣(mm)');
ylabel('Errors');
title('Errors␣by␣Total␣Armor␣Thickness');
hold off

figure(12)

hold on
boxplot(Errors1a,X_Vars(:,4),'PlotStyle','compact');
%boxplot(Errors1b,X_Vars(:,4),'PlotStyle','compact');
%boxplot(Errors2a,X_Vars(:,4),'PlotStyle','compact');
%boxplot(Errors2b,X_Vars(:,4),'PlotStyle','compact');
```

```
xlabel('Areal Density, (kg/m^2)');
ylabel('Errors');
title('Errors by Areal Density');
hold off

figure(13)

hold on
boxplot(Errors1a,X_Vars(:,5),'PlotStyle','compact');
%boxplot(Errors1b,X_Vars(:,5),'PlotStyle','compact');
%boxplot(Errors2a,X_Vars(:,5),'PlotStyle','compact');
%boxplot(Errors2b,X_Vars(:,5),'PlotStyle','compact');
xlabel('Ceramic Plate Thickness to Backing Ratio');
ylabel('Errors');
title('Errors by Ceramic Plate Thickness to Backing Ratio'
   );
hold off
```

Bibliography

1. R. Kinsler and J. Collins, "Comparison of V_{50} Shot Placement on Final Outcome," in *Proceedings Personal Armor Systems Symposium*, PASS, November 2014.

2. M. P. Keane, "Ballistic Limit Shot Dependency Testing in Composite Materials," Master's thesis, Air Force Institute of Technology, 13 June 2019.

3. C. J. Wu and Y. Tian, "Three-phase Optimal Design of Sensitivity Experiments," vol. 22, pp. 400–407, September 1951.

4. "V_{50} Ballistic Test for Armor," Department of Defense Test Method Standard MIL-STD-662F, 18 Dec 1997.

5. "A review of the v_{50} ballistic limit requirements of mil-a-46100," tech. rep.

6. "Armor:Lightweight, Composite," Performance Specification MIL-PERF-46103E, 6 January 1998.

7. "Ballistic Performance Ranking of Ceramic Armor Plates Against High Density Penetrators," Military Standard MIL-STD-376, 28 June 1993.

8. "Ballistic Resistance of Body Armor," NIJ Standard 0101.06, U.S. Department of Justice: Office of Justice Programs, July 2008.

9. "Ballistic Resistance of Body Armor," NIJ Standard 0101.07, U.S. Department of Justice: Office of Justice Programs, January 2018. Draft.

10. "Ballistic Test Method for Personal Armour Materials and Combat Clothing," Standardization Agreement STANAG 2920, 31 July 2003.

11. M. Bolduc and H. Jager, "Summary of Newly Ratified NATO Standard AEP 2920, Ed. A, V1," Tech. Rep. DRDC-RDDC-2016-P065, 2019.

12. J. Eridon and S. Mishler, "Ballistic Validation Test Statistics and Confidence Levels," in *Proceedings Ground Vehicle Systems Engineering and Technology Symposium*, NDIA, 11-13 Aug 2020.

13. J. C. Collins, "Quantal Response: Practical Sensitivity Testing," Tech. Rep. ARL-TR-7088, Septembe 2014.

14. H. J. Langlie, "A Reliabilty Test Method for "One-Shot" Items," in *Proceedings Eight Conference on the Design of Experiments in Army Research Development and Testing*, vol. ADA419759, 1962.

15. J. C. Collins and L. L. C. Moss, "LangMod Users Manual," Tech. Rep. ARL-TN-437, June 2011.

16. S. Burke and L. Truett, "Test Strategies for Experiments with a Binary Response and Single Stress Factor: Best Practice," Tech. Rep. STAT COE-Report-08-2017, Wright-Patterson AFB, OH, 15 June 2017.

17. B. T. Neyer, "Sensitivity Testing and Analysis," in *Proceedings of the Sixteenth International Pyrotechnics Seminar*, April 1994. Date Accessed: 20 Oct 2021.

18. B. T. Neyer, "A D-Optimality Based Sensitivity Test," in *Technometrics*, vol. 36, pp. 61–70, February 1994. Date Accessed: 20 Oct 2021.

19. P. A. Roediger, "GONOGO: an R Implementation of Test Methods to Perform, Analyze, and Simulate Sensitivity Experiments," Tech. Rep. AREIS-CR-18007, November 2018. Draft.

20. H. Robbins and S. Monro, "A Stochastic Approximation Method," *The Annals of Mathematical Statistics*, vol. 22, pp. 400–407, September 1951.

21. V. R. Joseph, "Efficient Robbins-Monroe Procedure for Binary Data," tech. rep., Georgia Institute of Technology, 2004.

22. D. Wang, Y. Tian, and C. F. J. Wu, "A Skewed Version of the Robbins-Monroe-Joseph Procedure for Binary Response," *Statistica Sinica*, vol. 25, pp. 1679–1689, October 2015.

23. J. C. Collins, "Quantal Response: Practical Sensitivity Testing," Tech. Rep. ARL-TR-6022, June 2012.

24. D. Mauchant, K. D. Rice, M. A. Riley, D. Leber, D. Samarov, and A. L. Forster, "Analysis of Three Different Regression Models to Estimate the Ballistic Performance of New and Environmentally Conditioned Body Armor," Tech. Rep. NISTIR 7760, U.S. Department of Commerce, February 2011.

25. A. L. Chang and B. A. Bodt, "JTCG/AS Interlaboratory Ballistic Test Program - Final Report," Tech. Rep. ARL-TR-1577, December 1997.

26. G. G. Ojoc, C. Pirvu, and L. Deleanu, "Standardization in Testing Ballistic Protection Systems," *IOP Conference Series: Materials Science and Engineering*, no. 724, 2020.

27. T. H. Johnson, L. Freeman, J. Hester, and J. L. Bell, "A Comparison of Ballistic Resistance Testing Techniques in the Department of Defense," *IEEE Access*, vol. 2, pp. 1442–1455, 2014.

28. B. Tahenti, F. Coghe, and R. Nasri, "Ballistic Limit Estimation Approaches for Ballistic Resistance Assessment," *Defence Science Journal*, vol. 70, pp. 82–87, 02 2020.

29. C. Andres and W. Boughers, "An Analysis of V_50 Ballistic Limit Results Adjusting 1st Shot Velocity, Step-Up Step-Down Increments, Truth Characteristics and Velocity Control Distributions," Department of Defense Test Method Standard ADA624217, 1 March 2012.

30. M. A. Riley, K. D. Rice, and A. L. Forester, "Assessment of Uncertainty in Ballistic Response Estimates Obtained from Ballistic Limit Testing," in *Proceedings Personal Armor Systems Symposium*, PASS, 2012.

31. J. Xu, C. Xiong, and R. Mu, "A Bayesian Stochastic Approximation Method," *Journal of Statistical Planning and Inference*, vol. 211, 05 2017.

32. R. L. Sierakowski, J. G. E. Nevill, C. A. Ross, and E. R. Jones, "Studies on the Ballistic Impact of Composite Materials," Tech. Rep. AD863202, 4 October 1972.

33. D. E. Carlucci and S. S. Jacobson, *Ballistics: Theory and Design of Guns and Ammunition*, ch. 15. Taylor and Francis Group, LLC, 2nd ed., 2008.

34. J. A. Zukas, "Impact Dynamics: Theory and Experiment," Tech. Rep. ARBRL-TR-02271, October 1980.

35. J. A. Zukas and W. P. Walters, eds., *Explosive Effects and Applications*. Springer, 1998.

36. P. W. Cooper, *Explosives Engineering*, ch. 19. Wiley-VCH, Inc., 1996.

37. N. K. Naik and A. V. Doshi, "Ballistic Impact Behavior of Thick Composites: Analytical Formulation," *AIAA Journal*, vol. 43, no. 7, pp. 1525–1536, 2005.

38. J. López-Puente, R. Zaera, and C. Navarro, "An analytical model for high velocity impacts on thin CFRPs woven laminated plates," *International Journal of Solids and Structures*, vol. 44, no. 9, pp. 2837–2851, 2007.

39. S. García-Castillo, S. Sanchez-Saez, and E. Barbero, "Nondimensional analysis of ballistic impact on thin woven laminate plates," *International Journal of Impact Engineering*, vol. 39, 01 2012.

40. T. Langston, "An analytical model for the ballistic performance of ultra-high molecular weight polyethylene composites," *Composite Structures*, vol. 179, pp. 245–257, 2017.

41. L. Bresciani, A. Manes, and M. Giglio, "An analytical model for ballistic impacts against plain-woven fabrics with a polymeric matrix," *International Journal of Impact Engineering*, vol. 78, pp. 138–149, 2015.

42. R. Mohamadipoor, M. Pol, and E. Zamani, "Nonlinear analytical study of thin laminated composite plate reinforced by nanoparticles under high-velocity impact," *Thin-Walled Structures*, vol. 127, pp. 446–458, 2018.

43. L. Alonso, C. Navarro, and S. K. García-Castillo, "Analytical models for the perforation of thick and thin thickness woven-laminates subjected to high-velocity impact," *Composites Part B: Engineering*, vol. 143, pp. 292–300, 2018.

44. R. Scazzosi, A. Manes, and M. Giglio, "Analytical Model of High-Velocity Impact of a Deformable Projectile Against Textile-Based Composites," *Journal of Materials Engineering and Performance*, vol. 28, 04 2019.

45. D. Gregori, R. Scazzosi, S. G. Nunes, S. C. Amico, M. Giglio, and A. Manes, "Analytical and numerical modelling of high-velocity impact on multilayer alumina/aramid fiber composite ballistic shields: Improvement in modelling approaches," *Composites Part B: Engineering*, vol. 187, p. 107830, 2020.

46. "Test Methods for Ballistic Defeat Materials," Department of Defense Test Method Standard MIL-STD-3038, 18 May 2011.

47. "Advanced Fibers and Composites: Spectra Shield® 4232." Customer Product Specification, 24 August 2015.

48. "Technical Fabrics Handbook," December 2010.

49. "Toray BT250E-1." Product Data Sheet, 09 July 2019.

50. "AF 163-2." Technical Datasheet, November 2009.

51. "Caldwell Ballistic Precision Chronograph: Care and Usage Instructions." Instruction Manual, May 2014.

52. D. C. Montgomery, *Design and Analysis of Experiments*, ch. 3. John Wiley and Sons, Inc., 8th ed., 2013.

53. S. Kumar, K. Akella, M. Joshi, A. Tewari, and N. Naik, "Performance of Ceramic-Composite Armors under Ballistic Impact Loading," *Journal of Materials Engineering and Performance*, vol. 29, 08 2020.

54. L. Blakely, M. J. Reno, and R. J. Broderick, "Decision tree ensemble machine learning for rapid QSTS simulations," in *2018 IEEE Power Energy Society Innovative Smart Grid Technologies Conference (ISGT)*, pp. 1–5, 2018.

55. R. Freund, P. Grigas, and R. Mazumder, "A New Perspective on Boosting in Linear Regression via Subgradient Optimization and Relatives," *The Annals of Statistics*, vol. 45, 05 2015.

56. P. Büddhlmann, "Bagging, Boosting and Ensemble Methods," *Handbook of Computational Statistics*, 01 2012.

57. J. Wu, X.-Y. Chen, H. Zhang, L.-D. Xiong, H. Lei, and S.-H. Deng, "Hyperparameter Optimization for Machine Learning Models Based on Bayesian Opti-

mization," *Journal of Electronic Science and Technology*, vol. 17, no. 1, pp. 26–40, 2019.

REPORT DOCUMENTATION PAGE

Form Approved
OMB No. 0704–0188

1. REPORT DATE *(DD–MM–YYYY)*	2. REPORT TYPE	3. DATES COVERED *(From — To)*
23–12–2021	Master's Thesis	Jul 2020 — Dec 2021

4. TITLE AND SUBTITLE

THE EFFECT OF SHOT DEPENDENCY ON COMPOSITE MATERIALS SUBJECT TO BALLISTIC TESTING

5a. CONTRACT NUMBER

5b. GRANT NUMBER

5c. PROGRAM ELEMENT NUMBER

6. AUTHOR(S)

Hankins, Clayton, 2d Lt, USAF

5d. PROJECT NUMBER

5e. TASK NUMBER

5f. WORK UNIT NUMBER

7. PERFORMING ORGANIZATION NAME(S) AND ADDRESS(ES)

Air Force Institute of Technology
Graduate School of Engineering and Management (AFIT/EN)
2950 Hobson Way
WPAFB OH 45433-7765

8. PERFORMING ORGANIZATION REPORT NUMBER

AFIT-ENY-MS-21-D-068

9. SPONSORING / MONITORING AGENCY NAME(S) AND ADDRESS(ES)

Joint Aircraft Survivability Program
701 Courthouse Road
Suite 1G140, Building 15
Arlington, VA 22204-2489
COMM: 703-604-0387
Email: contact@jasp-online.org

10. SPONSOR/MONITOR'S ACRONYM(S)

11. SPONSOR/MONITOR'S REPORT NUMBER(S)

12. DISTRIBUTION / AVAILABILITY STATEMENT

DISTRIBUTION STATEMENT A:
APPROVED FOR PUBLIC RELEASE; DISTRIBUTION UNLIMITED.

13. SUPPLEMENTARY NOTES

14. ABSTRACT

Ballistic analysis was performed on four common composite armor materials: 3k standard modulus plain weave carbon fiber, 8HS satin weave S-glass fiber, plain weave Kevlar® KM2 600 Denier fiber, and Spectra Shield® 4232 ultra-high molecular weight polyethylene to determine shot dependency based upon shot-to-shot impact distance, degree of penetration from the initial impacts, and the delamination effects from the initial impact. The primary measure of ballistic performance was the projectile velocity which represents a 50% probability of penetration, V_{50}. This velocity was determined using a three-phase optimal design test method with an average of twelve shots per test. Delamination was assessed via visual inspection and the tap test. All plates were 0.25 inches thick and impacted at 0° obliquity from a 0.5-inch-diameter hardened steel ball bearing fired from a nitrogen gas gun. Additionally, an ensemble regression analysis of available ceramic armor data was performed to model ballistic performance. The experimental study found no statistically significant increase in performance for the materials tested. The only shot dependency with statistical significance was a $1-2\%$ decrease of the ballistic limit for carbon fiber plates with a second impact one and two projectile diameters away. The regression ensemble proved capable of predicting the ballistic limit with an average error of 6.5%. The research recommends additional investigations into the ductility of composite materials to predict delamination, updates to MIL-STD-662F, and refinement of advanced modeling techniques in ballistic testing.

15. SUBJECT TERMS

Ballistic Testing, Gas Gun, Composites, Armor, Carbon Fiber, Glass Fiber, Aramid, Regression, Ceramic, Impact, Ballistic, Multi-Hit, Shot Dependency, UHMWPE, 3-Pod, Survivability

16. SECURITY CLASSIFICATION OF:			17. LIMITATION OF ABSTRACT	18. NUMBER OF PAGES	19a. NAME OF RESPONSIBLE PERSON
a. REPORT	b. ABSTRACT	c. THIS PAGE			2d Lt Clayton C. Hankins, AFIT/ENY
U	U	U	UU	187	19b. TELEPHONE NUMBER *(include area code)* (816)-714-8042; clayton.hankins@afit.edu